

ISSN 0352-9045

Informacije MIDEM

*Journal of Microelectronics,
Electronic Components and Materials*
Vol. 42, No. 1 (2012), March 2012

*Revija za mikroelektroniko,
elektronske sestavne dele in materiale*
letnik 42, številka 1 (2012), Marec 2012



Informacije MIDE M 1-2012

Journal of Microelectronics, Electronic Components and Materials

VOLUME 42, NO. 1(141), LJUBLJANA, MARCH 2012 | LETNIK 42, NO. 1(141), LJUBLJANA, MAREC 2012

Published quarterly (March, June, September, December) by Society for Microelectronics, Electronic Components and Materials - MIDE M. Copyright © 2012. All rights reserved. | Revija izhaja trimesečno (marec, junij, september, december). Izdaja Strokovno društvo za mikroelektroniko, elektronske sestavne dele in materiale – Društvo MIDE M. Copyright © 2012. Vse pravice pridržane.

Editor in Chief | Glavni in odgovorni urednik

Marko Topič, University of Ljubljana (UL), Faculty of Electrical Engineering, Slovenia

Editor of Electronic Edition | Urednik elektronske izdaje

Kristijan Brecl, UL, Faculty of Electrical Engineering, Slovenia

Associate Editors | Odgovorni področni uredniki

Vanja Ambrožič, UL, Faculty of Electrical Engineering, Slovenia

Slavko Amon, UL, Faculty of Electrical Engineering, Slovenia

Danjela Kuščer Hrovatin, Jožef Stefan Institute, Slovenia

Matjaž Vidmar, UL, Faculty of Electrical Engineering, Slovenia

Andrej Žemva, UL, Faculty of Electrical Engineering, Slovenia

Editorial Board | Uredniški odbor

Mohamed Akil, ESIEE PARIS, France

Giuseppe Buja, University of Padova, Italy

Gian-Franco Dalla Betta, University of Trento, Italy

Ciprian Iliescu, Institute of Bioengineering and Nanotechnology, A*STAR, Singapore

Malgorzata Jakubowska, Warsaw University of Technology, Poland

Marc Lethiecq, University of Tours, France

Teresa Orłowska-Kowalska, Wrocław University of Technology, Poland

Luca Palmieri, University of Padova, Italy

International Advisory Board | Časopisni svet

Janez Trontelj, UL, Faculty of Electrical Engineering, Slovenia - Chairman

Cor Claeys, IMEC, Leuven, Belgium

Denis Donlagič, University of Maribor, Faculty of Elec. Eng. and Computer Science, Slovenia

Zvonko Fazarinc, CIS, Stanford University, Stanford, USA

Leszek J. Golonka, Technical University Wrocław, Wrocław, Poland

Jean-Marie Haussonne, EIC-LUSAC, Octeville, France

Marija Kosec, Jožef Stefan Institute, Slovenia

Miran Mozetič, Jožef Stefan Institute, Slovenia

Stane Pejovnik, UL, Faculty of Chemistry and Chemical Technology, Slovenia

Giorgio Pignatelli, University of Perugia, Italy

Giovanni Soncini, University of Trento, Trento, Italy

Iztok Šorli, MIKROIKS d.o.o., Ljubljana, Slovenia

Headquarters | Naslov uredništva

Uredništvo Informacije MIDE M

MIDE M pri MIKROIKS

Stegne 11, 1521 Ljubljana, Slovenia

T. +386 (0)1 513 37 68

F. + 386 (0)1 513 37 71

E. info@midem-drustvo.si

www.midem-drustvo.si

Annual subscription rate is 100 EUR, separate issue is 25 EUR. MIDE M members and Society sponsors receive current issues for free. Scientific Council for Technical Sciences of Slovenian Research Agency has recognized Informacije MIDE M as scientific Journal for micro-electronics, electronic components and materials. Publishing of the Journal is cofinanced by Slovenian Book Agency and by Society sponsors. Scientific and professional papers published in the journal are indexed and abstracted in COBISS and INSPEC databases. The Journal is indexed by ISI® for Sci Search®, Research Alert® and Material Science Citation Index™. |

Letna naročnina je 100 EUR, cena posamezne številke pa 25 EUR. Člani in sponzorji MIDE M prejema posamezne številke brezplačno. Znanstveni svet za tehnične vede je podal pozitivno mnenje o reviji kot znanstveno-strokovni reviji za mikroelektroniko, elektronske sestavne dele in materiale. Izdajo revije sofinancirajo JAKRS in sponzorji društva. Znanstveno-strokovne prispevke objavljene v Informacijah MIDE M zajemamo v podatkovne baze COBISS in INSPEC. Prispevke iz revije zajema ISI® v naslednje svoje produkte: Sci Search®, Research Alert® in Materials Science Citation Index™.

Po mnenju Ministrstva za informiranje št.23/300-92 se šteje glasilo Informacije MIDE M med proizvode informativnega značaja.

Content | Vsebina

| <i>Original papers</i> | | <i>Izvirni članki</i> |
|---|----|--|
| Editorial | 2 | Uvodnik |
| D. A. Shnawah, M. F. M. Sabri, I. A. Badruddin: The Limited Reliability of Board-Level SAC Solder Joints under both Mechanical and Thermo-mechanical Loads | 3 | D. A. Shnawah, M. F. M. Sabri, I. A. Badruddin: Spoji pri mehaničnih in termo-mehaničnih obremenitvah |
| G. Bizjak, M. B. Kobav, B. Luin: Quality Control of Automotive Switches with help of Digital Camera | 11 | G. Bizjak, M. B. Kobav, B. Luin: Kontrola kakovosti avtomobilskih stikal s pomočjo digitalne kamere |
| M. R. I. Faruque, M. T. Islam, N. Misran: A New Design of Split Ring Resonators for Electromagnetic (EM) absorption Reduction in Human Head | 18 | M. R. I. Faruque, M. T. Islam, N. Misran: Nova oblika prekinjenih obročnih resonatorjev za zmanjševanje elektromagnetne absorpcije v človeški glavi |
| V. Gradišnik: Characterization of A-Si:H P-I-N Photodiode Response | 23 | V. Gradišnik: Karakterizacija odziva a-Si:H P-I-N fotodiode |
| T. Korošec, S. Tomažič: An Adaptive-Parity Error-Resilient LZ'77 Compression Algorithm | 29 | T. Korošec, S. Tomažič: Na napake odporen zgoščevalni algoritem LZ'77 s prilagodljivo pariteto |
| J. Koselj, V. B. Bregar: Influence of parameters of the flanged open- ended coaxial probe measurement setup on permittivity measurement | 36 | J. Koselj, V. B. Bregar: Vpliv parametrov merilnega sistema z odprto koaksialno sondo na meritve dielektričnosti |
| F. Pavlovčič: Kinetics of Discharging Arc Formation | 43 | F. Pavlovčič: Kinetika nastanka razelektritvenih oblikov |
| L. Pavlovič, J. Trontelj in D. Kostevc: 300 GHz microbolometer double-dipole antenna for focal-plane-array imaging | 56 | L. Pavlovič, J. Trontelj in D. Kostevc: 300 GHz mikrobolometriška antena z dvojnimi dipolom za slikanje s poljem v goriščni ravnini |
| M. Petkovšek, P. Kosmatin, C. Zevnik, D. Vončina, P. Zajec: Measurement system for testing of bipolar plates for PEM electrolyzers | 60 | M. Petkovšek, P. Kosmatin, C. Zevnik, D. Vončina, P. Zajec: Merilni sistem za testiranje bipolarnih plošč PEM elektrolizne celice |
| D. Strle: Design and Modeling High Performance Electromechanical Σ - Δ Modulator | 68 | D. Strle: Načrtovanje in modeliranje elektro-mehanskega Σ - Δ modulatorja z visoko ločljivostjo |
| M. J. T. Marvast, H. Sanusi, M. A. M. Ali: A 4.1-bit, 20 GS/s Comparator for High Speed Flash ADC in 45 nm CMOS Technology | 73 | M. J. T. Marvast, H. Sanusi, M. A. M. Ali: 4.1-bitni 20 GS/s komparator za hitrobliskovni ADC v 45 nm CMOS tehnologiji |
| Front page : Array of photovoltaic modules | | Naslovnica : Polje fotonapetostnih modulov |

Editorial | Uvodnik

Last year we celebrated twenty five years, a quarter of century, of the MIDE M Society – Society of Microelectronics, Electronic Components and Materials. There are two activities of our society that made it non-erasable in the history: the MIDE M conferences, 3-day international conferences taking place every September at different locations across picturesque Slovenia and the journal Informacije MIDE M – Journal of Microelectronics, Electronic Components and Materials. Both conference total number (48th in 2012) and journal volume number (42th in 2012) exceed the quarter-centennial history of our society, since we have ancestors in SSOSD (Federal Professional Committee of Electronic Components at ETAN (Yugoslav Association of Electronics, Telecommunication, Automation and Nuclear Engineering). The SSOSD Committee started to inform its members by publishing the newsletter called »Informacije SSOSD« in August 1969. In October 1977 the committee has been renamed to a section of ETAN as SSESD (Professional Section for Electronic Components, Microelectronics and Materials), which continued to publish »Informacije SSESD« until January 1986. In 1986 a new society was born, MIDE M (Strokovno društvo za mikroelektroniko, elektronske sestavne dele in materiale), registered in Ljubljana on 23 April 1986 as the first yugoslav professional society related to Microelectronics, Electronic Components and Materials. It took over the destiny and continuation of the newsletter with scientific and professional articles under the name »Informacije MIDE M« (ISSN 0352-9045). In 1987 Dr. Iztok Šorli became its Editor-in-Chief and thanks to him and members of Editorial Board the »Informacije MIDE M« evolved into scientific-professional journal with peer review articles. Based on high scientific quality and professional publishing process our journal has been accepted on the list of SCIE journals. The first impact factor by JCR (Journal Citation Reports) was 0,088 in 1998. Dr. Iztok Šorli has not been only successful Editor-in-Chief, but also excellent Technical Editor for 25 years. In recognition to his merits and distinguished contribution the Society MIDE M awarded him with a prize at the MIDE M Academy on occasion of 25th Anniversary of the MIDE M Society in May 2011. On behalf of all former Editorial Board Members, all reviewers and authors I would express our sincere gratitude and admiration for his tremendous work, great effort and devotion. Although he stepped down from EIC position, he stays in the Advisory Board of our journal. In the last six months we have renewed both the journal's International Advisory Board and Editorial Board. The renewed Editorial Board has five associate editors responsible for fields of Technology & Materials, Electronics (including Microelectronics), Sensors & Actuators, Power Engineering and Communications. Our Editorial Board has been expanded with distinguished researchers from Europe who will together with associate editors assure fair peer review process of increasing number of original scientific manuscripts. Scientists and professionals are also invited to submit review manuscripts related to the journal scope or any important news relevant to above mentioned fields to be considered for publication.

Informacije MIDE M also celebrated in 2011 its 25th anniversary of the journal design that called for renewal. I sincerely hope you like the new outlook and design.

For me personally, this is the first Editorial which I have the honour to write. I have served as Editorial Board Member for 10 years and I believe Informacije MIDE M is in very good health and spirit, and we can look forward to its prosperous future. I envision the role of the whole Editorial Board as the unique opportunity to work with so many highly dedicated authors and reviewers for benefit of our readers and community with one common goal: advancing science and engineering!

Marko Topič
Editor-in-Chief

P.S.

All papers published in Informacije MIDE M (since 1986) can be access electronically at <http://midem-drustvo.si/journal/home.aspx>.

The Limited Reliability of Board-Level SAC Solder Joints under both Mechanical and Thermo-mechanical Loads

Dhafer Abdulameer Shnawah, Mohd Faizul Mohd Sabri, Irfan Anjum Badruddin*

*Department of Mechanical Engineering, University of Malaya,
 50603 Kuala Lumpur, Malaysia*

Abstract: The trend of miniaturization, light weight, high speed and multifunction are common in electronic assemblies, especially, for portable electronic products. In particular, board-level solder joint reliability, in term of both mechanical (e.g., drop impact) and thermo-mechanical (e.g., thermal cycling) loads is of great concern for portable electronic products. The transition to lead-free solder happened to coincide with a dramatic increase in portable electronic products. Sn–Ag–Cu (SAC) is now recognized as the standard lead-free solder alloy for packaging interconnects in the electronics industry. Hence, this study review the reliability of board-level SAC solders joints when subjected to drop impact and thermal cycling loading conditions **from the viewpoints of mechanical and micro-structural properties of the bulk solder**. The finding presented in this study indicates that the best SAC composition for drop performance is not necessarily the best composition for optimum thermal cycling reliability, thus the SAC solder alloys are limited in their potential applications in the electronic industries. This contribution has its value in giving information on possible developments and the suitability for the usage of SAC solder in portable electronic devices.

Keywords: SnAgCu solders, silver content, mechanical properties, microstructure properties, thermal cycling, drop impact

Spoji pri mehaničnih in termo-mehaničnih obremenitvah

Izvleček: Trend miniaturizacije, nižja teže, višje hitrosti in večopravnosti so običajni v elektronskih sestavih, posebej pri prenosnih elektronskih izdelkih. Zanesljivost spajkanega spoja v smislu mehanične (npr. vpliv padca) in termomehanične (termično ciklanje) obremenitve je poglobitnega pomena pri prenosnih elektronskih izdelkih. Prehod na spajko brez svinca se je zgodil istočasno z drastičnim povečanjem prenosnih elektronskih izdelkov. Zlitina Sn–Ag–Cu (SAC) danes predstavlja običajno spajko brez svinca v industriji elektronike. Pričujoča raziskava podaja pregled zanesljivosti spajkanih spojev pri obremenitvah zaradi padcev ali termičnih ciklanj v smislu mehaničnih in mikrostrukturnih lastnosti spajke. Predstavljene ugotovitve nakazujejo, da najboljša SAC zlitina pri vplivih padcev ni nujno tudi najbolj zanesljiva pri termičnem ciklanju, zaradi česar so SAC zlitine omejene na določene aplikacije v elektronski industriji. Ta prispevek podaja informacijo o možnih razvojih in ustreznostih uporabe SAC zlitin v prenosnih elektronskih izdelkih.

Ključne besede: SnAgCu spajke, vsebnost srebra, mehanične lastnosti, mikrostrukturne lastnosti, termično ciklanje, vpliv padca

* Corresponding Author's e-mail: dhafer_eng@yahoo.com

1. Introduction

Currently, the trend in portable electronic products such as the handheld computer, mobile phone, Personal Digital Assistant (PDA) and digital camera toward miniaturization and multi-functionality, has led to electronic packages with higher density and smaller dimension, e.g. the smaller solder interconnections of Ball Grid Array (BGA) and Chip Scale Package (CSP) (Zhang, Ding et al. 2009). For portable electronic prod-

ucts, board-level solder joint reliability due to drop impact load and thermal cycling load is of great concern. The mechanical loads resulting from mishandling during transportation or customer usage may cause solder joint failure, which leads to malfunctioning of the product. Normally, mobile phones are designed to withstand a number of accidental drops to the floor from a height of 1.5 m, without resulting in major mechanical or functional failures (Tee, Ng et al. 2003). Besides, during use, portable electronic products are subject

to temperature cycles load, induced by environmental temperature change and power on-off cycles. A typical temperature cycling test condition of -40°C to 125°C is required to ensure a reliable package performance (Tee, Ng et al. 2003; Zhang, Ding et al. 2009). There are few publications related to integrated design analysis of board-level solder joint reliability, with consideration of both drop impact load and thermal cycling load performance simultaneously.

Overall solder joint reliability is determined by the combination of service environment and system design. The service environment will determine the temperature extremes which the product must endure, the frequency of power on / off cycling, and the possibility of specific mechanical shocks (for example, drop impact) stresses. Where the system design is concerned, a series of factors that include component and substrate physical properties, solder joint geometry, bulk solder alloy microstructure and mechanical properties, the nature of the IMC layer formed and their structure at the solder joint / pads interfaces are important. Cost limitations add additional constraints, forcing hard choices to be made (Tu 2007). The robustness of a solder joint subjected to both temperature cycles load and drop impact load is influenced by a complex combination of bulk solder alloy properties and IMC layer properties (Grafe, Garcia et al. 2008). For bulk solder alloys, eutectic tin-lead, with its long established history, has been replaced with the complexity of a multitude of new and unfamiliar lead-free alloys. SAC is now recognized as the standard lead free solder alloy for packaging interconnects in the electronics industry. However, Sn-Ag-Cu alloys are not enough to meet high solder joint reliability under different loading conditions. This study present the direct correlation between mechanical and microstructure properties of SAC bulk solder alloy and the reliability of SAC solder joints in term of both drop impact and thermal cycling loading conditions.

2. Sn-Ag-Cu lead-free solders series

Of the many lead-free solder series proposed in the last decade or so, Sn-Ag-Cu (SAC) series alloys have emerged as the most widely accepted as shown in Figure 1 Soldertec's survey shows that the most popular SAC are the near eutectic SAC alloys (Nimmo 2002), which consist of 3.0–4.0% of Ag and 0.5–1.0% of copper as shown in Figure 2. The melting point of these near eutectic SAC alloys is 217°C, which is lower than the 96.5Sn–3.5Ag binary eutectic alloy at 221°C. In the SAC system, the addition of Cu both lowers the melting temperature and improves the wettability (K. Nimmo 2004). Figure 3 is the top view (2-D) of the ternary phase diagram of Sn-Ag-Cu (Ma and Suhling 2009).

The area indicated in the red box is the near eutectic region. Most of the SAC alloy compositions currently in the market are within this region.

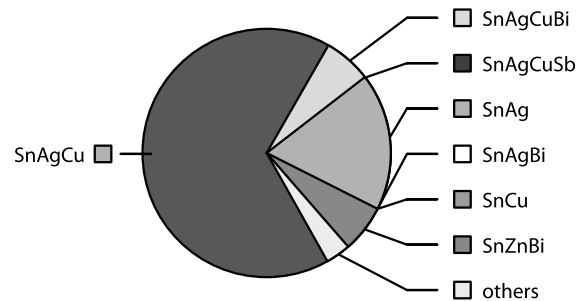


Figure 1: The market share of different lead-free solders (Nimmo 2002).

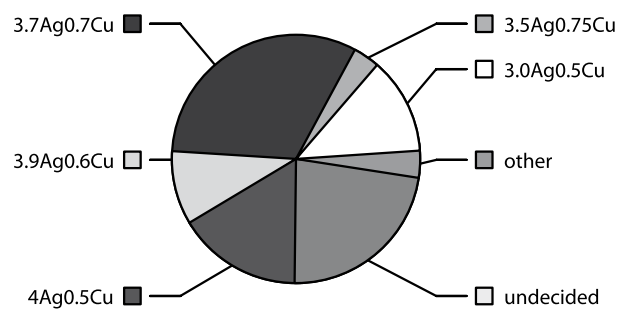


Figure 2: Survey of the market share of different types of SAC alloys (Nimmo 2002).

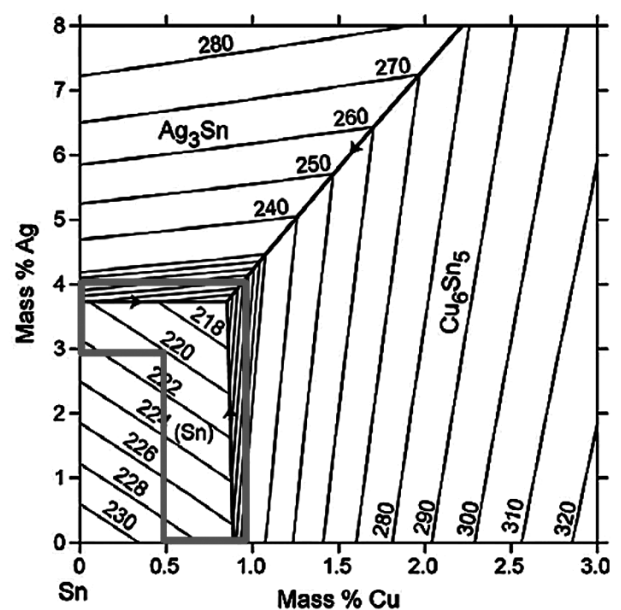


Figure 3: Sn-Ag-Cu ternary phase diagram (Ma and Suhling 2009).

3. Microstructure characteristics and mechanical properties of the Sn-xAg-Cu bulk solder

It is well known that, to a large extent, the microstructural characteristics of an alloy determine its mechanical performance (Allen 1969; R.F Smallman 1999; Hosford 2005). The microstructure development of a solder joint is affected by the alloy system and process conditions during solder joint formation (Moon, Boettinger et al. 2000; Pang, Tan et al. 2001; Anderson 2007). Therefore, understanding the micro-structural characteristics of the SAC ternary system is essential to understanding the mechanical performance and reliability of Sn-Ag-Cu solders. These properties provide design and manufacturing engineers with the necessary information when deciding on a solder alloy for their specific application.

Silver is an essential element in SAC composition which can have different effects on the solder joint reliability, depending on the loading conditions. Currently, a wide variety of SAC solders containing different levels of silver, and maintaining a Cu level to manage substrate dissolution, such as Sn-1Ag-0.5Cu (SAC105) and Sn-3Ag-0.5Cu (SAC305), have been studied and are in use in the electronics industry for a wide range of applications. Kariya and his coworkers investigated the as-soldered microstructure or initial microstructure of Sn-xAg-Cu shown in Figure 4 (Kariya, Hosoi et al. 2004). They found that the microstructures of Sn-xAg-Cu alloy consisted of a β -Sn matrix with dispersoids of fine Ag_3Sn and coarsened Cu_6Sn_5 inter-metallic compounds (IMC particles) (Terashima, Kariya et al. 2003; Kariya, Hosoi et al. 2004). The size of the IMC particles varied from submicron to several microns for all alloys, which is a common feature of the Sn-xAg-Cu alloys (Kariya and Plumbridge 2001). Volume fraction of the Ag_3Sn IMC particles in the microstructure tends to increase with increasing silver content. In the microstructure of SAC105, relatively large primary Sn grains and the Ag_3Sn IMC particles appeared sparsely within the matrix (Terashima, Kariya et al. 2003; Kariya, Hosoi et al. 2004). The SAC205 had cell-like primary Sn grains, and the grains were decorated with the very fine Ag_3Sn IMC particles. In the SAC305, the Ag_3Sn IMC particles formed a network structure around the primary Sn grains, and the size of the Sn grains was larger than that of the 2Ag solder. In the SAC405 alloy, the Ag_3Sn IMC particles compounds were finely dispersed within the matrix, and the inter-particle distance was smaller than that in other alloys (Terashima, Kariya et al. 2003; Kariya, Hosoi et al. 2004).

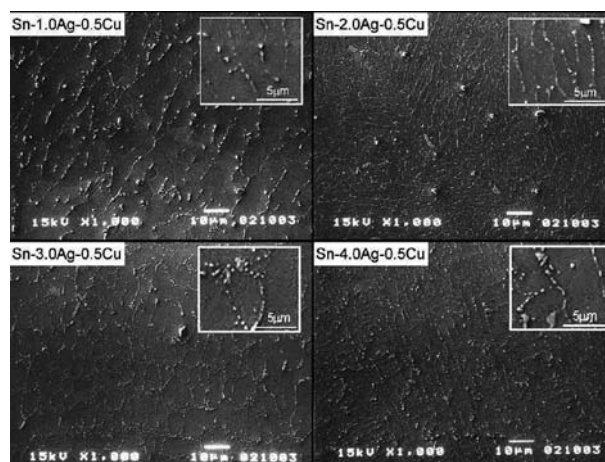


Figure 4: The initial microstructure of Sn-xAg-Cu bulk solders (Kariya, Hosoi et al. 2004).

The Ag_3Sn and Cu_6Sn_5 IMC particles possess much higher strength than the bulk material in SAC solder (R. J. Fields ; Tsai, Tai et al. 2005), while primary Sn has the lowest elastic modulus and lowest yield strength among the constituent phases in SAC solder (Kim, Suh et al. 2007; Suh, Kim et al. 2007), as shown in Table 1 (Kim, Suh et al. 2007). Fine IMC particles in the Sn matrix can therefore strengthen the alloys (S. Ganesan 2006). The number or volume fraction of the Ag_3Sn IMC particles in the microstructure of SAC solder alloy tends to increase with increasing silver content as shown in Figure 4 (Terashima, Kariya et al. 2003; Kariya, Hosoi et al. 2004); hence, high Ag content SAC solder (SAC305/SAC405) yields large numbers of Ag_3Sn IMC particles and small size of primary Sn grains. Therefore this is expected to increase the elastic modulus and yield strength and reduce the ductility of the solder (Che, Luan et al. 2008; Che, Zhu et al. 2010), as shown in Table 2 (Henshall, Healey et al. 2009). On the other hand, low Ag content SAC alloy (SAC105) gives rise to more primary Sn phase (large Sn grains) and decreased number of Ag_3Sn IMC particles as shown in Fig. 1. It is therefore expected to result in lower elastic modulus and lower yield strength than high Ag content SAC alloy (SAC 305) (Che, Luan et al. 2008; Che, Zhu et al. 2010)[39, 40], as shown in Table 2 (Henshall, Healey et al. 2009).

Table 1: Key material properties of constituent phases in SAC alloys (Henshall, Healey et al. 2009)

| Phase | E [GPa] | KIC [MPa√m] | HV [Kg/mm ²] |
|-------------------------------------|---------|-----------------------------------|--------------------------|
| Cu₆Sn₅ | 93.5 | 1.4 to 2.73 | 351-378 |
| Ag₃Sn | 74.5 | > Cu ₆ Sn ₅ | 142-120 |
| Sn | 42-50 | Very high | 100 |

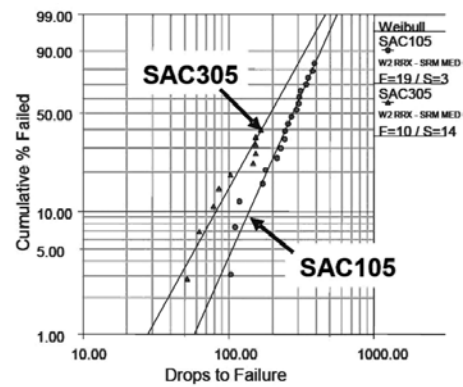
Table 2: Mechanical properties of SAC alloys vs. eutectic SnPb (Henshall, Healey et al. 2009)

| Solder alloy | Primary Sn | Modulus (GPa) | Modulus Reduction | UTS (Mpa) | Elong (%) |
|-------------------|------------|---------------|-------------------|-----------|-----------|
| SAC (4%Ag) | none | 53.3 | baseline | 52.4 | 35 |
| SAC (3%Ag) | 10% | 51.0 | -4% | 53.3 | 46 |
| SAC (1%Ag) | 35% | 47.0 | -12% | 45.2 | 46 |
| Sn-Pb | n/a | 40.2 | -25% | | 50 |

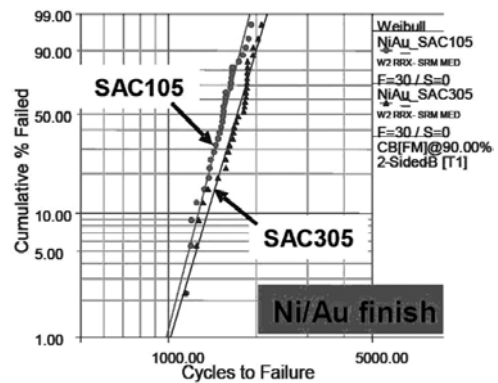
4. Limitation of SAC solder joints

A wide variety of SAC solders containing different levels of silver has been studied and is in use in electronics industry for a wide range of applications currently. The content level of silver in SAC solder alloys can be an advantage or a disadvantage depending on the application, package and reliability requirements (Henshall, Healey et al. 2009), e.g. the best level of silver content for drop performance is not necessarily the best level for optimum temperature cycling reliability (Syed, Scanlan et al. 2008). Hence, the SAC alloys are limited in their potential applications in the portable electronic products in which thermal cycling and drop/impact are the primary requirement for board level solder joint reliability.

The SAC105 and SAC305 solder ball joints for BGA interconnections (board level package) were evaluated under temperature cycling and drop (JESD22-B111) tests. The data indicates that lower silver content solder balls perform better under drop conditions, while temperature cycling reliability suffers as silver content decreases (Syed, Scanlan et al. 2008). In other words, SAC105 solder balls show better performance than SAC305 under drop loading conditions (see Figure 5a). However, the trend is reversed for temperature cycle test (see Figure 5b). The data show how the level of silver content in SAC composition can have a different effect on the board level solder joint performance depending on the loading conditions.



(a) Drop test



(b) Temperature cycle test

Figure 5: Drop and temperature cycling performance for NiAu finish packages.

5. Direct correlation between bulk SAC solder properties and drop impact reliability

Currently, high Ag SAC alloys (SAC305/SAC405) are the most common material systems for the Pb-free board level solder joints in electronic industry. However, these alloys exhibit significantly low robust in terms

of high strain rate response such as drop impact conditions due to the lack of the compliance of the bulk solder materials and complex IMC formation at the solder/metal interface (Kim, Suh et al. 2007; Suh, Kim et al. 2007). The root cause of the poor high strain rate response of high Ag SAC alloys (SAC305/SAC405) lies in the bulk alloy properties (Pang and Che 2006; Pandher, Lewis et al. 2007). These high Ag alloys have high yield strength and elastic modulus and low acoustic impedance, resulting in a high bulk solder strength. Therefore under drop impact loading conditions, they more readily transfer stress to the interface IMC layers. The interface IMC layers formed during soldering are of low ductility and it is this interface that exhibits brittle fracture (Pandher, Lewis et al. 2007; Che, Luan et al. 2008; M. P. Renavikar 2008; Che, Zhu et al. 2010; Yu, Jang et al. 2010). The high yield strength and elastic modulus of the high Ag alloys is derived primarily from the precipitation hardening of the tin matrix by the Ag_3Sn IMC particles and fine Sn grain size, result in a strong and stiff bulk solder (Che, Poh et al. 2007).

The first approach to improve the drop impact performance of SAC alloys is to optimize the bulk solder properties by reducing the silver content to as low as Ag < 2 wt% (SAC105) (Syed, Kim et al. 2006; Pandher, Lewis et al. 2007). The low Ag alloys are found to have low yield strength and elastic modulus, and high ductility (Che, Poh et al. 2007; Che, Luan et al. 2008; Che, Zhu et al. 2010). This means low Ag alloys have high elastic compliance and high plastic energy dissipation ability during crack propagation which effectively toughens the crack tip and prolongs the time to reach the critical stress for the fracture under high-strain rate conditions (Kim, Suh et al. 2007). As a result low Ag alloys can dissipate more high strain rate energy through bulk solder deformation and reduce the dynamic stress transformed to interface IMC layers, resulting in good drop impact performance. The low strength properties of low Ag alloys can be attributed to large Sn grain size or more Sn primary phase (see Figure 6) and sparsely distributed Ag_3Sn IMC particles in the bulk alloy matrix, which result in a soft bulk solder (Pandher, Lewis et al. 2007; M.P. Renavikar 2008; Yu, Jang et al. 2010). The shear strength for the SAC family of alloys is shown in Figure 7. Clearly lower Ag alloys have an advantage in potentially absorbing the effect of high strain rate deformation (Pandher, Lewis et al. 2007). The second approach is to optimize the interface reaction to improve the strength of the IMC layer via adding other elements in the SAC system which can effectively modify the interface reaction (Pandher, Lewis et al. 2007; Kittidacha, Kanjanavikat et al. 2008).

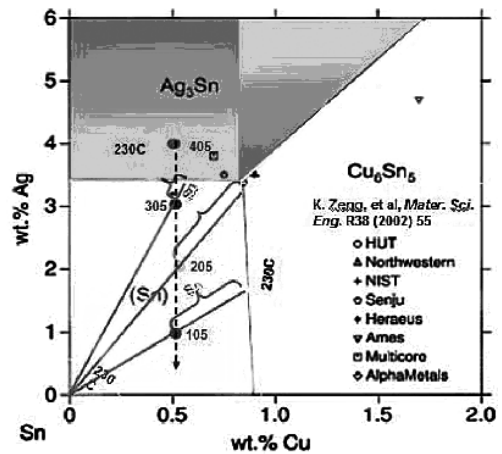


Figure 6: Sn-rich region of Sn-Ag-Cu ternary phase diagram. Variation of Ag content (with fixed Cu content of 0.5%) is indicated by vertical line. The tie line is also shown for representative SAC alloys (Kim, Suh et al. 2007).

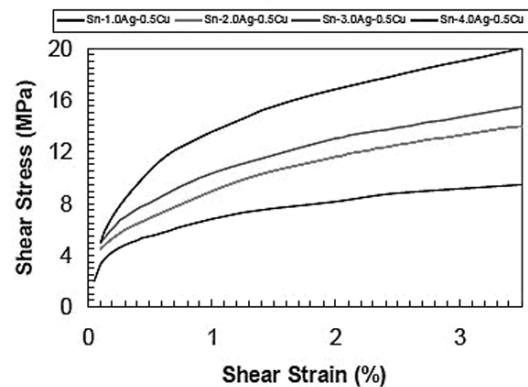


Figure 7: Mechanical (shear) properties of SAC alloys as a function of Ag content (Pandher, Lewis et al. 2007).

6. Direct correlation between bulk SAC solder properties and thermal cycling reliability

The thermal mechanical strain and elevated temperature during thermo-mechanical loading induces re-crystallization in the highly strained region of the bulk solder, leading to the development of thermo-mechanical fatigue cracks in the re-crystallized regions along large angle grain boundaries (Mattila 2005; Frear, Ramanathan et al. 2008). Hence, the degree of the coarsening indicates an accumulation of the strain or the stress imposed by the thermo-mechanical fatigue process.

The optimal silver content in the Sn-x Ag-Cu alloy is of great significance for designing a solder that has greater

thermo-mechanical fatigue resistance (Terashima, Kariya et al. 2003). One of the most detailed studies on thermo-mechanical fatigue failure rate of Sn-x Ag-Cu solder joints was conducted by Terashima et al. 2003 who found that increasing Ag content increases the fatigue resistance of SAC solder. Their results, summarized in Figure 8, show that the 1Ag solder had the fastest failure rate while the 4Ag solder had twice the cycles to first failure (No) as the 1Ag solder. They observed that the 3Ag and 4Ag solder joints suppressed micro-structural coarsening, which degrades fatigue resistance, whereas a significant micro-structural coarsening occurs in the 1Ag and 2Ag solders because of the thermo-mechanical fatigue process. As compared with Figures 9 and 10, the Sn grains were coarsened, and the number of the Ag_3Sn dispersions decreased drastically as a function of the number of thermal cycles compared with the initial microstructures for the 1Ag and the 2Ag solders. While grain coarsening was not significant in the 3Ag and the 4Ag solders, these alloys retained the fine Ag_3Sn dispersions even after thermal cycling.

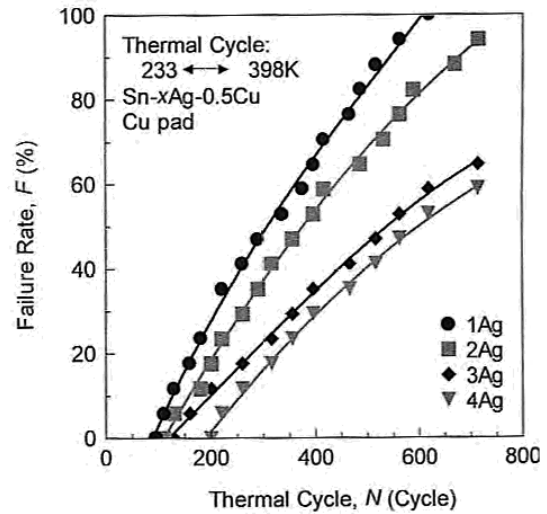


Figure 8: Effect of thermal cycles on the failure rate of Sn-xAg-0.5Cu (x = 1, 2, 3, and 4) solder joints on the Cu pads (Terashima, Kariya et al. 2003).

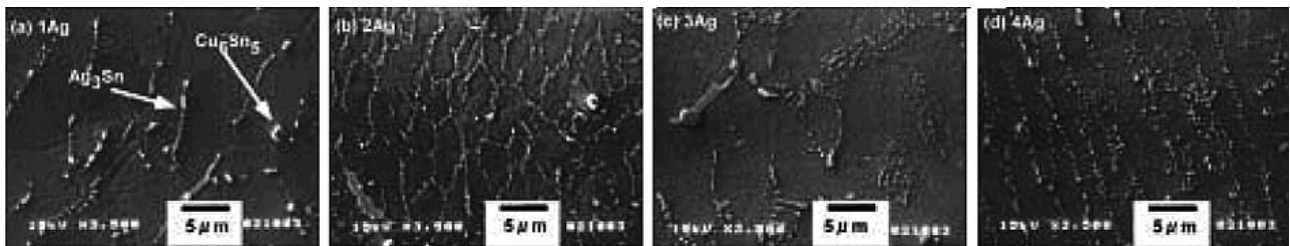


Figure 9: The initial microstructure for each Sn-xAg-0.5Cu solder joint: (a) 1Ag, (b) 2Ag, (c) 3Ag, and (d) 4Ag (Terashima, Kariya et al. 2003).

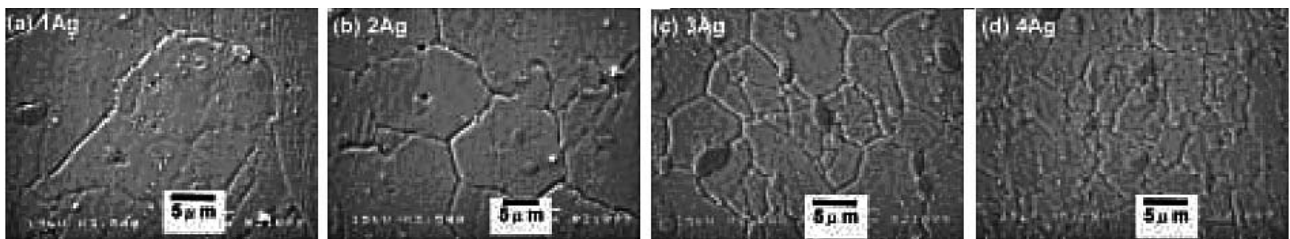


Figure 10: The microstructures at the center area for each Sn-xAg-0.5Cu solder joints after 600 cycles a) 1Ag, (b) 2Ag, (c) 3Ag, and (d) 4Ag (Terashima, Kariya et al. 2003).

It has been reported that the SAC solder has a dispersion or precipitation strengthening mechanism (Kariya, Hirata et al. 1999; Zhang, Li et al. 2002). Thus, the dispersion morphology of the Ag_3Sn IMC particles strongly affects the mechanical properties of the SAC solder. Namely, if the microstructure of an alloy has finely dispersed Ag_3Sn particles like SAC405 solder alloy, the alloy and Sn grains may show high strength bulk solder because of the Orowan looping of dislocations. Moreover, if coarsening of an alloy is inhibited because of the

finely dispersed Ag_3Sn , a good fatigue resistance can be expected as a result of suppressing plastic deformation of the solder (Ye, Lai et al. 2001; Subramanian and Lee 2003; Terashima, Kariya et al. 2003; Kariya, Hosoi et al. 2004). Furthermore, if the Ag_3Sn IMC particles form a eutectic network structure around Sn grains like SAC305 solder, a good fatigue resistance can be expected as a result of inhibiting micro-structural coarsening due to Zener pinning effect (Dieter 1981; Subramanian and Lee 2003; Liu, Lee et al. 2009; Terashima,

Kohno et al. 2009). In other words, the micro-structural coarsening suppression (grain size stability) can be attributed to the pinning of Sn grains boundary by the fine Ag_3Sn IMC particles due to the atomic matching, or coherency, between the lattices of the precipitates and the matrix. On the other hand, T. Kobayashi and his co-researchers studied the crack propagation morphology of SAC 105 solder joints subjected to a fatigue test. They observed that cracks were nucleated at the interface of primary $\beta\text{-Sn}$, where eutectic phase is not always observed. Hence the strength of the interface between primary $\beta\text{-Sn}$ to be lower than that of the primary $\beta\text{-Sn}$ interface, filled with the eutectic phase, resulting in poor fatigue resistance of SAC105 solder (Kobayashi, Kariya et al. 2007).

7. Conclusion

The Ag_3Sn and Cu_6Sn_5 IMC particles in the bulk SAC solder have much higher elastic modulus and yield more strength than the bulk material. Large amount of fine Ag_3Sn and Cu_6Sn_5 IMC particles in the Sn matrix can therefore strengthen the bulk SAC solder. On the other hand, among the constituent phases in bulk SAC solder, primary Sn has the lowest elastic modulus and yield strength. The role of Ag and Cu in SAC alloys is a straightforward issue of Cu_6Sn_5 and Ag_3Sn strengthening the Sn matrix. However, a Cu level is maintained to manage substrate dissolution. High Ag content SAC solder (SAC305/SAC405) produce large number of fine Ag_3Sn IMC particles and small sized of Sn primary grains, which make the bulk solder exhibit high strength. This will help to suppress the plastic deformation during the thermo-mechanical fatigue process. Moreover, the large number of fine Ag_3Sn IMC particles in SAC305 bulk solder forms a eutectic network structure around the primary Sn grain and suppresses the grain coarsening, which results in good thermo-mechanical fatigue cracks resistance. However the stiff or strong bulk high Ag solder prevents the drop impact energy from dissipating through the bulk solder, thereby transferring more stress to the interface IMC layers which cause brittle fracture of the solder joint. Low Ag content will decrease the strength and elastic modulus of the solder, transferring less stress to the IMC layers. This is due to increasing the amount of primary Sn relative to the Ag_3Sn and Cu_6Sn_5 phases in the low Ag alloy, which make the bulk solder more compliant. However, the low Ag alloy shows poor thermal cycling reliability due to fewer number of Ag_3Sn IMC particles compared to high Ag alloy. The content level of silver in SAC solder alloys can be an advantage or a disadvantage depending on the application, package and reliability requirements. Hence, it is highly recommended to improve both the strength and ductility of the bulk SAC

solder through SAC optimization for optimal solder ball attachments in portable electronic products.

Acknowledgement

The authors would like to acknowledge the financial support provided by the Institute of Research Management and Consultancy, University of Malaya (UM) under the IPPP Fund Project No.: PS117/2010B

Reference

1. Allen, D. K. (1969). Metallurgy theory and practice. Homewood, IL USA, American Technical Publishers.
2. Anderson, I. E. (2007). "Development of Sn-Ag-Cu and Sn-Ag-Cu-X alloys for Pb-free electronic solder applications." Lead-Free Electronic Solders: 55-76.
3. Che, F., J. Luan, et al. (2008). Effect of silver content and nickel dopant on mechanical properties of Sn-Ag-based solders, IEEE.
4. Che, F., J. Luan, et al. (2008). Effect of silver content and nickel dopant on mechanical properties of Sn-Ag-based solders. ECTC, IEEE.
5. Che, F., E. C. Poh, et al. (2007). Ag Content Effect on Mechanical Properties of Sn-xAg-0.5 Cu Solders. ECTC, IEEE.
6. Che, F., W. Zhu, et al. (2010). "The study of mechanical properties of Sn-Ag-Cu lead-free solders with different Ag content and Ni doping under different strain rates and temperatures." Journal of Alloys and Compounds.
7. Dieter, G. E. (1981). Mechanical metallurgy. TOKYO, McGRAW-HILL.
8. Frear, D., L. Ramanathan, et al. (2008). Emerging reliability challenges in electronic packaging. Annual International Reliability Physics Symposium, IEEE.
9. Grafe, J., R. Garcia, et al. (2008). "Reliability and Quality Aspects of FBGA Solder Joints." FORSCHUNG & TECHNOLOGIE 10: 2224-2234.
10. Henshall, G., R. Healey, et al. (2009). Addressing opportunities and risks of pb-free solder alloy alternatives, IEEE.
11. Hosford, W. F. (2005). Physical metallurgy. Boca Raton, FL USA, CRC Press, Taylor and Francis Group.
12. K. Nimmo (2004). Alloy selection. New York, Marcel Dekker.
13. Kariya, Y., Y. Hirata, et al. (1999). "Effect of thermal cycles on the mechanical strength of quad flat pack leads/Sn-3.5 Ag-X (X= Bi and Cu) solder joints." Journal of electronic materials 28(11): 1263-1269.
14. Kariya, Y., T. Hosoi, et al. (2004). "Effect of silver content on the shear fatigue properties of Sn-Ag-Cu flip-chip interconnects." Journal of electronic materials 33(4): 321-328.

15. Kariya, Y. and W. Plumbridge (2001). Mechanical properties of Sn-3.0 mass% Ag-0.5 mass% Cu alloy.
16. Kim, D., D. Suh, et al. (2007). Evaluation of high compliant low Ag solder alloys on OSP as a drop solution for the 2nd level Pb-free interconnection, IEEE.
17. Kittidacha, W., A. Kanjanavikat, et al. (2008). Effect of SAC Alloy Composition on Drop and Temp cycle Reliability of BGA with NiAu Pad Finish. ECTC, IEEE.
18. Kobayashi, T., Y. Kariya, et al. (2007). Effect of Ni Addition on Bending Properties of Sn-Ag-Cu Lead-Free Solder Joints. ECTC, IEEE.
19. Liu, W., N. C. Lee, et al. (2009). Achieving high reliability low cost lead-free SAC solder joints via Mn or Ce doping. ECTC, IEEE.
20. M.P. Renavikar, N. P., A. Dani, V. Wakharkar, G. Arrigotti, V. Vasudevan, O. Bchir, A.P. Alur, C.K. Gurumurthy, R.W. Stage (2008). "Materials technology for environmentally green micro-electronic packaging." Intel® Technology Journal 12: 1-16.
21. Ma, H. and J. C. Suhling (2009). "A review of mechanical properties of lead-free solders for electronic packaging." Journal of materials science 44(5): 1141-1158.
22. Mattila, T. (2005). Reliability of high-density lead-free solder interconnections under thermal cycling and mechanical shock loading. Espoo, Finland, Helsinki University of Technology.
23. Moon, K. W., W. Boettinger, et al. (2000). "Experimental and thermodynamic assessment of Sn-Ag-Cu solder alloys." Journal of electronic materials 29(10): 1122-1136.
24. Nimmo, K. (2002). European Lead-free Technology Roadmap, Ver1: February 2002, Soldertec at Tin Technology Ltd.
25. Pandher, R. S., B. G. Lewis, et al. (2007). Drop shock reliability of lead-free alloys-effect of micro-additives, IEEE.
26. Pang, H., K. Tan, et al. (2001). "Microstructure and intermetallic growth effects on shear and fatigue strength of solder joints subjected to thermal cycling aging." Materials Science and Engineering: A 307(1-2): 42-50.
27. Pang, J. H. L. and F. Che (2006). Drop impact analysis of Sn-Ag-Cu solder joints using dynamic high-strain rate plastic strain as the impact damage driving force, IEEE.
28. R. J. Fields, S. R. L. "Physical and mechanical properties of intermetallic compounds commonly found in solder joints." Retrieved April 20, 2011, 2011, from http://www.metallurgy.nist.gov/mechanical_properties/solder_paper.html.
29. R.F Smallman, R. J. B. (1999). Modern physical metallurgy and materials engineering. Oxford, Butterworth- Heinemann
30. S. Ganesan, M. P. (2006). Lead-free electronics. New York, Wiley-Interscience Publication.
31. Subramanian, K. and J. Lee (2003). "Physical metallurgy in lead-free electronic solder development." JOM Journal of the Minerals, Metals and Materials Society 55(5): 26-32.
32. Suh, D., D. W. Kim, et al. (2007). "Effects of Ag content on fracture resistance of Sn-Ag-Cu lead-free solders under high-strain rate conditions." Materials Science and Engineering: A 460: 595-603.
33. Syed, A., T. S. Kim, et al. (2006). Alloying effect of Ni, Co, and Sb in SAC solder for improved drop performance of chip scale packages with Cu OSP pad finish. ECTC, IEEE.
34. Syed, A., J. Scanlan, et al. (2008). Impact of package design and materials on reliability for temperature cycling, bend, and drop loading conditions. IEEE-ECTC, IEEE.
35. Tee, T. Y., H. S. Ng, et al. (2003). Design for enhanced solder joint reliability of integrated passives device under board level drop test and thermal cycling test, IEEE.
36. Terashima, S., Y. Kariya, et al. (2003). "Effect of silver content on thermal fatigue life of Sn-xAg-0.5 Cu flip-chip interconnects." Journal of electronic materials 32(12): 1527-1533.
37. Terashima, S., T. Kohno, et al. (2009). "Improvement of thermal fatigue properties of Sn-Ag-Cu lead-free solder interconnects on Casio's wafer-level packages based on morphology and grain boundary character." Journal of electronic materials 38(1): 33-38.
38. Tsai, I., L. J. Tai, et al. (2005). Identification of Mechanical Properties of Intermetallic Compounds on Lead Free Solder, IEEE; 1999.
39. Tu, K. (2007). Solder joint technology: materials, properties, and reliability, Springer Verlag.
40. Ye, L., Z. Lai, et al. (2001). "Microstructure investigation of Sn-0.5 Cu-3.5 Ag and Sn-3.5 Ag-0.5 Cu-0.5 B lead-free solders." Soldering & surface mount technology 13(3): 16-20.
41. Yu, A., J. W. Jang, et al. (2010). Improved reliability of Sn-Ag-Cu-In solder alloy by the addition of minor elements. ECTC, IEEE.
42. Zhang, B., H. Ding, et al. (2009). "Reliability study of board-level lead-free interconnections under sequential thermal cycling and drop impact." Microelectronics Reliability 49(5): 530-536.
43. Zhang, F., M. Li, et al. (2002). "Failure mechanism of lead-free solder joints in flip chip packages." Journal of electronic materials 31(11): 1256-1263.

Arrived: 28. 04. 2011

Accepted: 26. 1. 2012

Quality Control of Automotive Switches with help of Digital Camera

Grega Bizjak*, Matej Bernard Kobav, Blaž Luin

Univerza v Ljubljani, Fakulteta za elektrotehniko

Abstract: For the purpose of quality control at one Slovenian automotive parts producer a system for luminance measurement based on digital camera was developed. The system consists of black chamber in which the measured specimen and the camera are placed. They are positioned very close to each other with the distance between them limited with the minimal focus distance of the camera which is about few millimeters. Such a short distance assures that in spite of rather small symbol on a car switch there is still enough information on the picture that the luminance of the symbol can be calculated.

Special software automatically takes the picture, transfers it into the computer and analyzes it according to the car manufacturer standard. First the boundaries of the symbol are located on the pictures and then the measurement areas are found. In the next step, the luminance of the measured area is calculated. On one symbol two or three measuring areas are defined. If the luminance of the measuring areas is in the allowed interval, the switch is adequate to be mounted in a car, if not, the switch must be discarded. The result of the analysis (adequate, not adequate) is clearly stated on the screen. As whole measuring process is automatic no special knowledge is needed to manage the measuring system.

Keywords: quality control, automotive industry, digital image processing, luminance measuring with digital camera

Kontrola kakovosti avtomobilskih stikal s pomočjo digitalne kamere

Izvleček: V proizvodnji sestavnih delov za avtomobilsko industrijo je ustrezna končna kontrola izdelkov danes obvezna. V okviru končne kontrole pa je potrebno izdelek zanesljivo in čim hitreje preveriti. Zato je bil za slovenskega izdelovalca stikal za vgradnjo v avtomobile izdelan sistem za končno kontrolo svetlosti znakov na stikalih. Sistem temelji na uporabi digitalne kamere in ustrezne programske opreme. V članku je najprej predstavljena metoda meritve svetlosti osvetljenih simbolov na avtomobilskih stikalih. Namesto klasičnega merilnika svetlosti in črne sobe je pri opisanem postopku uporabljena digitalna kamera ter posebna črna komora. V komori sta merjeno stikalo in digitalna kamera nameščena na ustrezno kratki razdalji, ki omogoča ostro zajemanje slike, ustrezno razpoznavanje detajlom na sliki in izračun svetlosti simbola na stikalu. Z digitalno kamero najprej zajamemo sliko osvetljenega simbola in jo prenesemo na računalnik. S posebno programsko opremo se slika nato obdelava, poiščejo se meje osvetljenega simbola in izračunajo se svetlosti referenčnih točk. Na podlagi izračunanih svetlosti se poda ocena o skladnosti testiranega vzorca z proizvajalčevim standardom. Rezultat analize (ustrezno, neustrezno stikalo) se jasno izpiše na zaslonu računalnika. Na posameznem simbolu se lahko upošteva dve ali več referenčnih točk. Celoten postopek od zajema slike preko določitve meja simbola, izračuna svetlosti in ocene ustreznosti je popolnoma avtomatiziran. Tako lahko z napravo rokujejo tudi delavci brez posebnega znanja o fotometriji in merjenju svetlosti. Kljub temu da je metoda za razliko od klasične meritve svetlosti precej hitrejša in lažje izvedljiva še vedno zagotavlja ustrezno zanesljivost. Poleg tega pa so tudi stroški za potrebna oprema precej nižji kot pri klasični merilni opremi. Tako sama naprava kot tudi programska oprema sta bili razviti v laboratoriju za razsvetljavo in fotometrijo na ljubljanski Fakulteti za elektrotehniko.

Ključne besede: kontrola kakovosti, avtomobilska industrija, obdelava digitalnih slik, meritev svetlosti z digitalno kamero

* Corresponding Author's e-mail: grega.bizjak@fe.uni-lj.si

1. Introduction

For the purpose of quality control at one Slovenian automotive parts producer a system for luminance measurement based on digital camera was developed at Laboratory of Lighting and Photometry. The

products are different switches for the car interior for a large European car manufacturer. Due to the strong demands of the company internal standardization the parts producer needs to have efficient quality control in order to preserve orders. To control the luminance of the symbol on switches, the Slovenian produces had

two possibilities. One was the use of a luminance meter in a dark room. This measuring procedure needs a lot of time and some special equipment like a dark room, photometric bench etc. are needed together with the luminance meter. It is also very difficult to measure luminance of very small surfaces, illuminated with almost monochromatic light, at a short distance. The second possibility was the use of a luminance measuring device, based on digital camera.



Figure 1: Developed device for measurement of luminance of symbols on car switches.

In close cooperation with the mentioned Slovenian automotive parts producer such a luminance measuring device was developed in the Laboratory of lighting and photometry. First, the prototype device was constructed based on the commercial digital camera with 5 million pixels and possibility to control it through a USB port. The device was tested in the production quality control and proved to be very useful although clumsy to use due to some construction details [3]. So the second device, described in this paper, was constructed.

2. Design of the Black chamber

To prevent the external light sources to disturb the measuring results the measured switch and the camera were placed in a black chamber. Apart from this the chamber, build as a small cabined, also provides a power supply for the camera and switch sample and a USB connection for the camera. Inside the container is painted black to prevent light reflections. To enable easy exchange of the measured specimens, both the specimen and the camera are placed on the drawers.

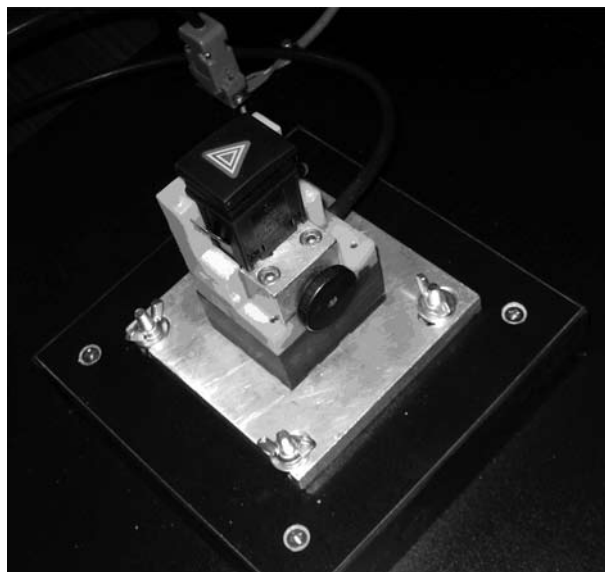


Figure 2: Measured specimen mounted on a stand in a drawer.



Figure 3: Digital camera is positioned on the top of the measured specimen.

The measured specimen of a car switch is mounted on a special stand in the drawer (Figure 2) and connected to the power supply. The digital camera is mounted in the second drawer on top of the measured specimen (Figure 3). The specimen and the camera are positioned and adjusted so, that the distance between the specimen and camera lens assures focused picture at the closest possible distance. The camera is connected to the power supply and to the computer with the USB cable. After specimen is mounted on the stand, the drawer is closed to provide a total darkness inside the chamber.

3. Choice of the camera

There are many different digital cameras on the market. But to be suitable for our application, the camera should fulfil following criteria:

- the light sensitivity should be adequate to luminance range of measured symbols;
- the minimal focus distance should be short enough so the taken picture of symbol covers most of the canvas;
- it must be possible to control the camera remotely from the computer via USB port.

First requirement is that the camera is able to sense luminance range we were about to measure. The luminance of the symbols on car switches is normally in range from 2 to 60 cd/m². Nearly every consumer camera fulfils this requirement. Ability to focus to a short distance of approximately 20 mm as the switch is relatively small significantly narrowed our choice of suitable cameras. The last important requirement is that the camera can be completely remotely controlled. This means that it should be possible to remotely set zoom, focus distance, aperture width and shutter speed. To sum up image should be remotely captured and transferred to the computer. Most of the remote controllable cameras use protocol PTP (picture transfer protocol), which is standardized as ISO 15740. Its default network transport media is USB (universal serial bus).

The camera that fulfilled our requirements is a consumer model Canon G7. Apart from this one, there are many other suitable cameras on the market.

4. Segmentation of the captured image and calculation of the luminance

After the sample has been put into the chamber and turned on, the image is captured and transferred to the software on computer. To be able to calculate the luminance of the symbol, first the boundaries of the illuminated symbol have to be found. This is accomplished by detecting the outer edges on all sides of the symbol. Therefore the procedure depends on the shape of the sign. In the following example we present a procedure for a nearly rectangular shaped sign like on the switch for heating the back window. In this case we have to detect four outer edges.

A first point on a left vertical edge is found by searching from left to the right for the first point in a row at which an increase in light intensity is larger than a predefined threshold.

$$V_l = \{(x, y)\}, i(x, y) - i(x - 1, y) > T, x = 0, x \rightarrow x_{max} \quad (1)$$

where $i(x, y)$ denotes light intensity of a point with coordinates (x, y) and T represents a predefined threshold.

Subsequently points on right vertical edge, upper horizontal and lower horizontal edges are found:

$$V_r = \{(x, y)\}, i(x, y) - i(x + 1, y) > T, x = x_{max}, x \rightarrow 0 \quad (2)$$

$$H_u = \{(x, y)\}, i(x, y) - i(x, y - 1) > T, y = 0, y \rightarrow y_{max} \text{ and} \quad (3)$$

$$H_l = \{(x, y)\}, i(x, y) - i(x, y + 1) > T, x = 0, y_{max} \rightarrow 0. \quad (4)$$

After we find the first point on one edge the direction of the edge is determined using simple linear regression model. For horizontal sets

$$y = \alpha_H + \beta_H x + \epsilon_H, \quad (5)$$

has been used and for vertical sets

$$x = \alpha_V + \beta_V y + \epsilon_V. \quad (6)$$

The estimates of regression parameters for the equation (5) are as follows

$$\hat{\beta}_V = \frac{nS_{XY} - nS_X S_Y}{nS_{XX} - S_X^2}, \quad \hat{\alpha}_H = \frac{S_Y - \hat{\beta}_H S_X}{n} \quad (7)$$

and for the equation (6) as follows

$$\hat{\beta}_V = \frac{nS_{XY} - nS_X S_Y}{nS_{YY} - S_Y^2}, \quad \hat{\alpha}_V = \frac{S_Y - \hat{\beta}_V S_X}{n}, \text{ where} \quad (8)$$

$$S_{XX} = x_1^2 + x_2^2 + \dots + x_n^2 \quad (9)$$

$$S_{YY} = y_1^2 + y_2^2 + \dots + y_n^2 \quad (10)$$

$$S_{XY} = x_1 y_1 + x_2 y_2 + \dots + x_n y_n \quad (11)$$

$$S_X = x_1 + x_2 + \dots + x_n \quad (12)$$

$$S_Y = y_1 + y_2 + \dots + y_n \quad (13)$$

After edges have been determined, corner points $T_i(x_i, y_i)$ can be calculated by finding intersections of the edges. On this basis outer borders of the symbol on a switch are determined. The next step is positioning of the measuring points on the symbol. The measuring points are circular areas on the illuminated part of the symbol. They are placed according to the car producer standard in the corners or in the middle of the lines. The dimension (radius) of the measuring point is 80 % of the symbol line width.

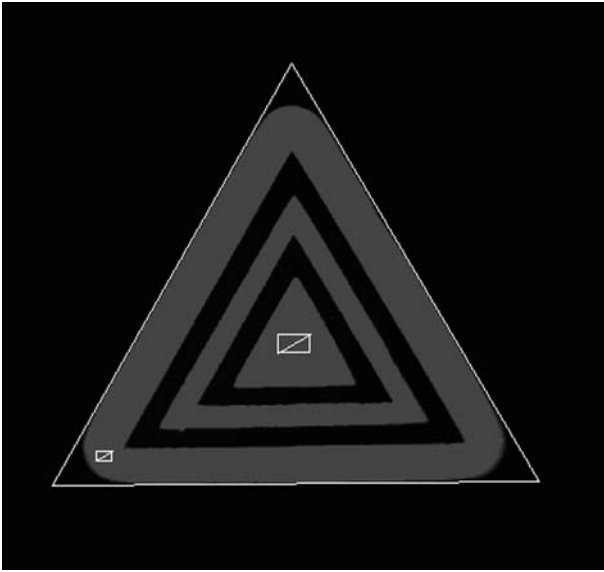


Figure 4: An image of the illuminated switch with edges and measuring points detected automatically and marked.

When measuring points are known, it is necessary to calculate the average luminance of area, which is covered by the measuring point. For that purpose, first the sRGB values of each pixel in the measuring area need to be transformed to CIE Lab color space. This is done by following transformations [2].

- first from sRGB to RGB color space,
- second from RGB to CIE XYZ color space and
- third from CIE XYZ to CIE Lab color space.

All of the sRGB values are converted into RGB values in the same manner. Let R , G and B denote sRGB color values and r , g and b denote RGB color values. Then the transformation among them is defined by the following equations:

$$r = \begin{cases} \frac{R}{12.92}, & R \leq 0.04045 \\ \left(\frac{R + 0.055}{1.055} \right)^{2.4}, & R > 0.04045 \end{cases} \quad (14)$$

$$g = \begin{cases} \frac{G}{12.92}, & G \leq 0.04045 \\ \left(\frac{G + 0.055}{1.055} \right)^{2.4}, & G > 0.04045 \end{cases} \quad (15)$$

$$b = \begin{cases} \frac{B}{12.92}, & B \leq 0.04045 \\ \left(\frac{B + 0.055}{1.055} \right)^{2.4}, & B > 0.04045 \end{cases} \quad (16)$$

With obtained RGB values, it is possible to calculate CIE XYZ values with reference white D65 from them using the following equation:

$$\begin{bmatrix} X \\ Y \\ Z \end{bmatrix} = \begin{bmatrix} r \\ g \\ b \end{bmatrix} \begin{bmatrix} 0.412 & 0.213 & 0.019 \\ 0.357 & 0.715 & 0.119 \\ 0.180 & 0.722 & 0.950 \end{bmatrix} \quad (17)$$

From CIE XYZ color space we calculate lightness component of CIE Lab color space with:

$$L^* = \begin{cases} 116 \sqrt[3]{Y} - 16, & Y > 0.008856 \\ 903.3Y, & Y \leq 0.008856 \end{cases} \quad (18)$$

Finally the luminance of the pixel can be calculated. Relation between the pixel lightness L^* and luminance L is defined by the following equation [1]:

$$L = A(EV)e^{B(EV)L^*}. \quad (19)$$

Therefore our luminance value depends on camera parameter exposition value EV , which is described by the formula:

$$EV = \log_2 \left(\frac{N^2}{t} \right), \quad (20)$$

where N is relative aperture (f-number) and t is shutter speed.

5. Calibration of the device

As one can see from the equation 19, the luminance of the symbol is calculated from the lightness (obtained from the picture data) with help of constants A and B . In the process of calibration the constants A and B should be set so, that the calculated luminance of the measuring point is the same as the luminance of the same point measured with a reference luminance meter. To define constants A and B properly at least two measuring point with different luminance need to be used.

The constants are calculated by regressing average lightness L^* of all pixels inside the measuring point with measured luminance L of the same point on the switch. In order to make calibration successful at least two calibration points with different luminance are required, but in practice we need more points for good accuracy. After constants A and B are properly adjusted, calibration is finished.

As a reference instrument the normal luminance meter class L is used. For the purpose of calibration first the luminance of measuring points on some selected specimens are measured in a dark room of a laboratory

with specimens and instrument mounted on an optical bench. Afterwards the same specimens are inserted into black chamber of the measuring device and the picture of the symbol is taken.

With the calibration part of the software program, the lightness values of the selected points can be obtained from the picture and used for the calculation of both constants. The calculation is normally done by the same part of the program, so the user just need to select the points and input the previously measured luminance of these points. The user should input at least two points, but he/she can also input more points to get better values for *A* and *B*. Beside this possibility both constants can also be calculated using some other tools or software and inputted in the program manually.

To obtain better measurement result with the device, the constants need to be set for each type of the switch (symbol) separately. The constants are saved in a software configuration data and need to be set just once although we recommend the user to repeat the calibration procedure after certain time interval to compensate possible changes in camera CCD sensor.



Figure 5: Part of the software for calibration of the measurement system.

After both constants are set, the software and so also the device is ready for use.

6. Software Program

From the user's point of view the software should be simple and intuitive to use. We kept in mind that users probably will be neither computer nor lighting experts. To accomplish this graphical user interface has been developed which allows users to be able to choose functions by clicking.

As mentioned before, the software itself has two functions: measurement and calibration. Use of the software part for the calibration was already described in previous chapter.

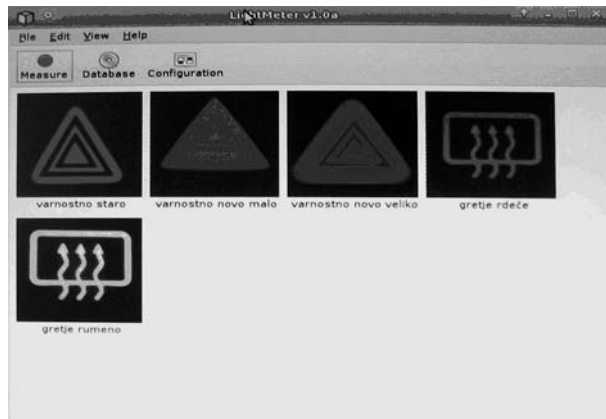


Figure 6: Main window of the software where type of measured switch is chosen.

Measurement is accomplished by selecting first the type of the sign we are about to measure with clicking on the right picture on software desktop. After clicking the "measurement" button the camera is initialized with appropriate parameters such as shutter speed, aperture and ISO sensitivity.



Figure 7: Settings which are send to camera before picture is taken.

The picture is then automatically captured, transferred to the computer and displayed in a window. In the next step the measuring points are automatically detected. To allow user to verify measuring points, they

are drawn on the displayed image. After calculation of luminance of measuring points the results are displayed in the lower part of the "Measurement preview window". On the left side of the results also a statement whether measured specimen complies with the standards or not is written together with green (complies) or red (not complies) symbol.

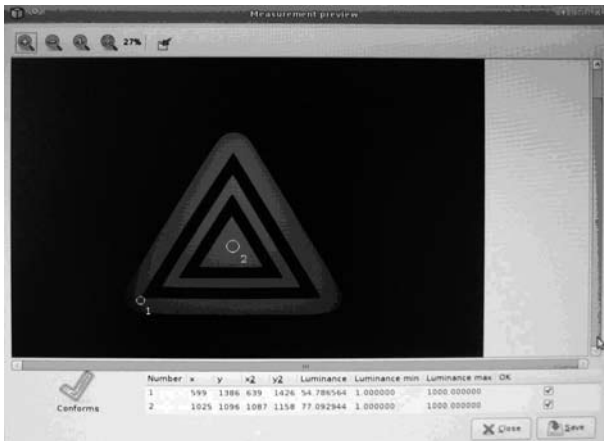


Figure 8: Measurement results, the specimen complies with the standard.

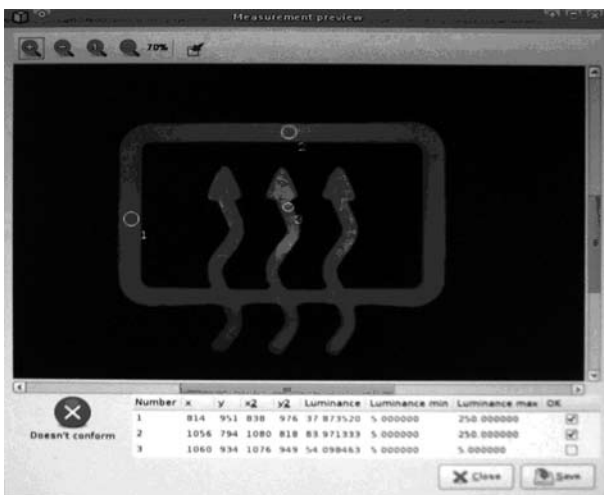


Figure 9: Measurement results of a specimen which does not comply with the standard.

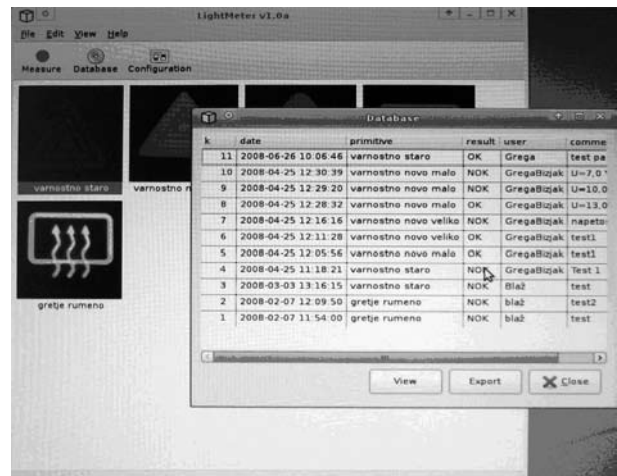


Figure 10: Database with list of last performed measurements.

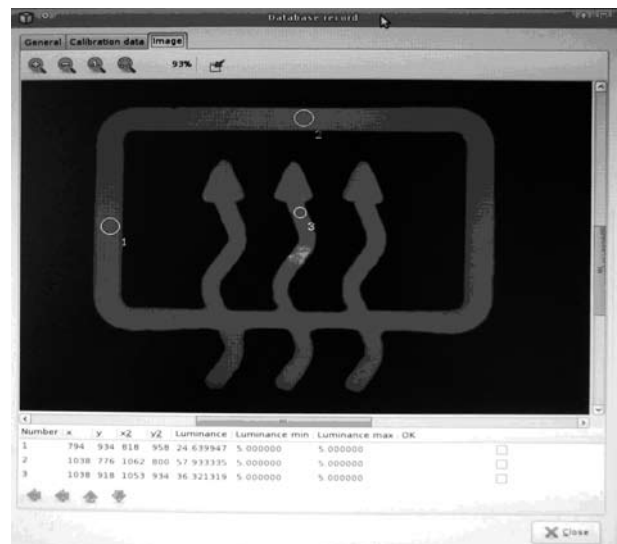


Figure 11: Results of a measurement stored in a database.

After measurement is done, the results can be saved in a database. On this point also a comment to be saved with the results can be added. Together with the results and comment also the picture and the calibration data are saved. Saved results are so documented for the quality control and can be later analyzed again if needed.

From the development point of view the software has been developed in c programming language under Linux 2.6 operating system because of a large choice of open source libraries. In order to remotely control the camera LIBPTP communication library has been used. Graphical user interface is implemented using GTK toolkit.

References

1. COUTELIER, B., Luminance calibration of the Nikon Coolpix 990 digital camera, EPIC 2002 AIVC, October 2002, pp. 697-702
2. ZAGAR, T., BIZJAK, G. Izracun svetlosti iz RGB vrednosti umerjenega digitalnega fotoaparata in razvoj aplikacije za analizo svetlosti, Faculty of electrical engineering, University of Ljubljana, Ljubljana 2004
3. LUIN, B., KOBAV, M. B., BIZJAK, G. Luminance measurement device based on digital camera for quality control in automative industry. 26th Session of the CIE: 4.-11. July 2007, Beijing, China

Arrived: 13. 09. 2011

Accepted: 26. 1. 2012

A New Design of Split Ring Resonators for Electromagnetic (EM) absorption Reduction in Human Head

*M. R. I. Faruque^{1,2} *, M. T. Islam¹ and N. Misran^{1,2}*

¹*Institute of Space Science,*

²*Department of electrical, Electronic and systems Engineering,*

*Faculty of Engineering & Built Environment, Universiti Kebangsaan Malaysia,
43600 UKM, Bangi, Selangor D. E., Malaysia*

Abstract: The reducing electromagnetic (EM) absorption reduction with a new type of triangular split ring resonators (TSSRs) based on triangular metamaterials (TMMs) attachment is investigated. The finite-difference time-domain method with lossy-Drude model is adopted in this investigation. The technique of EM absorption reduction is discussed and the effects of position, distance, and size of new design of metamaterials are investigated. Metamaterials have achieved a 63.40% reduction of the initial SAR value for the case of 10 gm SAR.

Keywords: antenna, human head model, lossy-Drude model, triangular metamaterials, specific absorption rate (SAR).

Nova oblika prekinjenih obročnih resonatorjev za zmanjševanje elektromagnetne absorpcije v človeški glavi

Izvleček: Raziskan je nov tip trikotno prekinjenih obročnih resonatorjev (TSSRs) na osnovih dodanih trikotnih meta kovinah (TMMs) za zmanjševanje elektromagnetne (EM) absorpcije. Obdelana je metoda končnih diferenc v časovnem prostoru z izgubnim Drude modelom. Predstavljena in raziskana je tehnika zmanjševanja EM absorpcije in vpliv lokacije, razmika in velikosti novih oblik meta kovin. Metamateriali so dosegli 63.40% zmanjšanje začetne vrednosti SAR indeksa v primeru 10 gm SAR

Ključne besede: antena, model človeške glave, izgubni Drude model, trikotne meta kovine, specifična absorpcijska stopnja (SAR)

*Corresponding Author's e-mail: rashedgen@yahoo.com

1. Introduction

The basic parameter in the electromagnetic (EM) absorption is defined in terms of the specific absorption rate (SAR), or the absorbed power in unit mass of tissue [1]. The SAR is generally evaluated using either phantom measurement or computer simulation. The interaction of handset antennas with the human body is a great consideration in cellular communications. The user's body, especially the head and hand, influence the antenna voltage standing wave ratio (VSWR), gain, and radiation patterns. The interaction of the cellular handset with the human head has been investigated by many published papers considering; first, the effect

of the human head on the handset antenna performance including the feed-point impedance, gain, and efficiency [2-7], and second, the impact of the antenna EM radiation on the user's head due to the absorbed power, which is measured by predicting the induced SAR in the head tissue [6-14]. In [6], a perfect electric conductor (PEC) reflector was placed between a human head and the driver of a folded loop antenna. The result showed that the radiation efficiency can be enhanced and the peak SAR value can be reduced. In [8, 15], a study on the effects of attaching conductive materials to cellular phone for SAR reduction has been presented. It is shown that the position of the shielding material is an important factor for SAR reduction effectiveness.

Metamaterials denote artificially constructed materials having electromagnetic properties not generally found in nature. Two important parameters, electric permittivity and magnetic permeability determine the response of the materials and metamaterials to electromagnetic fields. The negative permittivity can be obtained by arranging the metallic thin wires periodically [11, 13]. On the other hand, an array of split ring resonators (SRRs) can exhibit negative effective permeability. In [7], the designed SRRs operated at 1.8 GHz were used to reduce the SAR value in a lossy material. The metamaterials are designed on circuit board so it may be easily integrated to the cellular phone. Simulation of wave propagation into metamaterials was proposed in [7, 15]. The authors utilized the FDTD method with lossy-Drude models for metamaterials simulation. This method is a helpful approach to study the wave propagation characteristics of metamaterials [11] and has been more developed with the perfectly matched layer (PML) and extended to three-dimension problem [7].

Since 2000, the rate of publications on electromagnetic-metamaterials has grown exponentially [11-16], indicative of the intense interest that artificial materials have generated. Specifically, the problems to be solved in SAR reduction need a correct representation of the cellular phone, anatomical representation of the head, alignment of the phone and the head, and suitable design of metamaterials.

2. Methodology

CST MWS, based on the finite integral time-domain technique (FITD), was used as the main simulation instrument. A non-uniform meshing scheme was adopted so that the major computation endeavor was dedicated to regions along the inhomogeneous boundaries for fast and perfect analysis. For two cut planes of the complete model indicating the area with denser meshing along the inhomogeneous boundaries. The minimum and maximum mesh sizes were 0.3 mm and 1.0 mm, respectively. A total of 2,122,164 mesh cells were generated for the complete model, and the simulation time was 1208 seconds (including mesh generation) for each run on an Intel Core TM 2 Duo E 8400 3.0 GHz CPU with 4 GB RAM system. At first materials are placed between the antenna and a human head, and then replaced by a metamaterial. In order to study the SAR reduction of an antenna operated at the GSM 900 band, the effective medium parameter of metamaterials is set to be negative at 900 MHz. Different positions, sizes, and negative medium parameters of metamaterials for SAR reduction effectiveness are also analyzed. The SAM head model was considered for this research where it consists about 2,097,152 cubical cells with a

resolution of 1 mm. Fig. 1 shows a portable telephone model at 900 MHz for the present. It was considered to be a quarter wavelength PIFA antenna mounted on a rectangular conducting box. The conducting box was 10 cm tall, 4 cm wide, and 3 cm thick. The PIFA antenna was located at the top surface of the conducting box.

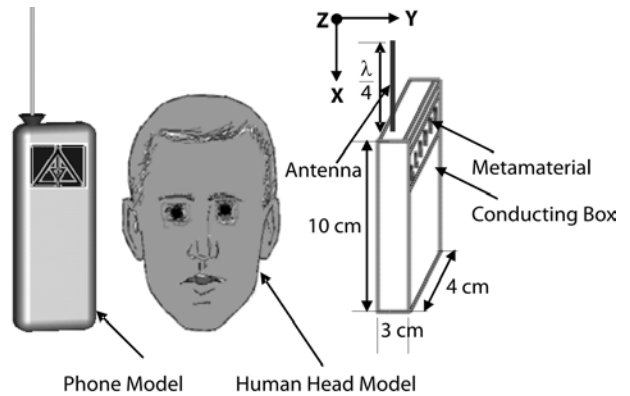


Figure 1: The head and antenna model for SAR calculation.

3. TSRRs Construction and Design

We establish that the TMMs can be used to reduce the peak SAR 1 gm and SAR 10 gm in the head from the FDTD analysis. In this section, the TMMs are operated at the 900 and 1800 MHz bands of the cellular phone were considered. The TMMs can be attained by arranging TSRRs periodically. The TSRRs structure consists of two concentric triangular ring of conductive material. There is a gap on each triangular ring, and each triangular ring is situated opposite to the gap on the other ring. The schematics of the TSRRs structure that we used in this study as shown in Fig. 2.

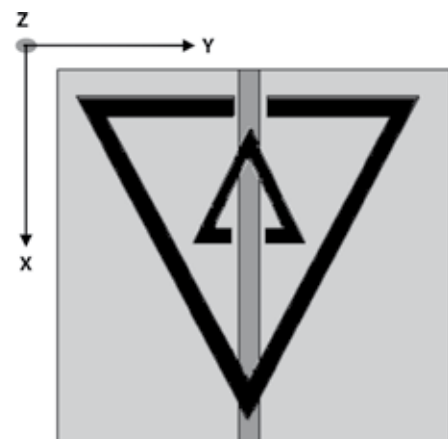


Figure 2: The structure of the TSRRs.

To construct the TMMs for SAR reduction, we proposed one model of resonators namely the TSRRs as shown in Fig. 2. We design the resonators for operation at the 900 MHz bands. The TSRRs contains two triangular rings, each with gaps appearing on the opposite sides. The SRRs was introduced by Pendry et al. in 1999 [10] and subsequently used by Smith et al. for synthesis of the first left-handed artificial medium [12]. We design the metamaterials from periodically arrangement of SRRs to reduce the SAR value. By properly designing structure parameters of TSRRs, the effective medium parameter can be negative around 900 and 1800 MHz band. In Fig. 2, the structures of resonators are defined by the following structure parameters: the triangular ring thickness c , the triangular ring gap d , the triangular ring size l , the split gap g , and c_0 is the speed of light in free space. The resonant frequency ω is very sensitive to small changes in the structure parameters of TSRRs. The frequency response can be scaled to higher or lower frequency by properly choosing these geometry parameters by utilizing the following equation [15].

$$\omega^2 = \frac{3lc_0^2}{\pi \ln \frac{2c}{d} r^3} \quad (1)$$

The TSRRs is resonating at approximately half the guided-wavelength of the resonant frequency. There are two resonances from the split rings. We have given the formula for the resonance of the outer split ring, which has a lower resonance frequency.

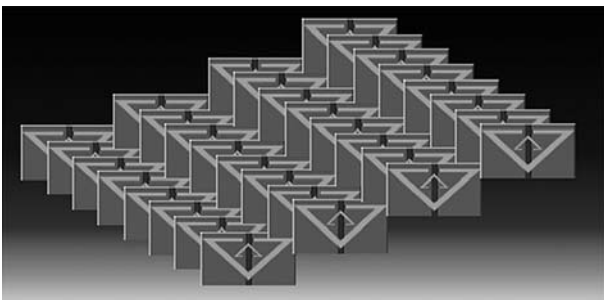


Figure 3: The structure of the TSRRs array used in this simulation.

Figure 3 shows the arrays of TSRRs based on TMMs design used in this simulation. In the new design of metamaterials we have considered 28 elements in the propagation direction which will reduce the thickness and metamaterial size. In our new design research found that metamaterial design; specifically ring size, ring thickness is an important factor for SAR reduction.

4. Results & Discussion

The designed of triangular split ring resonators (TSRRs) were placed between the antenna and a human head thus reducing the SAR value. In order to study SAR reduction of an antenna operated at the GSM 900 band, different positions, sizes, and metamaterials for SAR reduction effectiveness are also analyzed by using the FDTD method in conjunction with a detailed human head model. The antenna was arranged in parallel to the head axis, the distance is varied from 5 mm to 20 mm, and finally 20 mm was chosen for comparison with the metamaterials. Besides that, the output power of the mobile phone model needs to be set before SAR is simulated. In this paper, the output power of the cellular phone is 600 mW at the operating frequency of 900 MHz. In the real case, the output power of the mobile phone will not exceed 250 mW for normal use, while the maximum output power can reach to 1 W or 2 W when the base station is far away from the mobile station (cellular phone). The calculated peak SAR 1 gm value is 2.002 W/kg, and SAR 10 gm value is 1.293 W/kg when the phone model is placed 20 mm away from the human head model without a metamaterial. This SAR reduction is better than without metamaterials attachment, the result reported in [6], and [8], which is 2.28 W/kg and 2.17 W/kg, for SAR 1 gm. This is because the mobile antenna position, and antenna sizes is not properly situated, and antenna is different also. This SAR value is better compared with the result reported in [7], which is 2.43 W/kg for SAR 1 gm. This is achieved using different radiating powers and different antenna.

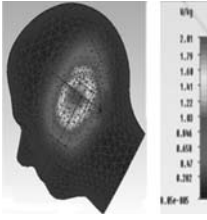
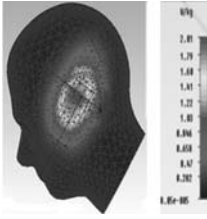
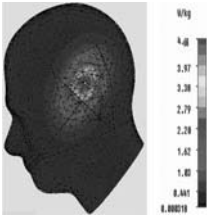
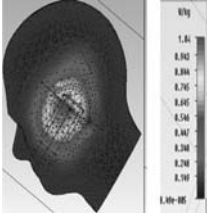
The use of metamaterials was also compared with other SAR reduction techniques. A PEC reflector and a ferrite material are commonly used in SAR reduction. The PEC reflector and ferrite sheet were analyzed. The relative permittivity and permeability of the ferrite sheet were $\epsilon = 7.0 - j0.58$ and $\mu = 2.83 - j3.25$, respectively. A PEC placed between the human head and the antenna is studied. It can be found that the peak SAR 1 gm is increased with the use of a PEC reflector. This is because the EM wave can be induced in the neighbour of a PEC reflector due to scattering. When the size of PEC sheet is small compared to the human head, the head will absorb more EM energy. Similar results of peak SAR increase with PEC placement were also reported in [7].

The use of a ferrite sheet can reduce the peak SAR 1 gm effectively. However, the degradation on radiated power from the antenna is also significant. In addition, compared to the use of a ferrite sheet, the metamaterials can be designed on the circuit board so they may be easily integrated to the cellular phone.

To study the effect of SAR reduction with the use of new type of metamaterials, the radiated power from the PIFA antenna with $\mu = 1$ and $\epsilon = -3$ mediums was fixed at 600 mW. Numerical results are shown in Table 1. It is found that calculated SAR value at 900 MHz, without the metamaterial, is 2.002 W/kg for SAR 1 gm and with the metamaterial, the reduction of the SAR 1 gm value is 1.0963 W/kg. The reduction is 45.44 % where as the design reported in [7] achieved 22.63%. This is achieved due to the consideration of different density, different antenna, and different size of metamaterial and

different type of conductivity. The SAR reduction is better than that our previous research (where we achieved about 42.12 %) [15], due to the use of new metamaterials. Furthermore, the size of the mobile phone was considered 61 mm but in our previous paper [15] it was considered 63 mm. From simulation results, the metamaterials can reduce peak SAR effectively and the antenna performance can be less affected. The metamaterials are resonant due to internal capacitance and inductance. The mediums will display a stop band with a single negative medium parameter.

Table 1: Comparisons of SAR reduction techniques with different materials

| | $Z_R (\Omega)$ | $P_R (mW)$ | Peak head SAR (W/Kg) | |
|--|----------------|------------|--|--------|
| | | | 1 gm | 10 gm |
| Without material | 63.39 + j94.53 | 600 |  | |
| | | | 2.002 | 1.673 |
| $\mu = 1, \epsilon = -3$ (Metamaterial) | 51.04 + j98.94 | 512.7 |  | |
| | | | 1.0724 | 0.8215 |
| PEC reflector | 66.83 + j32.23 | 509.3 |  | |
| | | | 4.6803 | 3.278 |
| Ferrite Sheet | 51.43 + j99.68 | 519.3 |  | |
| | | | 1.043 | 0.676 |

5. Conclusion

The EM absorption between an antenna and the human head with new type of metamaterials has been discussed in this paper. Utilizing metamaterial in the phone model a SAR value is achieved of about 0.692 W/kg for SAR 10 gm and 1.0923 W/kg for SAR 1 gm is achieved. Numerical results can provide useful information in designing communication equipment for safety compliance.

References

- 1 International Non-Ionizing Radiation Committee of the International Radiation Protection Association.: 'Guidelines on Limits on exposure to radio frequency electromagnetic fields in the frequency range from 100KHz to 300GHz'. Health Physics, 1988, 54, (1), pp. 115-123.
- 2 Islam, M. T. Faruque, M. R. I. and Misran, N.: 'Design analysis of ferrite sheet attachment for SAR reduction in human head', Progress In Electromagnetics Research, PIER, 2009, 98, pp. 191-205.
- 3 Islam, M. T. Faruque, M. R. I. and Misran, N.: 'Study of specific absorption rate (SAR) in the Human Head by metamaterial attachment', IEICE Electronics Express, 2010, 7 (4), pp. 240-246.
- 4 Faruque, M. R. I. Islam, M. T. and Misran, N.: 'Effect of human head shapes for mobile phone exposure on electromagnetic absorption', Informacije MIDEM, 2010, 40 (3), pp. 232-237.
- 5 Islam, M. T. Faruque, M. R. I. and Misran, N.: 'Specific absorption rate analysis using metal attachment', Informacije MIDEM, 2010, 40 (3), pp. 238-240.
- 6 Kuo C. M., Kuo C. W.: 'SAR distribution and temperature increase in the human head for mobile communication', in IEEE-APS Int. Symp. Dig., Columbus, OH, 2003, pp. 1025-1028.
- 7 Hawang, J. N. and chen, Fu-chiarng.: 'Reduction of the peak SAR in the Human Head with Metamaterials', IEEE Trans. on antenna and propagation. Dec. 2006, 54, (12), pp. 3763-3770.
- 8 Wang, J. and Fujiwara, O.: 'FDTD computation of temperature rise in the human head for portable telephones', IEEE Trans. Microwave Theory Tech., Aug. 1999, 47, (8), pp. 1528-1534.
- 9 Faruque, M. R. I. Islam, M. T. and Misran, N.: 'Design of Metamaterial Attachment for SAR Reduction in Human Head', Applied Computational electromagnetic society Journal (ACES Journal), December 2010, 25 (12), pp. 1097-1107.
- 10 Islam, M. T. Faruque, M. R. I. and Misran, N.: 'SAR Reduction in a Muscle Cube with Metamaterial Attachment', Applied Physics A (Springer), 2011, 103 (2), pp. 367-372.
- 11 Sigalalas, M. M. Chan, C. T. Ho, K.M. and Soukoulis.: 'Metallic photonic band gap materials', Phys. Rev. B., 2000, 52, (16), pp. 11744-11760.
- 12 Smith, D. R. R D, and Kroll, N.: 'Negative Refractive Index in left handed materials', Phys. Rev. Lett., 2000. 85, (14), pp. 2933-2936.
- 13 Faruque, M. R. I. Islam, M. T. and Misran, N.: 'Analysis of Electromagnetic Absorption in the Mobile Phones Using Metamaterials', Electromagnetics Journal (Taylor & Francis Group), 2011, 31 (3), pp.215-232.
- 14 Manapati, M. B. and Kshetrimayum, R. S. : 'SAR reduction in human head from mobile phone radiation using single negative metamaterials', J. of Electromagn. Waves and Appl., 2009, 23, pp. 1385-1395.
- 15 Islam M. T., Faruque M. R. I., Misran N. : 'Reduction of specific absorption rate (SAR) in the human head with ferrite material and metamaterial', Progress In Electromagnetics Research, PIER C, 2009, 9, pp. 47-58.
- 16 Pendry J. B., Holen A. J., Robbins D. J., Stewart W. J., 'Magnetism from conductors and enhanced non-linear phenomena', IEEE Trans. Microwave Theory Tech., Nov. 1999, 47, (11), pp. 2075–2084

Arrived: 03. 05. 2011

Accepted: 26. 1. 2012

Characterization of α -Si:H P-I-N photodiode response

Vera Gradišnik*

University of Rijeka, Faculty of Engineering, Croatia

Abstract: The α -Si:H p-i-n photodiode response due to simultaneous voltage and light pulses has a characteristic shape similar as that of retinal layers response. The characteristic shape of photodiode response, ascribed to trap states, is analyzed and discussed. The amplitude, waveform, latency and threshold voltages of the α -Si:H p-i-n photodiode responses were analyzed in dependence of voltage pulse amplitude and voltage and light pulses duration. The simultaneous stimuli influence on photodiode response has been explained through the excitation of dangling bond in i-layer. Described photodiode response behaviour suggests potential of development of a method for defect characterization and use of α -Si:H p-i-n PD as image sensor.

Keywords: α -Si:H, defects, photodiode, retina

Karakterizacija odziva α -Si:H P-I-N fotodiode

Izveček: Oblika odziva α -Si:H p-i-n fotodiode pri sovpadnih napetostnih in svetlobnih pulzih je podobna kot odzivu plasti mrežnice. Analizirana in predstavljena je tipična oblika odziva fotodiode pri različnih stanjih pasti. Amplituda, oblika signala, latenca in prag napetosti α -Si:H p-i-n fotodiode je bila analizirana v odvisnosti od amplitude napetostnega pučza in trajanja osvetlitve. Odziv fotodiode pri sočasnem vzbujanju je razložen s pomočjo vzbujanja bingljajočih vezi v plasti i. Opisan odziv fotodiode ponuja možnost razvoja metode karakterizacije defektov in uporabe α -Si:H p-i-n PD kot slikovnega senzorja.

Ključne besede: α -Si:H, defekti, fotodiode, mrežnica

*Corresponding Author's e-mail: vera.gradisnik@riteh.uniri.hr

1. Introduction

It is well known, that the presence of charged defects in the optically active material, which is intrinsic layer (i-layer) in the p-i-n, α -Si:H photodiode reduces the built-in electric field [1]-[4] and consequently the local optical absorption coefficient [5], reduces the free carriers mean lifetime, decreases the response time. The knowledge of the spatial distribution of defects induced by light is important in improving the photodiode performances in order to use it as a detector in active pixel sensor and imaging sensors. The mid-gap states energy levels and their spatial distribution in i-layer and at p⁺-i interface can be obtained [6, 7] from the transient dark current and steady-state thermal generation current. Emission of carriers from the p-i and n-i interfaces and thermal generation in i-layer, which is a voltage dependent at low biases, mainly contribute to the dark current. The optical and electronic properties of α -Si:H determine transient current relevance for device application. The recombination via dangling bonds as the main recombination centers and transport through localized states contributes to the transient current as

are well described by Fuhs [1] and Dhariwal et al. [2-4]. The influence of deeply-trapped charge on the transient photocurrent has been studied by various authors using the transient photocurrent method TPC and the AC and DC constant photocurrent method CPM [8-10].

The aim of this paper is to study the transient responses and respective time constants after the simultaneous illumination and voltage pulses as well as the influence of dangling bond states on characteristic shape of photodiode response previously observed in [11] in comparison with similar behaviour of retinal response [12]. The optimal parameters (amplitude, duration and waveform), threshold voltage and response latencies of the α -Si:H p-i-n photodiode responses on simultaneous electrical and light stimulation were analyzed and discussed.

The results show the dangling bond states energy levels distributed in range from shallow to deep and activated at low bias voltages and visible pulses illumination, are responsible for characteristic photodiode response shape. Further investigation is needed to

develop the method for colour recognition and material characterization.

After a brief description of the devices fabrication and measurements in Section II, the obtained results are presented and discussed in Section III. Finally, the conclusions are given in Section IV.

2. Device fabrication and measurements

The a-Si:H p-i-n structure was deposited on a transparent conductive oxide (TCO) coated glass from undiluted SiH_4 by plasma-enhanced CVD as described in [13]. The thicknesses of the n-type, i-type and p-type layers were 5 nm, 300 nm and 5 nm, from top to the bottom, respectively. The n-type layer was made by adding phosphine and the p-type by adding diborane to the gas mixture. The back contact was aluminium deposited by the evaporation. The area of the pixel was 0.28 cm^2 . The basic device characterization and experimental set-up are described in more details in [13] and [14]. Photo-illumination was obtained through the bottom p-type layer. The transient response of a-Si:H device was measured as a response to the simultaneous pulses of light and bias voltage.

Measurements were carried out at the room temperature. Multicolour LED lamps were used in the experiments, emitting at 470 nm, 565 nm and 624 nm for blue (B), green (G) and red (R) light, respectively. The pulse widths in our experiments (0.5 - 3 ms) are in accordance with relevant values used in measurements of other authors obtained on retina [15].

Simultaneous response on voltage and light pulse was measured on a-Si p-i-n photodiode at 2V reverse bias voltage. The voltage pulse amplitude was changed from 0.1 to 1 V at constant pulse duration for all wavelengths. For the same voltage pulse amplitude, the pulse duration T_a was changed from 0.5 to 3 ms. The concurrent forward voltage and light pulses were applied on a-Si:H p-i-n photodiode at low reverse voltages. The same response behaviour was also observed in reversed mode. The measurement set-up was previously described in detail [13].

3. Results and discussion

Fig. 1 shows the a-Si p-i-n PD responses on the simultaneous voltage and R, G, B, RGB LED light pulses. The voltage pulse amplitudes for R, G, B and RGB were 0.3, 0.1, 0.1 and 0.5 V, respectively and 0.5 ms pulse du-

ration (T_a) with period of 3 ms. As observed and described previously in [11], with increased voltage amplitudes, above threshold voltage for any wavelength, the electric field influence prevails over the optical generation. The responses (basic colours R, G, B and their superposition RGB) show two distinct shapes a) characteristic and b) standard. Standard responses are exponential in nature while characteristic responses, with quite different shapes, are exponential in smallest time intervals and show similarities with retinal signals [11].

The characteristic shape of all responses for given small voltage pulse amplitude and pulse duration is shown in Fig. 1 and Fig. 2. In first time interval the positive amplitudes (p1) is present, which are voltage dependent as described in [11]. After that, is the region of exponential fall to quasi steady-state, negative potential, NP [12, 15]. Next follows sudden fall to negative amplitude (n1) and than the second positive amplitude (p2) before long tail and after that appears wavelength dependent third (p3) positive amplitude (Fig. 1). Increasing the voltage pulse amplitude, at 0.5 ms pulse duration, the photodiode response takes spike shape as shown for blue light illumination in Fig. 2.

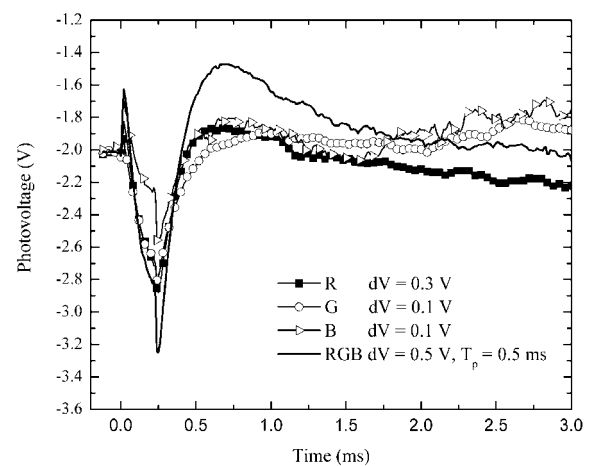


Figure 1: PD responses to simultaneous light and voltage pulses under the illumination of R, G, B and RGB LED. The voltage pulse amplitudes (dV) were 0.3, 0.1, 0.1 and 0.5V, respectively. Pulse duration (T_p) of 0.5 ms was the same in all cases.

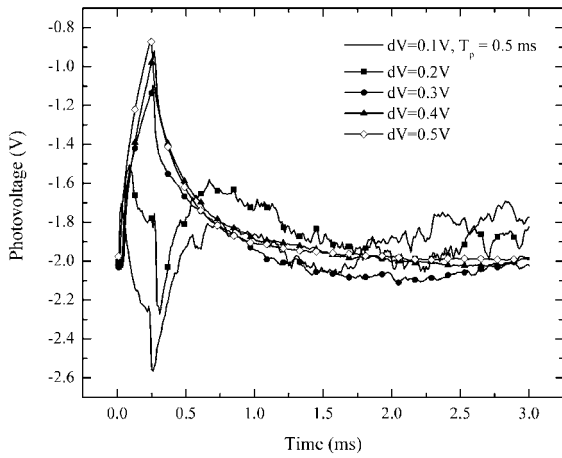
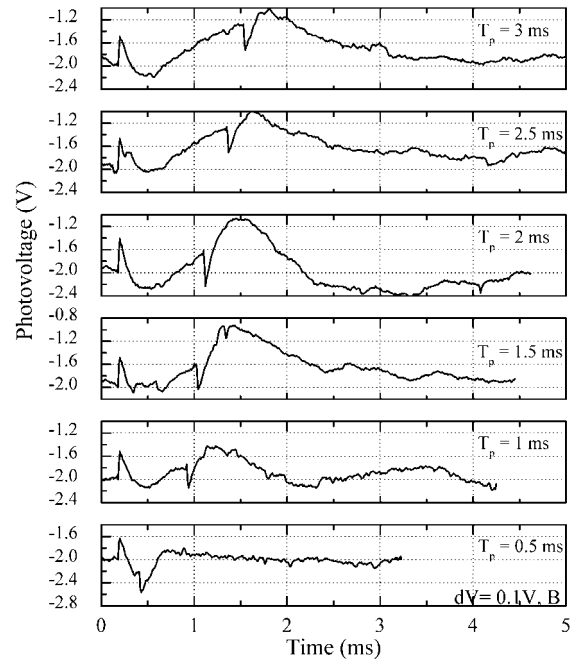
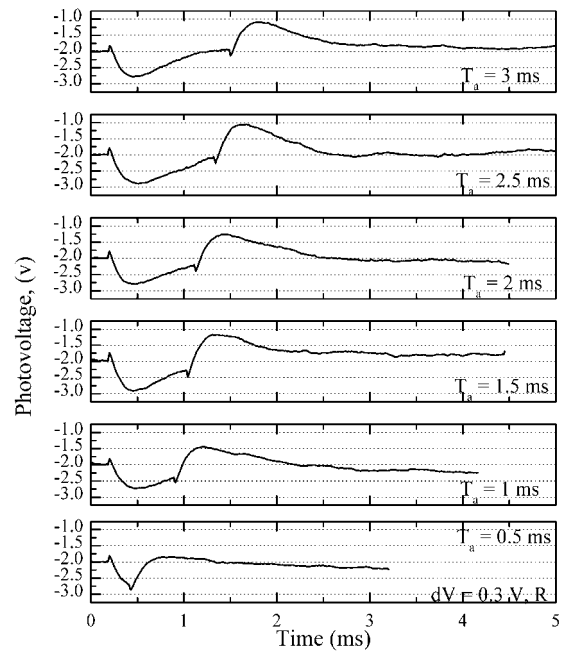


Figure 2: PD responses to simultaneous blue light and voltage pulses of 0.5 ms duration (T_p) for different voltage pulse amplitudes (dV) from 0.1 to 0.5 V.

The detailed analysis of characteristic shapes follows. The threshold voltage at which appears the characteristic photodiode response shape is 0.1 V, for blue and green light, 0.3 V and 0.5 V for red and RGB light, respectively. The peak-to-peak amplitude, defined as difference from positive (p2) and negative (n1) amplitude, is 0.76 V, 0.91V, 1.02 V, 1.73 V for blue, green, red, and RGB light, respectively and it decreases with increased voltage pulse amplitude. The positive response amplitude (p2), in relation to referent reverse bias voltage of -2 V, increases until negative amplitude (n1) and their difference decrease with voltage pulse amplitude. The difference in latency times between p2 and n1 decreases, also. The negative potentials, NP, are -2.23 V, -2.68 V, -2.69 V and -3.03 V for blue, green, red and RGB light, respectively.



a)



b)

Figure 3: PD responses to simultaneous a) blue (B) and b) red light (R), respectively and voltage pulses of 0.1 V and 0.3 V voltage amplitude (dV), respectively and different pulse durations (T_p) from 0.5 to 3 ms.

As shown in the Figure 2, and in the Figure 3 a) and b), the shape of responses changes with voltage pulse amplitude and with pulse duration, respectively.

In order to determine the influence of photo-generated carriers on pulse response, pulse durations were varied from 0.5 to 3 ms with period of 5 ms. Fig. 3.a) shows the a-Si:H p-i-n responses to blue light and voltage pulses from 0.5 to 3 ms duration, with a voltage pulse amplitude of 0.1 V. Fig. 3 b) response to red light and voltage pulse amplitude of 0.3 V.

In examining of the photodiode response as a function of pulse duration, it is evident that the all responses show characteristic shape primarily composed of n1 and p2 peaks. However, at pulse duration over 0.5 ms, there is a large secondary minimum, n0, evident in response as overshoot.

The corresponding n1- and p2- peaks delay times called "latency", signed as α and β , respectively, are measured from the pulses onset and are shown in Fig. 4 for blue light illumination. The negative peak amplitude, n1, firstly decreases with increased pulse duration from 0.5 to 1 ms and remains quasi constant with further pulse duration increase, as shown in Fig. 4. However, the positive peak amplitude, p2, shows increase. The peaks amplitude difference ($p2 - n1$), increases for small and decreases for higher pulse durations. Delay times, known as latency, for both peaks n1 and p2 increase for same conditions. The observed negative n0 amplitude shows small changes with pulse duration increase, Fig. 4.

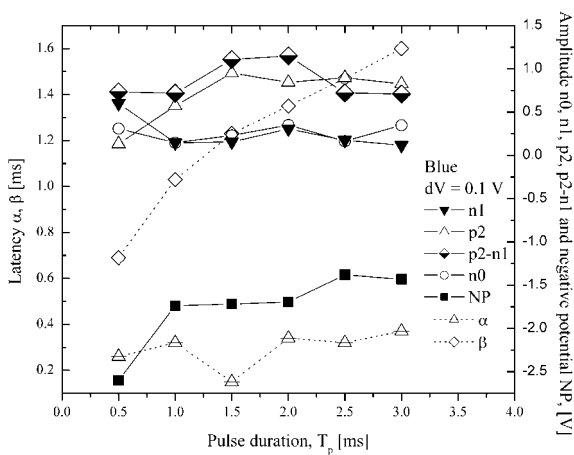


Figure 4: Amplitudes n0, n1, p2, p2-n1, negative potential NP, and latency α , β of n1 and p2 peaks of PD responses to simultaneous voltage and blue light pulses respectively as a function of pulse duration, $T_a = 0.5 \div 3$ ms.

The characteristic response shape is ascribed to dangling bonds and their effect on transient response of p-i-n a-Si:H photodiode at simultaneously forward voltage and light pulse of visible light at low reverse bias and low frequency as presented and discussed in [11]. The calculated activation energies of dangling bond

levels, as described in [14] using methods from [8-9], [16] and neglecting the Poole-Frenkel effect, for red, green, blue and red-green-blue light within time intervals in which the photodiode response is exponential in nature, are shown in Fig. 5.

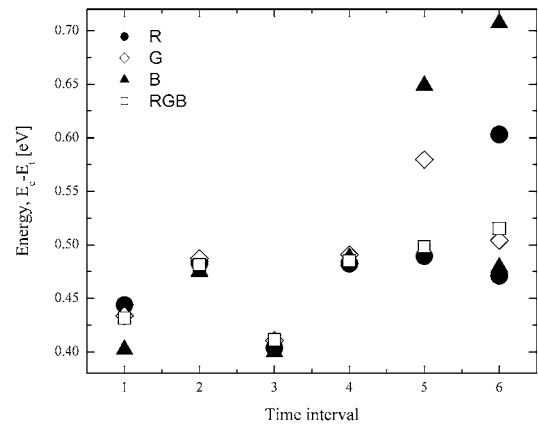


Figure 5: Calculated trap energy levels for PD responses to simultaneous voltage and red, green, blue and red-green-blue light pulses presented in Fig. 1, respectively. The time intervals corresponds to one in which the changes in response shapes occurs and are exponential in nature.

Analysing the measured PD responses it is observed that at small voltage pulse amplitude, less than 0.5 V, in initial time interval, when voltage and light pulses suddenly go on, the voltage (electric field) influence prevails the illumination one. Dangling bond and tail states at energies between 0.4 and 0.45 eV for R, G, B and RGB light illumination, capture the photogenerated free carriers in very short initial time interval. The space charge region reduces and with decreasing electric field, reduces the current. In the second time interval, the exponential rise of photocurrent is present for low voltage pulse amplitude and for all light illuminations used in our experiment. The capture of electrons through the dangling bond at energies below 0.5 eV at p⁺-i interface follows the electric field reduction, and consequently the photocurrent reaches the local maximum, or photovoltage corresponding to negative potential, NP. In following time interval present only at pulse durations over 0.5 ms the photocurrent and space charge reduce as recombination takes place through the deeper dangling bonds. For small pulse duration, these photocurrent decreases are not evident. With increased pulse duration, photocurrent increase as an overshoot is present. In the very short next time interval, after the voltage and light pulses are turned off, the current suddenly increases as a consequence of electric field increase, occurs thermal electron emission from shallow states

about 0.4 eV and recombination of remaining photo-generated free carriers is negligible. After that follows the long current fall, overshoot, as the consequence of free carriers electrons and holes capture via the deeper states at energies around 0.5 eV. In the last time interval, a long current tail arises from detrapping of carriers from the deep level between 0.5 and 0.7 eV, before steady state. The two energy levels are activated for blue and red light illumination at the end of the tail.

The calculated activation energies of dangling bonds from PD responses (Fig. 2) to simultaneous blue light and voltage pulses with duration (T_p) of 0.5 ms for voltage pulse amplitudes from 0.1 to 0.5 V are shown in Fig. 6. Increasing the voltage pulse amplitude, results in activation of deeper energy levels. At 0.4 V, the two energy levels are involved in response.

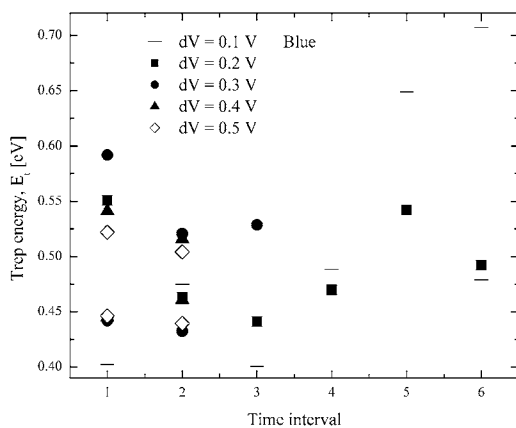


Figure 6: The calculated trap energy levels of PD responses to simultaneous blue light and voltage pulses of 0.5 ms duration (T_p) for voltage pulse amplitude (dV) from 0.1 to 0.5 V.

4. Conclusion

The characteristic shape of a-Si:H p-i-n photodiode response to simultaneous voltage and light pulses at low bias voltages are ascribed to activation of the dangling bond states energy levels. The parameters (amplitude, duration and waveform), threshold voltage and latency of PD response on simultaneous voltage and light pulses are analysed in dependence of voltage pulse amplitude or applied electric field and on duration of excitation pulses. Further investigation is necessary in order to obtain the parameters value for desirable characteristic response shape and to develop new colour recognition sensors and method for semiconductor material characterization.

References

- 1 W.Fuhs, Recombination and transport through localized states in hydrogenated amorphous and microcrystalline silicon, *J. Non-Cryst. Solids*, no. 354, 2008, pp. 2067-2078.
- 2 S.R. Dhariwal, S.Rajvanshi, Theory of amorphous silicon solar cell (a): numerical analysis, *Sol. Energy Mater. Sol. Cells*, no. 79, 2003, pp. 199-213.
- 3 S.R. Dhariwal, S.Rajvanshi, Theory of amorphous silicon solar cell (b): a five layer analytical model, *Sol. Energy Mater. Sol. Cells*, no. 79, 2003, pp. 215-233.
- 4 S.R. Dhariwal, M. Smirty, On the sensitivity of open-circuit voltage and fill factor on dangling bond density and Fermi level position in amorphous silicon p-i-n solar cell, *Sol. Energy Mater. Sol. Cells*, no. 90, 2006, pp. 1254-1272.
- 5 E. A. Schiff, H. T. Grahn, R. I. Devlen, J. Tauc, S. Guha, "Picosecond Photocurrent Transport in Hydrogenated Amorphous-Silicon p-i-n Diodes," *IEEE Trans. Electron Devices*, vol. ED-36, pp 2781-2784, Dec. 1989.
- 6 R.V.R. Murthy, V. Dutta, Underlying reverse current mechanisms in a-Si:H p+i-n+ solar cell and compact SPICE modeling, *J. Non-Cryst. Solids*, no. 354, 2008, pp. 3780-3784.
- 7 S.A. Mahmood, M. Z. Kabir, Modling of transient and steady-state dark current in amorphous silicon p-i-n photodiodes, *Current Appl. Phys.*, no. 9, 2009, pp. 1393-1396.
- 8 C. Main, Interpretation of photocurrent transients in amorphous semiconductors, *J. of Non-Crystalline Solids*, 299-302, 2002, 525-530.
- 9 C. Main, S. Reynolds, I. Zrinščak, A. Merazga, Comparison of AC and DC constant photocurrent methods for determination of defect densities, *J. of Non-Crystalline Solids*, 338-340, 2004, 228-231
- 10 A. G. Kazanskii, K. Yu Khabarova, E. I. Terukov, Modulated photoconductivity method for investigation of band gap states distribution in silicon-based thin films, *J. Non-Cryst. Solids*, no. 352, 2006, pp. 1176-1179.
- 11 V. Gradišnik, Observed similar behaviour of a-Si:H p-i-n photodiode and retina response, In Proc. of the 7th IASTED International Conf. on Biomedical Engineering, BioMed 2010, Innsbruck, Austria: IASTED, 2010, pp. 176-180.
- 12 S. G. Rosolen, F. Rifaudiere, J.-F. Le Gargasson, M. G. Brigell, Recommendations for a toxicological screening ERG procedure in laboratory animals, *Doc. Ophthalmol.*, 110(1), Oct. 2005, 57-66.
- 13 V. Gradišnik, M. Pavlović, B. Pivac, and I. Zulim, Study of the color detection of a-Si:H by transient response in the visible range, *IEEE Trans. Electron Devices*, 49(4), 2002, 550-556.

- 14 V. Gradišnik, M. Pavlović, B. Pivac, and I. Zulim, Transient response times of a-Si:H p-i-n color detector, *IEEE Trans. Electron Devices*, 53(10), 2006, 2485-2491.
- 15 T. M. O'Hearn, S. R. Sadda, J. D. Weiland, M. Maia, E. Margalit, and M. S. Humayun, Electrical stimulation in normal and retinal degeneration (rd1) isolated mouse retina, *Vision Research*, 46(19), 2006, 3198-3204.
- 16 A. Merazga, H. Belgacem, C. Main, S. Reynolds, Transient photoconductivity, density of tail states and doping effect in amorphous silicon, *Solid State Communications*, 112, 1999, 535-539.

Arrived: 14. 03. 2011

Accepted: 26. 1. 2012

An Adaptive-Parity Error-Resilient LZ'77 Compression Algorithm

Tomaž Korošec* and Sašo Tomažič

University of Ljubljana, Faculty of Electrical Engineering, Ljubljana, Slovenia

Abstract: The paper proposes an improved error-resilient Lempel-Ziv'77 (LZ'77) algorithm employing an adaptive amount of parity bits for error protection. It is a modified version of error resilient algorithm LZRS'77, proposed recently, which uses a constant amount of parity over all of the encoded blocks of data. The constant amount of parity is bounded by the lowest-redundancy part of the encoded string, whereas the adaptive parity more efficiently utilizes the available redundancy of the encoded string, and can be on average much higher. The proposed algorithm thus provides better error protection of encoded data. The performance of both algorithms was measured. The comparison showed a noticeable improvement by use of adaptive parity. The proposed algorithm is capable of correcting up to a few times as many errors as the original algorithm, while the compression performance remains practically unchanged.

Key words: Lempel-Ziv'77 coding, joint source-channel coding, multiple matches, error resilience, adaptive parity, Reed-Solomon coding

Na napake odporen zgoščevalni algoritem LZ'77 s prilagodljivo pariteto

Izveček: V prispevku je predlagan izboljššan na napake odporen Lempel-Ziv'77 (LZ'77) algoritem, ki za zaščito proti napakam uporablja prilagodljivo število paritetnih bitov prek posameznih kodiranih podatkovnih blokov. Gre za modifikacijo na napake odpornega algoritma LZRS'77, ki za zaščito posameznih podatkovnih blokov uporablja konstantno število paritetnih bitov prek celotnega kodiranega podatkovnega niza. Za zapis paritetnih bitov je izkoriščena redundanca zakodiranih podatkov. Maksimalno konstantno količino paritetnih bitov tako narekuje del niza z najnižjo redundanco, medtem ko prilagodljiva pariteta bolje izkorišča redundanco, ki je na voljo v posameznih delih kodiranega niza in je lahko tako v povprečju bistveno večja. Predlagan algoritem posledično omogoča boljšo zaščito proti napakam.

Meritve zmogljivosti obeh algoritmov so pokazale znatno povečanje odpornosti na napake pri uporabi novo predlaganega algoritma. Slednji je sposoben popraviti do nekaj krat več napak kot obstoječi algoritem, pri čemer kvaliteta zgoščevanja ostane praktično nespremenjena.

Ključne besede: Lempel-Ziv'77 kodiranje, združeno izvorno-kanalsko, večkratno ujemanje niza, odpornost na napake, prilagodljiva pariteta, Reed-Solomon kodiranje

* Corresponding Author's e-mail: tomaz.korosec@fe.uni-lj.si

1. Introduction

Lossless data compression algorithms, such as the Lempel-Ziv'77 (LZ'77) [1] algorithm and its variations, are nowadays quite common in different applications and compression schemes (GZIP, GIF, etc.). However, one of their major disadvantages is their lack of resistance to errors. In practice, even a single error can propagate and cause a large amount of errors in the decoding process. One possible solution for this problem is to use a channel coding scheme succeeding the source coding, which adds additional parity bits, allowing error correction and detection in the decoding process. However,

such a solution is undesirable in bandwidth- or storage-limited systems, where the amount of bits required to carry some information should be as small as possible. A separate use of source and channel coding is not optimal, since it does not utilize inherent redundancy left by the source coding. This redundancy could be exploited for protection against errors. Therefore, joint source-channel coding seems to be a better solution. Several joint source-channel coding algorithms have been proposed in the past, e.g., [2], [3], and [4]. The redundancy left in LZ'77 and LZW encoded data and the possibility of using it to embed additional information has been considered and investigated in [5], [6], [7], and [8].

The LZRS'77 algorithm, proposed in [8], exploits the redundancy left by the LZ'77 encoder to embed parity bits of the Reed-Solomon (RS) code. Embedded parity bits allow detection and correction of errors with practically no degradation of the compression performance. However, due to the limited redundancy left in the encoded data, the ability to detect and correct errors is limited to a finite number of successfully corrected errors. To successfully correct e error bits, $2e$ parity bits should be embedded. In the above-mentioned scheme, the number of parity bits embedded in each encoded block is constant and equal for all blocks, thus e is limited by the block with the lowest redundancy.

In this paper, we propose an improvement to LZRS'77. Instead of keeping e constant, we change it adaptively in accordance with the redundancy present in the encoded blocks. In this way, we increase the average number of parity bits per block and thus also increase the total number of errors that can be successfully corrected. We named this new algorithm LZRSa'77, where 'a' stands for adaptive.

The paper is organized as follows. In Section 2, we briefly describe the LZRS'77 algorithm, which is the basis of the proposed adaptive-parity algorithm LZRSa'77 described in Section 3. Experimental results comparing both algorithms are presented in Section 4. Some concluding remarks are given in Section 5.

2. Protection Against Errors Exploiting LZ'77 Redundancy

The basic principle of the LZ'77 algorithm is to replace sequences of symbols that occur repeatedly in the encoding string $\mathbf{X} = (X_1, X_2, X_3, \dots)$ with pointers $\mathbf{Y} = (Y_1, Y_2, Y_3, \dots)$ to previous occurrence of the same sequence. The algorithm looks in the sequence of past symbols $\mathbf{E} = (X_1, X_2, \dots, X_{i-1})$ to find the longest match of the prefix $(X_i, X_{i+1}, \dots, X_{i+l-1})$ of the currently encoding string $\mathbf{S} = (X_i, X_{i+1}, \dots, X_N)$. The pointer is written as a triple $Y_k = (p_k, l_k, s_k)$, where p_k is the position (i.e., starting index) of the longest match relative to the current index i , l_k is the length of the longest match, and $s_k = X_{i+l}$ is the first non-matching symbol following the matching sequence. The symbol s_k is needed to proceed in cases when there is no match for the current symbol. An example of encoding the sequence at position i that matches the sequence at position j is shown in Fig. 1.

To avoid overly large values of position and length parameters, the LZ'77 algorithm employs a principle called the sliding window. The algorithm looks for the longest matches only in data within the fixed-size window.

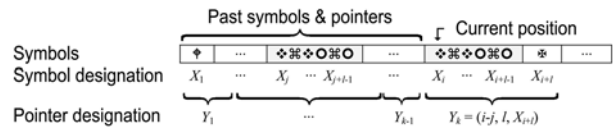


Figure 1: An example of a pointer record for a repeated part of a string in the LZ'77 algorithm. The sequence of length $l = 6$ at position j is repeated at position i , i.e., the current position.

Often, there is more than one longest match for a given sequence or phrase, which means more than one possible pointer. Usually, the algorithm chooses the latest pointer, i.e., the one with the smallest position value. However, selection of another pointer would not affect the decompression process. Actually, the multiplicity of matches represents some kind of redundancy and could be exploited for embedding additional information bits almost without degradation in the compression rate. A small decrease in compression performance could be noticed only in case when pointers are additionally Huffman encoded, as for example in GZIP algorithm, specified in [9]. With appropriate selection of one among M possible pointers, we can encode up to $d = \lfloor \log_2 M \rfloor$ additional bits. These additional bits can be encoded with proper selection of pointers with multiplicity $M > 1$, as shown in Fig. 2. The algorithm LZS'77 that exploits the above-described principle in LZ'77 scheme was proposed and fully described in [5], [6], [7], and [8]. Since different pointer selection does not affect the decoding process, the proposed algorithm is completely backward compatible with the LZ'77 decoder.

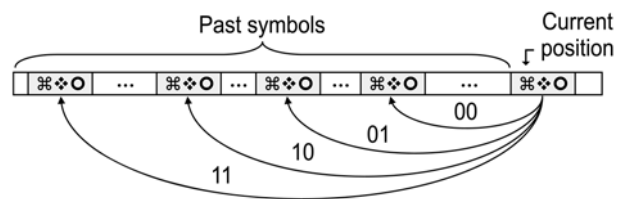


Figure 2: An example of the longest match with multiplicity $M = 4$. With a choice of one of four possible pointers, we can encode two additional bits.

The additional bits can be utilized to embed parity bits for error detection and correction. In [6] and [8], a new algorithm called LZRS'77 was proposed. It uses the additional bits in LZ'77 to embed parity bits of RS code originally proposed in [10]. In LZRS'77, an input string \mathbf{X} is first encoded using the standard LZ'77 algorithm. Encoded data \mathbf{Y} are then split into blocks of $255 - 2e$ bytes, which are processed in reverse order starting with the last block. When processing block B_n , $2e$ parity bytes of block B_{n+1} are computed first using RS(255, $255 - 2e$) code and then those bytes are embedded in the point-

ers of block B_n using the previously mentioned LZS'77 scheme. Parity bits of the first block can be stored at the beginning of the file if we also wish to protect the first block. Otherwise, to assure backward compatibility with the LZ'77 decoder, protection of the first block should be omitted.

In the decoding process, the procedure is performed in the opposite order. The first block is corrected (only in the case when the first block is protected as well) using parity bits appended at the beginning of the file. Then it is decompressed using the LZS'77 decompression algorithm, which reconstructs the first part of the original string and also recovers parity bits of the second block. The algorithm then corrects and decompresses the second block and continues in this manner till the end of the file.

The desired maximum number of errors e to be effectively corrected in each block during the decoding process is given as an input parameter of the algorithm. This number is upward-limited by the ability to embed bits in the pointer selection, i.e., by the redundancy of the encoded data. In the LZRS'77 algorithm, e is constant over all blocks; thus its value is limited by the block with the lowest redundancy. So e could be an arbitrary value between zero and maximum allowable one.

3. The LZRSa'77 Algorithm with Adaptive Parity

A constant e over all encoding blocks, as in LZRS'77, is not optimal, since redundancy in different parts of data string can differ significantly. If there is just one part of the string that has very low redundancy, it will dictate the maximum value of e for the whole string. Such low-redundancy blocks are usually at the beginning of the encoded data, since there are not yet many previous matches that would contribute to redundancy. Better utilization of overall redundancy would be possible with an adaptive e , changing from one block to another according to availability of redundancy bits in each block. In that case, low-redundancy parts of the string would affect the error protection performance just of these parts, whereas the rest of the string could be better protected according to its redundancy availability. As a result, the value of e is still upward-limited by the overall redundancy but its average value can be higher, resulting in better resistance to errors.

On the basis of the above-described assumptions, we propose an improved version of the LZRS'77 algorithm, named LZRSa'77, where 'a' refers to adaptive e . The input string X is first encoded using the standard LZ'77

algorithm, when the multiplicity M_k of each pointer is also recorded. The encoded data is then divided into blocks of different lengths, according to the locally available redundancy. Firstly, $255-2e_1$ bytes are put in the first block B_1 , where e_1 is given as an input parameter of the algorithm. Then, the number of parity bytes $2e_2$ of the second block B_2 is calculated, where e_2 is given as:

$$e_2 = \left\lfloor \frac{\sum_{k \in B_1} \lfloor \log_2 M_k \rfloor / 16}{2} \right\rfloor \quad (1)$$

If, for example, the number of additional bits that could be embedded in the pointers multiplicity of the first block ($\sum \lfloor \log_2 M_i \rfloor$) is 43, then the number of parity bytes of the second block would be $2e_2 = 2 \lfloor 43/16 \rfloor = 4$. Number '16' provides for proper bits-to-bytes recalculation, since the algorithm operate with the integer value of bytes as the RS coding does. According to the obtained value, the second block length is $255-2e_2 = 251$ bytes. The process is then repeated until the end of the input data is reached. We obtain b blocks of different lengths $255-2e_n$.

After dividing all the data into blocks of different lengths, the process of RS coding and embedding of parity bits is performed. Embedding of parity bits is realized by adjusting the pointer values. The blocks are processed in reverse order, from the very last to the first, as with the LZRS'77 algorithm. The number of parity bytes $2e_n$ for RS coding varies for each block. The sequence of operations of the encoder is illustrated in Fig. 3.

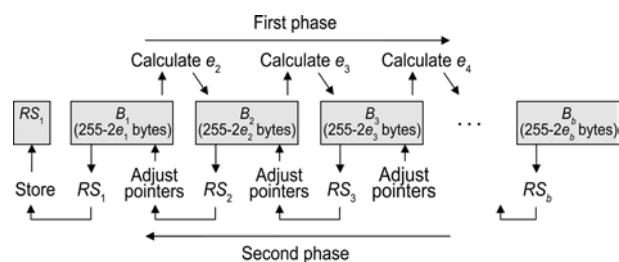


Figure 3: The sequence of operations on the compressed data as processed by the LZRSa'77 encoder. Here RS_n are parity bytes of the block B_n .

As mentioned above, the desired error correction capability of the first block e_1 is given as an input parameter of the algorithm, whereas e_n for all the other blocks are obtained from the redundancy of their preceding blocks and are as high as the redundancy permits. As in the LZRS'77 algorithm, parity bits of the first block are appended at the beginning of the encoded data, or omitted if we want to preserve backward compatibility

with the standard LZ'77 decoder. In the last case, e_1 is equal to zero.

The decoding process is similar to that used in the LZRS'77 decoding algorithm. Each block B_n is first error-corrected using $2e_n$ parity bytes known from the previous block B_{n-1} , then decoded using the LZS'77 decoder to decompress part of the original string and obtain $2e_{n+1}$ parity bytes of the next block. The amount of parity bits is used to determine the length of the next block B_{n+1} , whereas the parity bits themselves are used to correct the block. The process is continued to the last block. A high-level description of the encoding and decoding algorithms is shown in Fig. 4.

```

LZRSA'77_ENCODER (X,  $e_1$ )
let  $b, j \leftarrow 1, 0$ 
 $[P, p] \leftarrow$  LZ'77_COMPRESS(X)
while  $j < |P|$  do
  append  $(j + 1) \dots (j + 255 - 2e_b)$  bytes of  $P$  to  $B_b$ 
  let  $j \leftarrow j + 255 - 2e_b$ 
  let  $b \leftarrow b + 1$ 
  evaluate  $e_b$  by counting possible pointers in  $p$  for  $B_{b-1}$ 
for  $n \leftarrow b, \dots, 2$  do
  let  $RS_n \leftarrow$  RS_ENCODER( $B_n, e_n$ )
  embed bytes  $RS_n$  in the block  $B_{n-1}$  using LZS'77
let  $RS_1 \leftarrow$  RS_ENCODER( $B_1, e_1$ )
let  $B \leftarrow (B_1, B_2, \dots, B_b)$ 
return  $e_1, RS_1, B$ 

LZRSA'77_DECODER ( $e_1, RS_1, B$ )
 $D \leftarrow$  empty string
let  $B_1 \leftarrow$  first  $255 - 2e_1$  bytes of  $B$ 
let  $j \leftarrow 255 - 2e_1 + 1$ 
let  $n \leftarrow 2$ 
if RS_DECODER( $B_1 + RS_1, e_1$ ) = errors
  then correct  $B_1$ 
append LZ'77_DECOMPRESS( $B_1$ ) to  $D$ 
while  $j < |B|$  do
  recover  $RS_n$  from the pointers in  $B_{n-1}$  using LZS'77
  let  $e_n \leftarrow$  half a number of  $RS_n$  bytes
  let  $B_n \leftarrow$  next  $255 - 2e_n$  bytes of  $B$  from index  $j$  on
  let  $j \leftarrow j + 255 - 2e_n$ 
  let  $n \leftarrow n + 1$ 
  if RS_DECODER( $B_n + RS_n, e_n$ ) = errors
    then correct  $B_n$ 
  append LZ'77_DECOMPRESS( $B_n$ ) to  $D$ 
return  $D$ 

```

Figure 4: The error-resilient LZ'77 algorithm with adaptive parity $2e_n$. Here X is the input string, e_1 is the maximum number of errors that can be corrected in the first block, P is the LZ'77 encoded string of pointers, p is a vector of possible positions for each pointer, B_n are blocks of encoded data of variable length $255 - 2e_n$, RS_n are RS parity bytes of the block B_n , and D is the recovered string.

4. Experimental Results

To evaluate the performance of the proposed algorithm, we performed several tests with different files from the Calgary corpus [11], a commonly used collection of text and binary data files for comparing data compression algorithms. We implemented our proposed algorithm in the Matlab 6.5.1 Release 13 program tool. For the basic LZ'77 encoding, the LZ'77 algorithm with a sliding-window length of 32 kilobytes was used. It was implemented in Matlab as well. Maximum length of pointers was chosen to be 255 bytes.

In the experiment, we first compared the maximal value of constant e (e_{\max}) and average value of an adaptive e ($E(e_n)$) in different test strings. For this purpose, we encoded different files from the Calgary corpus using the LZRS'77 and LZRSa'77 algorithms. For maximal constant e observation, we performed tests only on strings of 10.000 bytes length, since the lowest-redundancy parts proved to be in the first blocks of the encoded strings, because there are not so many past symbols yet. Thus, different string lengths practically do not affect the maximal e , as long as the beginning of the string is the same. For this reason, we rather performed tests on different substrings of the same length within each file, starting at different positions. Average maximal e ($E(e_{\max})$) averaged over all tested substrings for each file is given in the second column of Table 1, whereas maximal e of the first substring of each file (and thus that corresponding to the whole file) is given in the third column. Even if, in an unexpected case, the lowest redundancy part of the whole file is not within the first 10.000 symbols, the obtained results were still relevant, since we made additional experiments on error-correction performance on the first 3000 and 30.000 symbols with the same constant parity used.

When observing average adaptive e ($E(e_n)$), we performed measurements on two different lengths of source strings, i.e., 3000 bytes and 30.000 bytes, and we again performed the tests on different substrings within each file for both lengths. The value of e_1 was in all cases chosen to be equal to 1. Results are shown in fourth and fifth columns of Table 1.

The experiment results showed that the maximal constant e that could be embedded in the redundancy of the encoded string is in the best case equal to 3 (*geo* file), whereas average adaptive e over large number of blocks could be from 4,5 up to 8. These results already justify the use of adaptive e . To justify it further, we performed another experiment. We tested the ability of each algorithm to correct random errors.

Table 1: Values of maximal constant and average adaptive e for different length (L) substrings of the Calgary corpus files

| file name | constant e | | adaptive e | |
|---------------|---|------------------------------|--|--|
| | $E(e_{\max})$ over substrings with $L=10.000$ | e_{\max} of the whole file | $E[e_n]$ over substrings with $L=3000$ | $E[e_n]$ over substrings with $L=30.000$ |
| <i>bib</i> | 2,00 | 2 | 4,79 | 5,29 |
| <i>book1</i> | 2,38 | 2 | 4,75 | 4,94 |
| <i>book2</i> | 2,18 | 1 | 4,64 | 5,04 |
| <i>geo</i> | 2,40 | 3 | 5,48 | 8,32 |
| <i>news</i> | 1,92 | 1 | 5,05 | 5,93 |
| <i>obj1</i> | 2,50 | 2 | 5,05 | / |
| <i>obj2</i> | 1,46 | 1 | 4,68 | 6,77 |
| <i>paper1</i> | 2,00 | 1 | 4,64 | 5,14 |
| <i>paper2</i> | 1,88 | 1 | 4,65 | 4,80 |
| <i>paper3</i> | 1,75 | 1 | 4,62 | 4,87 |
| <i>paper4</i> | 1,00 | 1 | 4,70 | / |
| <i>paper5</i> | 1,00 | 1 | 4,75 | / |
| <i>paper6</i> | 1,67 | 1 | 4,81 | 5,14 |
| <i>progc</i> | 2,00 | 2 | 4,65 | 5,70 |
| <i>progl</i> | 2,00 | 2 | 4,48 | 6,21 |
| <i>progp</i> | 2,25 | 2 | 4,96 | 5,69 |
| <i>trans</i> | 1,22 | 2 | 4,82 | 6,26 |

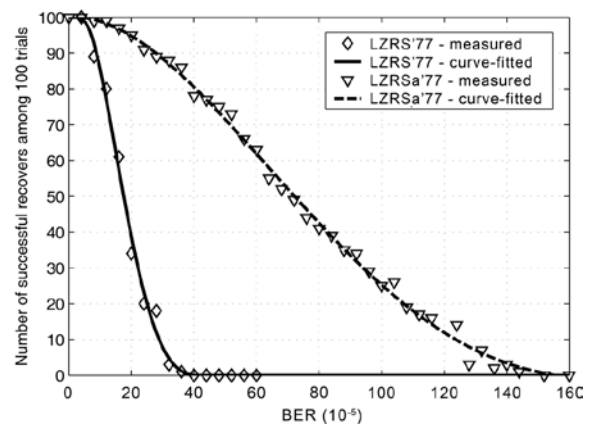
When testing error correction performance, we performed measurements on three different files from Calgary corpus, i.e., *news*, *progp*, and *geo*, which allow maximal values of constant e equal to 1, 2, and 3 respectively, as shown in Table 1. Measurements were made on the first 3000 and 30.000 bytes of each file respectively. When using the LZRSa'77 algorithm, e_1 could be an arbitrary value. However, we chose values that approximately correspond to $E(e_n)$ for each of the tested files. Thus, we chose $e_1 = 5$ for the *news* and *progp* test strings, and $e_1 = 8$ for the *geo* test string.

We tested the resilience to errors by introducing different number of errors randomly distributed over the whole encoded string. For error generation, we used a built-in Matlab function, called *randerr*, which generates patterns of geometrically distributed bit errors.

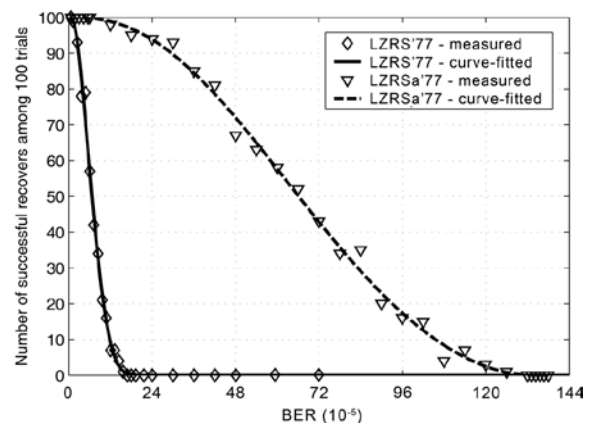
Results for the three test strings, all in two different length variations, and for both described algorithms used (LZRS'77 and LZRSa'77) are shown in the graphs in Fig. 5 to Fig. 7. Each case of string type, string length and algorithm used was tested with different numbers of injected errors. For each number of errors, 100 trials with different randomly distributed errors were performed and number of successful data recovers tested.

In the graphs in Fig.5 to Fig.7, the measured results are plotted with discrete points, whereas continuous curves represent a polynomial-fitted approximation. The results show quite an improvement in error correction capability when using the LZRSa'77 algorithm instead of LZRS'77, which is a direct consequence of the larger amount of parity used in the first algorithm. The performance improvement decreases with increasing constant e from 1 to 3, but is still noticeable also in the last case, which is practically the best we could achieve with the LZRS'77 algorithm. As can be seen from the results, the performance improvement also somewhat increases with increasing length of the string. This is probably due to the increasing $E(e_n)$ with increasing length of the string, as evident from Table 1, whereas constant e remains the same.

The performance of the LZRSa'77 algorithm could be slightly further improved using higher value of e_1 , which would, however, improve only the protection of the first block.

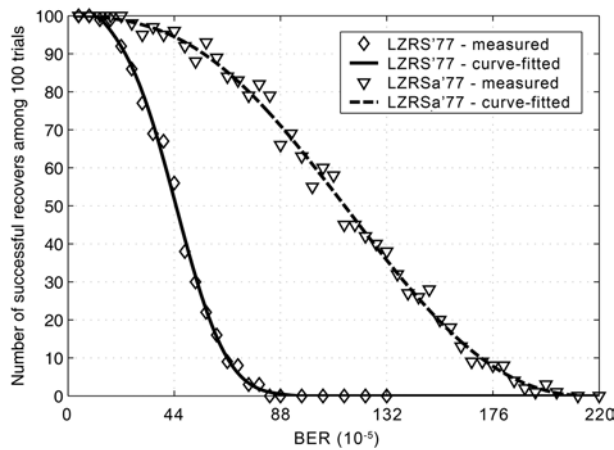


a)

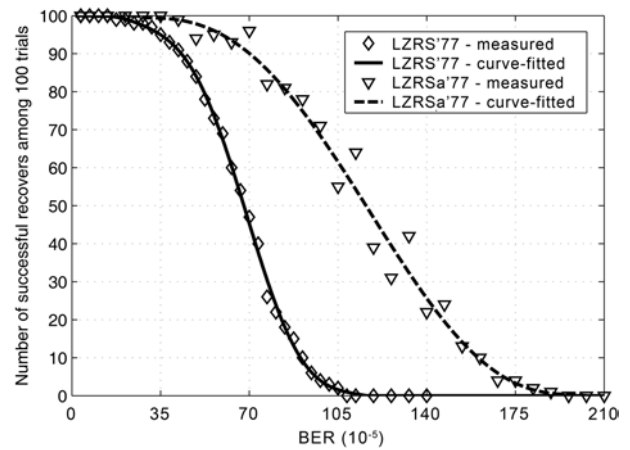


b)

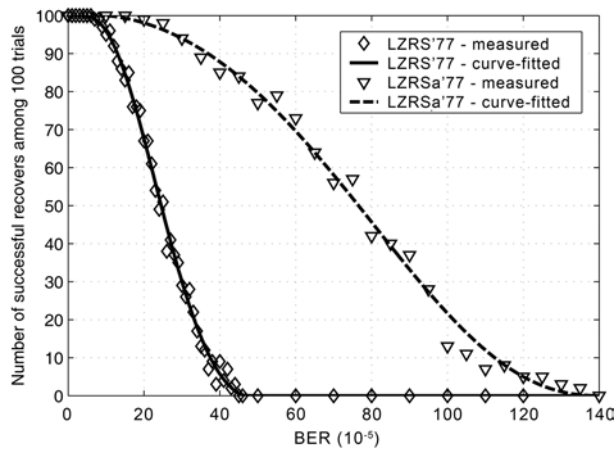
Figure 5: The number of successful recovers among 100 trials for two different length (L) substrings of the file *news*, for increasing number of bit errors geometrically distributed over the encoded strings, represented as Bit Error Rate (BER), end different algorithm used (LZRS'77 and LZRSa'77). a) $L = 3000$ bytes; b) $L = 30.000$ bytes.



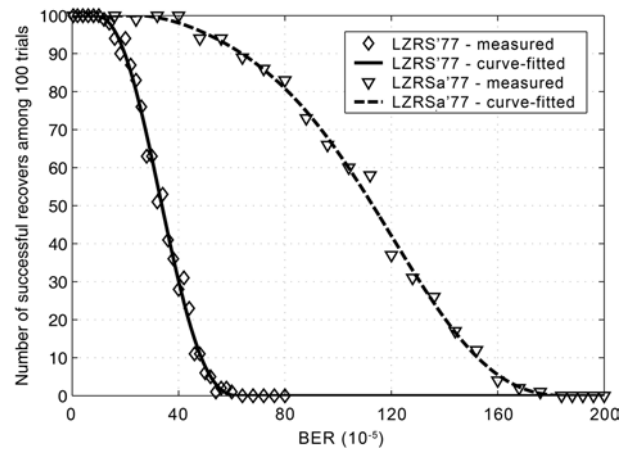
a)



a)



b)



b)

Figure 6: The number of successful recoveries among 100 trials for two different length (L) substrings of the file *progp*, for increasing number of bit errors geometrically distributed over the encoded strings, represented as BER, and different algorithm used (LZRS'77 and LZRSa'77). a) $L = 3000$ bytes; b) $L = 30.000$ bytes.

Figure 7: The number of successful recoveries among 100 trials for two different length (L) substrings of the file *geo*, for increasing number of bit errors geometrically distributed over the encoded strings, represented as BER, and different algorithm used (LZRS'77 and LZRSa'77). a) $L = 3000$ bytes; b) $L = 30.000$ bytes.

5. Conclusion

An improved version of the error-resilient LZ'77 data compression scheme was presented. It allows use of adaptive number of parity bits over different blocks of encoded data according to available redundancy in the blocks. Compared to the recently proposed LZRS'77 scheme allowing only constant number of parity bits along the whole string, the new solution better utilizes available redundancy in the string, resulting in a larger number of errors that can be effectively corrected. Such an improvement does not practically degrade the compression rate compared to the LZRS'77 algorithm. Even though the parity of each block has to be calculated each time from the redundancy of the previous block,

the time complexity of the new algorithm remains on the order of that of the LZRS'77 algorithm.

However, some legacy from the LZRS'77 algorithm still remains in the new algorithm and represents two unsolved problems. The first is a question of an online encoding process, which could not be achieved due to the reverse order of block processing. The second is protection of the first block while maintaining backward compatibility.

References

- 1 J. Ziv and A. Lempel, "A universal algorithm for sequential data compression," *IEEE Trans. Inf. Theory*, vol. IT-23, no. 3, May 1977, pp. 337–343.
- 2 M. E. Hellman, "On using natural redundancy for error detection," *IEEE Trans. on Commun.*, vol. 22, October 1974, pp. 1690–1693.
- 3 K. Sayood and J. C. Borkenhagen, "Use of residual redundancy in the design of joint source/channel coders," *IEEE Trans. on Commun.*, vol. 39, June 1991, pp. 838–846.
- 4 K. Sayood, H. Otu, and N. Demir, "Joint source/channel coding for variable length codes," *IEEE Trans. Commun.*, vol. 48, no. 5, May 2000, pp. 787–794.
- 5 M. J. Atallah and S. Lonardi, "Authentication of LZ-77 compressed data," *SAC 2003*, Melbourne, FL, 2003, pp. 282–287.
- 6 S. Lonardi and W. Szpankowski, "Joint source-channel LZ'77 coding," in *Proc. IEEE Data Compression Conf., Snowbird, UT, 2003*, pp. 273–282.
- 7 Y. Wu, S. Lonardi, and W. Szpankowski, "Error-resilient LZW data compression," in *IEEE Data Compression Conf., Snowbird, UT, 2006*, pp. 193–202.
- 8 S. Lonardi, W. Szpankowski, and M. D. Ward, "Error resilient LZ'77 data compression: algorithms, analysis, and experiments," *IEEE Trans. Inf. Theory*, vol. 53, no. 5, May 2007, pp. 1799–1813.
- 9 RFC 1951: DEFLATE compressed data format specification version 1.3, P. Deutsch, Aladdin Enterprises, May 1996. Available: <http://www.ietf.org/rfc/rfc1951.txt>
- 10 I. S. Reed and G. Solomon, "Polynomial codes over certain finite fields," *J. SIAM*, vol. 8, 1960, pp. 300–304.
- 11 The Calgary corpus. Available: <http://corpus.canterbury.ac.nz/descriptions/#calgary>

Arrived: 25. 02. 2011

Accepted: 26. 1. 2012

Influence of parameters of the flanged open-ended coaxial probe measurement setup on permittivity measurement

Jure Koselj*, Vladimir B. Bregar

Nanotesla Institute Ljubljana, Stegne 29, 1000 Ljubljana, Slovenia

Abstract: The flanged open-ended coaxial probe is studied using a full-wave model. Influence of parameters like a gap, sample thickness, set-up measurement geometry, probe impedance, size of the flange and size of the sample are investigated and presented. Study is limited to dielectric materials with different characteristics (low loss, high loss). The results showed that error in an air gap is the most important parameter that affects the permittivity measurement accuracy, but also several other parameters are important and present considerable constraints regarding application of open-ended coaxial probe. We also identified the optimal measurement geometry in order to minimize the effect of these parameters.

Key words: full-wave model, dielectric materials, open-ended coaxial probe

Vpliv parametrov merilnega sistema z odprto koaksialno sondo na meritve dielektričnosti

Povzetek: Predstavljena je študija odprte koaksialne sonde s prirobnico z uporabo modela polnovalne analize. Raziskali in predstavili smo vpliv parametrov kot so reža, debelina vzorca, merilna geometrija, impedanca sonde, velikost prirobnice in velikost vzorca. Študija je omejena na dielektrične materiale z različnimi karakteristikami (nizko izgubne, visoko izgubne). Rezultati so pokazali, da ima največji vpliv na merilno točnost meritve dielektričnosti zračna reža, poleg tega pa so pomembni tudi ostali parametri, ki predstavljajo precejšnje omejitve aplikacij z odprto koaksialno sondo. Prav tako smo poiskali optimalno merilno geometrijo, da bi zmanjšali efekt parametrov merilnega sistema z odprto koaksialno sondo.

Ključne besede: polnovalni model, dielektrični materiali, odprta koaksialna sonda

*Corresponding Author's e-mail: jure.koselj@nanotesla.si

1. Introduction

Each material has distinct dielectric properties and knowing these properties enables engineers to use appropriate materials in specific application. Measuring and understanding how dielectric properties of material vary at microwave frequencies is important in many fields like wireless communication, radar detection or biomedical application.

Intensive studies have been done in development of measurement of the complex permittivity. Many factors like frequency range, required measurement accuracy, sample size, surface topology, state of the material (liquid, solid, powder, thin film), destructive or nondestructive nature of measurements, have to be considered when choosing appropriate method for measurement permittivity. Methods

commonly used include transmission/reflection and resonance methods. Transmission/reflection methods have advantage over resonance methods because they have wide frequency range, are simple to use and can measure lossy materials but are less accurate than resonance methods /1-4/. On the other hand resonance methods are limited to discrete frequencies, defined by resonator dimensions, and to materials with low losses. For transmission/reflection method there are several different approaches by using coaxial waveguide /5, 6/, planar waveguide /7, 8/, rectangular waveguide /9-10/ or free-space method /11-13/. The latter two present frequency limitations due to size of the tested sample and planar waveguides methods are limited to the solid and thick film materials. Hence the most widely used method among transmission/reflection methods is open-ended coaxial line due to its simplicity and accuracy in broadband measurements.

An alternative characterization method based on the reflection is application of an open-end coaxial probe /14/. Simple set-up and sample geometry present significant advantage over other methods; however, for determination of the sample material parameters a good model of wave propagation is needed. There are several models for open-ended coaxial probe like capacitance model /5, 15/, radiation model /16/, virtual line model /17/, rational function model /18, 19/ and full-wave model /14, 20, 21, 24/, with increasing accuracy and also complexity.

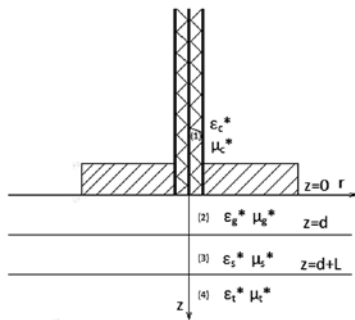


Figure 1: Flanged open-ended coaxial probe measurement setup with layered dielectric sample with termination.

The aim of this paper is to analyze in detail the open-end coaxial probe system and determine which parameters are affecting measured reflection coefficient for given measurement geometry and evaluate the effect of individual parameter. The analysis is made with the full-wave model and thus presents the most accurate analytical representation of the open-end coaxial probe. We focused the study to non magnetic materials as they are both more commonly measured and require simpler measurement set-up compared to the magnetic materials. In addition, we analyzed the system for both liquid and solid samples and for materials that have either low or high dielectric losses. Our results show the effect of different parameters on permittivity (reflection coefficient) and therefore help researchers to select appropriate measurement geometry for measurement solid materials (low and high loss).

2. Methods

We focused on the non-magnetic materials where the tested sample has permittivity $\epsilon_s^* = \epsilon_0[\epsilon_s' - j\epsilon_s'']$ and permeability $\mu_s^* = \mu_0$, ϵ_0 is permittivity of vacuum and μ_0 is permeability of vacuum. The geometry of the problem as shown in Fig.1 consists of an internal and external region. The internal region represents interior of an open-ended coaxial line, while external region is a layered medium. The coaxial line has inner diameter $2a$, outer diameter $2b$ and is filled with a low loss material of permittivity $\epsilon_c^* = \epsilon_0\epsilon_c'$ and permeability $\mu_c^* = \mu_0$. To determine the influence of parameters on measured permittivity we

calculate reflection coefficient with full-wave model /14/ and then use this value in optimization algorithm (Matlab's fsolve trust-region-dogleg algorithm) as a substitute for a measured reflection coefficient. To eliminate measurement uncertainties and have well defined geometry we decided to use model instead of actual measurements. Each parameter of interest was varied to get results (permittivity) and afterwards we compared true value which was used to calculate the true reflection coefficient with the one obtained from optimization.

$$\Delta\epsilon = \left| 1 - \frac{\epsilon_i}{\epsilon_r} \right|, \quad (1)$$

$$\Delta d = d_r - d_i, \quad \Delta L = L_r - L_i, \quad (2)$$

where ϵ_r is true value of permittivity, ϵ_i is the value obtained with optimization, d_r and d_i are values of true gap thickness and gap thickness used in optimization, L_r and L_i are values of true sample thickness and sample thickness used in optimization algorithm. The true permittivity of each material was calculated for two probes with following parameters of $a = 1.51$ mm, $b = 4.90$ mm, $\epsilon_c = 1.99$ (realistic 50 Ω coaxial probe 1), $a = 0.255$ mm, $b = 0.84$ mm, $\epsilon_c = 2.04$ (realistic 50 Ω coaxial probe 2), $\epsilon_t = 1$, $d = 50$ μm , $L = 500$ μm and 12 TM_{0n} modes were used. In our study we used values for different materials such as Teflon ($\epsilon_r = 2-0.003j$ at 10 GHz), mixture of titanium dioxide and wax ($\epsilon_r = 10-0.09j$ at 10 GHz) and mixture of graphite and wax ($\epsilon_r = 40-25j$ at 10 GHz) to show the effect of low and high loss material on the relative error in permittivity.

We also used different measurement set-up geometries to find out which would be optimum for dielectric materials. The full-wave model has three distinct measurement set-up geometries, semi-infinite (model 0), short-circuit (model 1) and dielectric terminated (model 2) geometry.

3. Results and discussion

Influence of parameters on permittivity

The full-wave model used for calculation of reflection coefficient as mentioned earlier is exact but in the case of real measurement set-up it has some disadvantages due to the assumption that the flange and sample extend to infinity in radial direction. These conditions are never satisfied in real measurement, however, the effect of using finite sample and flange in radial dimensions was investigated by De Langhe et al. /22/. It was found that if the ratio between the aperture size and the surface of the sample is greater than 2.5, the measured characteristics (amplitude and phase) are very close to those of the infinite sample. If the sample thickness decreases, one sees larger differences and if thickness increases, the differences get smaller. It was also found

that if the flange radius is at least two times larger than the outer radii of the coaxial probe, only small differences are seen in amplitude and phase. Thus accurate measurements can be made with reasonable flange and sample dimensions despite assumption of infinity.

Influence of gap and sample thickness with different measurement set-up geometry

One of the important uncertainties is a gap between the sample and the probe as this gap is very difficult to measure. But in reality sample can be also concave or convex and this effect was investigated by A.-K. A. Hassan et al. /23/. It was found that for the concave sample the reflection coefficient is strongly affected by both flange diameter and the radius of concave sample, whereas in the case of convex sample reflection coefficient is affected for small radii of the sample, but the flange diameter has negligible effect on the reflection coefficient. It is concluded that an improve technique is required to achieve better accuracy of measurement of concave samples, while measurements of convex samples, in general, are in good agreement with published data. In order to evaluate how variation of an air gap and sample thickness affect complex permittivity a number of calculations with different measurement set-up geometries were made. In Fig. 2 we compare how error in air gap influences real and imaginary part of permittivity of high loss sample (graphite in wax composite) at 10 GHz.

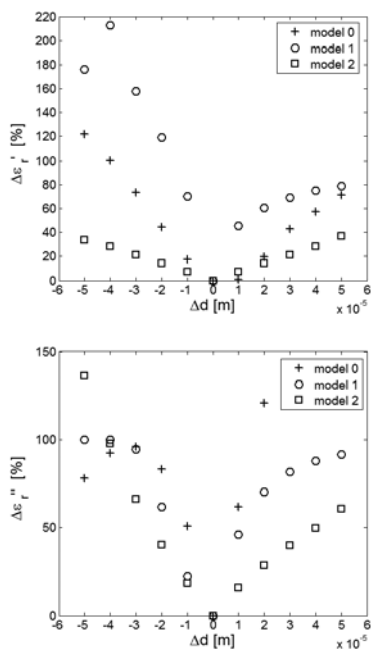


Figure 2: Error in real and component of permittivity in percentage as a function of an air gap for a frequency of 10 GHz for graphite mixed with wax with different measurement set-up geometries.

For graphite composite model 2 has the lowest dependence of an air gap on permittivity, nevertheless, error is for both components of permittivity over 40% at air gap value $\Delta d = 50\mu\text{m}$. One can see similar results with model 2 for composite of titanium dioxide and wax (Fig. 3). Fig. 4 shows that model 0 and model 2 have similar error in real component of permittivity of teflon, while error in imaginary component clearly shows that model 2 produces better results when the air gap is varied. From Figs. 2-4 one can conclude both that model 2 has in general the least amount of relative error, and that the permittivity of high-loss material is more affected by the air gap.

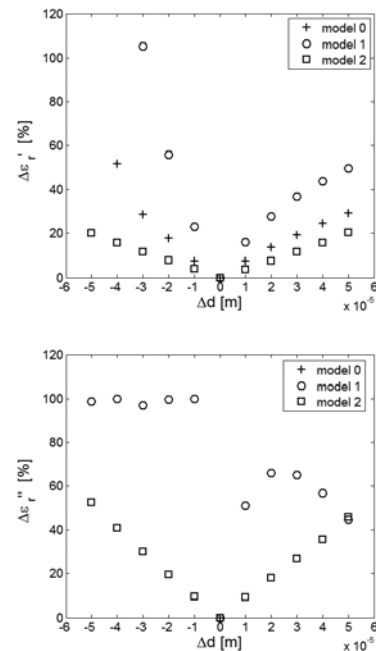


Figure 3: Error in real and imaginary component of permittivity in percentage as a function of an air gap for a frequency of 10GHz for titanium dioxide mixed with wax with different measurement set-up geometries.

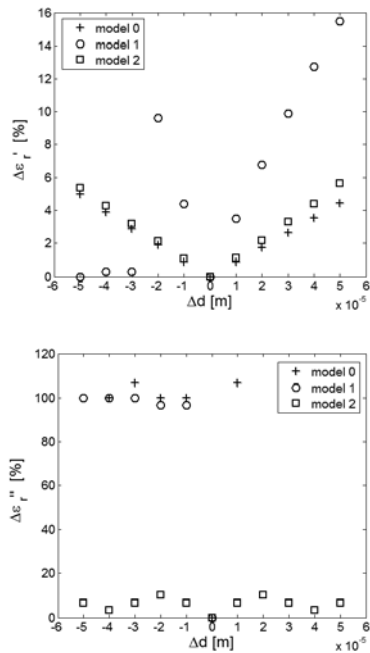


Figure 4: Error in real and imaginary component of permittivity in percentage as a function of an air gap for a frequency of 10GHz for teflon with different measurement set-up geometries.

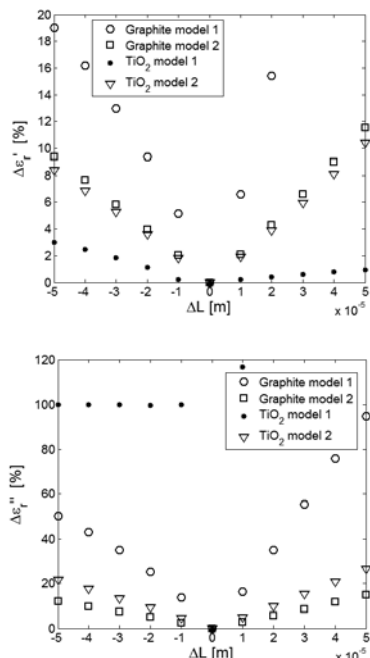


Figure 5: Error in real and imaginary component of permittivity in percentage as a function of the sample thickness for a frequency of 10GHz for titanium dioxide-wax and graphite-wax composites with different measurement set-up geometries.

Fig. 5 illustrates the dependence of sample thickness on permittivity. The results show that in general model 2 produces best results on both materials. Also it is shown that error in sample thickness produces higher error in imaginary component of permittivity of low loss material, this can be due to low absolute value of imaginary component of permittivity and therefore larger error. We obtained similar results for teflon which has low relative error for real component and highest relative error for imaginary component of permittivity, this can be also explained by low absolute value of imaginary component of permittivity and therefore larger error.

Influence of probe size and frequency

With simple test we also examined the effect of probe dimensions and operating frequency on the required the thickness of sample that can be used as semi-infinite sample. For reference we computed reflection coefficient for the geometry of semi-infinite sample. Then for finite thickness geometry we adapt the thickness of sample so that the reflection coefficient computed had the same value (on 6th decimal place) as reference reflection coefficient. Results for different probe dimensions can be seen in table 1.

Table 1: Influence of probe dimensions and frequency on electromagnetic field penetration for different materials

| probe dimensions | | frequency [GHz] | thickness [mm] | ε of material |
|------------------|--------|-----------------|----------------|---------------|
| a [mm] | b [mm] | | | |
| 1,51 | 4,87 | 1 | 1120 | 10-0,01i |
| 1,51 | 4,87 | 5 | 2070 | 10-0,01i |
| 1,51 | 4,87 | 10 | 2080 | 10-0,01i |
| 1,51 | 4,87 | 1 | 54 | 10-25i |
| 1,51 | 4,87 | 5 | 18 | 10-25i |
| 1,51 | 4,87 | 10 | 11 | 10-25i |
| 0,225 | 0,84 | 1 | 20 | 10-25i |
| 0,225 | 0,84 | 5 | 11 | 10-25i |
| 0,225 | 0,84 | 10 | 7 | 10-25i |
| 0,225 | 0,84 | 1 | 36 | 10-0,01i |
| 0,225 | 0,84 | 5 | 182 | 10-0,01i |
| 0,225 | 0,84 | 10 | 211 | 10-0,01i |

As expected, for both probes material with higher dielectric losses needs lower thickness to be applicable as semi infinite sample. For the larger probe and relatively low-loss material the required thicknesses are substantial. The smaller probe shows the same dependence but required thicknesses are as expected much lower. But it is evident that operating frequency and probe dimensions are key factors when one wants to use semi-infinite geometry for measurement set-up.

Table 2 comprises probe dimensions, frequency of operation, true and obtained value of permittivity. The true value is permittivity used for calculation of reflection coefficient with parameters of $d=50 \mu\text{m}$, $L=500 \mu\text{m}$, mode=12, model=2 and frequency=10 GHz, the obtained value is permittivity obtained by optimization algorithm from calculated reflection coefficient with parameters of $d=0 \mu\text{m}$, $L=500 \mu\text{m}$, mode=12, model=2 and frequency at 10 GHz.

Table 2: Comparison of error in complex permittivity for used probes at 10 GHz

| probe dimensions | | frequency [GHz] | true value of ϵ | obtained value of ϵ |
|------------------|--------|-----------------|--------------------------|------------------------------|
| a [mm] | b [mm] | | | |
| 1,51 | 4,87 | 10 | 10-0,09i | 7,96-0,049i |
| 0,225 | 0,84 | 10 | 10-0,09i | 3,73-0,012i |
| 1,51 | 4,87 | 10 | 2-0,003i | 1,89-0,0028i |
| 0,225 | 0,84 | 10 | 2-0,003i | 1,60-0,0016i |
| 1,51 | 4,87 | 10 | 40-25i | 25,31-9,85i |
| 0,225 | 0,84 | 10 | 40-25i | 24,66-9,10i |

Table 2 shows the difference between error in obtained permittivity with small and large probe. It is also seen that for low-loss materials small probe produces higher error in permittivity than large probe if the value of the air gap (d) is not at the correct value (the difference is $50 \mu\text{m}$). We obtain similar results for other values of air-gap uncertainty Δd . For high-loss materials both probes give similar error in obtained permittivity. The frequency has little effect on error of permittivity for both probes and the above conclusions are valid over the operating frequency range.

Influence of TM_{0n} modes

In our study we also analyzed the influence of number of used TM_{0n} modes with different geometry set-up. For reference value we used 12 TM_{0n} modes. We observed different behavior on high-loss material as it has the smallest relative error in real part of permittivity with model 0 (Fig. 6) and highest relative error with model 1 and model 2. With model 1 and model 2 low-loss materials

has smallest relative error in real part of permittivity. One observes the opposite in relative error for imaginary part of permittivity for all three models (model 2 has the lowest relative error) where high-loss material has lowest error among all three materials. Again, higher relative error in imaginary component can be explained with low absolute value and therefore high relative error.

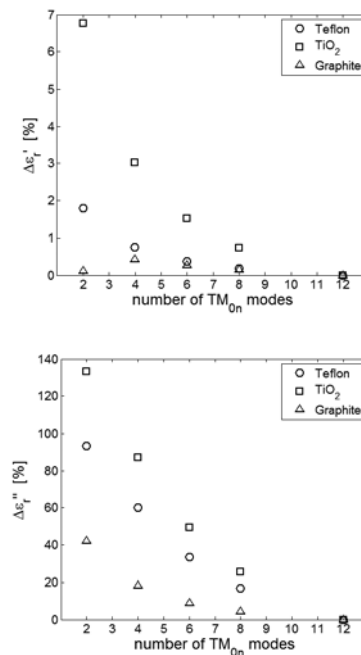


Figure 6: Error in real and imaginary component of permittivity in percentage as a function of a number of TM_{0n} modes for a frequency of 10GHz for different materials with measurement set-up geometry of model 0.

From data shown in figure 6 we can conclude that higher modes affect permittivity and should be used as many as possible. We used only 12 modes as reference and it is obvious that low number of used TM_{0n} modes contribute to measurement error.

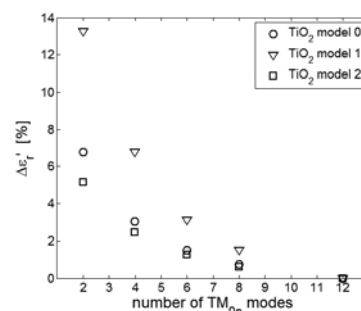


Figure 7: Error in real component of permittivity in percentage as a function of a number of TM_{0n} modes for a frequency of 10GHz for titanium dioxide mixed with wax with different measurement set-up geometries.

Figure 7 shows that the optimum geometry set-up for titanium dioxide composite (relatively low-loss material) is dielectric terminated geometry (model 2). The same results came for imaginary component. Similar results were obtained for teflon and graphite composite. This is not surprising because in geometry of model 2 strong electric fields interact with sample material, thus giving good measurement results. And we also confirm that model 1 which has short-circuited termination has the worst results due to the boundary condition at the sample position. Electric fields in the sample are weak (magnetic fields are strong) and are approaching zero at the termination.

4. Conclusion

In our study of open-ended coaxial probe system we analyzed effect of several key parameters of measurement set-up on measurement error of permittivity. The analysis showed that error in an air gap (error between actual and measured air gap) is clearly the single most important parameter as it produces highest error in permittivity among all studied parameters. Of the studied cases the least effect on error in permittivity was observable for low-loss materials with dielectric terminated measurement geometry.

Of other parameters size of the probe and operating frequency affect penetration of the field through the sample as large probe produces more field penetration in sample material than small probe. As expected, our calculations show that at high frequencies there is less penetration than at low frequencies for the case of high-loss materials. Just the opposite is seen for low-loss materials. Also uncertainty of the sample thickness does have some effect on the measured value of permittivity, but this parameter is much easier to control, especially for solid samples. Also, we analyzed the effect of the number of TM modes in calculations and clearly showed that with lower mode number the error can be significant. This is especially important since to obtain the permittivity one compares measured and calculated values of reflection coefficient. The accuracy of the obtained permittivity values is inherently limited by the accuracy of the calculation and this further strengthens the grounds for the use of the full-wave model with several TM modes over simpler models of open-ended coaxial probe.

When taken together our results show that the open-end coaxial probe system can be very problematic for solid samples and special effort must be applied to the air gap evaluation in order to get relevant values. Otherwise the method is limited to liquid or deformable materials where a gap can be eliminated. Further, it

can be concluded that dielectric terminated geometry (model 2) is best option among feasible measurement setup geometries for permittivity measurements and this is valid for both high- or low-loss materials.

References

- 1 M.D. Janezic and J. Baker-Jarvis, Full-wave analysis of a split cylinder resonator for nondestructive permittivity measurements, *IEEE Trans. on microwave theory and tech.*, Vol. 47 (10), pp. 2014-2020, 1999
- 2 W.E. Courtney, Analysis and evaluation of a method of measuring the complex permittivity and permeability of microwave insulators, *IEEE Trans. on microwave theory and tech.*, Vol. MTT-18 (8), pp. 476-485, 1970
- 3 G. Kent, Nondestructive permittivity measurement of substrates, *IEEE Trans. on Instrum. and measurement*, Vol. 45 (1), pp. 102-106, 1996
- 4 J. Krupka and C. Weil, Recent advances in metrology for the electromagnetic characterization of materials at microwave frequencies, 12th Intern. Conf. on Microwaves and radar (MIKON '98), Vol. 4, pp.243-253, 1998
- 5 M.A. Stuchly, T.W. Athey, G.M. Samaras and G.E. Taylor, Measurement of radio frequency permittivity of biological tissues with an open-ended coaxial line: Part II - experimental results, *IEEE Trans. on microwave theory and tech.*, Vol. MTT-30 (1), pp. 87-92, 1982
- 6 V.K. Ivanov, A.O. Silin and A.M. Stadnik, Determination of dielectric permittivity of materials by an isolated coaxial probe, *Radioelectronics and communications systems*, Vol. 50 (7), pp. 367-374, 2007
- 7 P. Queffelec et al., A microstrip device for the broad band simultaneous measurement of complex permeability and permittivity, *IEEE Transactions on magnetics*, Vol. 30 (2), pp. 224-231, 1994
- 8 N. Berger et al., Broadband non-destructive determination of complex permittivity with coplanar waveguide fixture, *Electronics letters*, Vol. 39 (20), 2003
- 9 N.N. Al-Moayed et al., Nano ferrites microwave complex permeability and permittivity measurements by T/R technique in waveguide, *IEEE Transactions on magnetics*, Vol. 44 (7), pp. 1768-1772, 2008
- 10 K.J. Bois, A.D. Benally and R. Zoughi, Multimode solution for the reflection properties of an open-ended rectangular waveguide radiating into a dielectric half-space: The forward and inverse problem, *IEEE Trans. on Instrum. and measurement*, Vol. 48 (6), pp. 1131-1140, 1999

- 11 D.K. Ghodgaonkar, V.V. Varadan and V.K. Varadan, Free-space measurement of complex permittivity and complex permeability of magnetic materials at microwave frequencies, *IEEE Trans. on Instrum. and measurement.*, Vol. 39 (2), pp. 387-394, 1990
- 12 I.S. Seo, W.S. Chin and D.G. Lee, Characterization of electromagnetic properties of polymeric composite materials with free-space method, *Composite structures*, Vol. 66, pp. 533-542, 2004
- 13 C.A. Grosvenor et al., Electrical material property measurements using a free-field, ultra-wideband system, 2004 annual report conference on electrical insulation and dielectric phenomena, pp.174-177, 2004
- 14 J. Baker-Jarvis, M.D. Janezic, P.D. Domich and R. G. Geyer, Analysis of an open-ended coaxial probe with lift-off for nondestructive testing, *IEEE Trans. on Instrum. and measurement.*, Vol. 43 (5), pp. 711-718, 1994
- 15 T.W. Athey, M.A. Stuchly and S.S. Stuchly, Measurements of radio frequency permittivity of biological tissues with an open-ended coaxial line: Part I, *IEEE Trans. on microwave theory and tech.*, Vol. MTT-30 (1), pp. 82-86, 1982
- 16 M.M. Brady, S.A. Symons and S.S. Stuchly, Dielectric behavior of selected animal tissues in vitro at frequencies from 2 to 4 GHz, *IEEE Trans. on biomedical engineering*, Vol. BME-28 (3), pp. 305-307, 1981
- 17 F.M. Ghannouchi and R.G. Bosisio, Measurement of microwave permittivity using a six-port reflectometer with an open-ended coaxial line, *IEEE Trans. on Instrum. and measurement.*, Vol. 38 (2), pp. 505-508, 1989
- 18 J.M. Anderson, C.L. Sibbald and S.S. Stuchly, Dielectric measurements using a rational function model, *IEEE Trans. on microwave theory and tech.*, Vol. 42 (2), pp. 199-204, 1994
- 19 S.S. Stuchly, C.L. Sibbald and J.M. Anderson, A new aperture admittance model for open-ended waveguides, *IEEE Trans. on microwave theory and tech.*, Vol. 42 (2), pp. 192-198, 1994
- 20 C.L. Li and K.M. Chen, Determination of electromagnetic properties of materials using flanged open-ended coaxial probe - full-wave analysis, *IEEE Trans. on Instrum. and measurement.*, Vol. 44 (1), pp. 19-27, 1995
- 21 G. Panariello, L. Verolino and G. Vitolo, Efficient an accurate full-wave analysis of the open-ended coaxial cable, *IEEE Trans. on microwave theory and tech.*, Vol. 49 (7), pp. 1304-1309, 2001
- 22 P. De Langhe, L. Martens and D. De Zutter, Design rules for an experimental setup using an open-ended coaxial probe based on theoretical modeling, *IEEE Trans. on Instrum. and measurement.*, Vol. 43 (6), pp. 810-817, 1994
- 23 A.-K.A. Hassan, X. Deming, Z. Yujian, Analysis of open-ended coaxial probe for EM-properties of curved surfaces materials testing y FDTD method, 1999 International conference on Computational Electromagnetics and Its Applications, pp. 549-552, 1999
- 24 J.W. Steward and M.J. Harvilla, Electromagnetic characterization of a magnetic material using an open-ended waveguide probe and a rigorous full-wave multimode model, *J. of Electromagn. Waves and appl.*, Vol. 20 (14), pp. 2037-2052, 2006

Arrived: 18. 04. 2011

Accepted: 26. 1. 2012

Kinetics of discharging arc formation

*France Pavlovčič**

University of Ljubljana, Faculty of electrical engineering, Ljubljana, Slovenia

Abstract: A scope of this paper is to present a mechanism of a discharge arc ignition in mechanically operated electric contacts in a gas mixture medium, such as the air. Introductory, the electric contacts are classified due to their mechanic and electric operation with given examples and corresponding most probable transient phenomena during their typical operation. In the first place, drawn arcs being metal vapour arcs of contact materials are most wearisome and destructive to the electric contacts, but mostly the discharging arcs are just preceding phenomenon to metal vapour arcs, and as such, they have indirectly the same effect on weariness of the electric contacts as the drawn arcs with intensity proportional to the arc current. A phenomenon of discharging arcs formation is discussed in this paper, which is an end result of throughout ionization and a throughout ionized path formation. The author's mathematical model calculates average kinetic energy of electrons in the non-homogeneous electric field due to an electron primary and secondary flow between two spherical electrodes. Exciting energy of gas molecules gained through electron impacts causes ionization of the molecules if the energy is high enough, but with the lower energy levels, dissociation of these molecules is carried out if they are at least two-atom molecules. Further on, the dissociated particles are associating in the other molecules, being also influenced by the electric field and so resulting in another processes of ionization and dissociation, and further on, recombination and association. There is continuous kinesis within the gas mixture, which gains a steady state mixture of the constituent gases, until the throughout ionization of one of the constituent gases at least is established by the increasing electric field throughout a space between the electrodes. So far, physics of this phenomenon deals with the electron kinetic energy and the energy of other energy carriers, such as photons and displacement current, in the electric field, and its transferring to molecules as the exciting energy causing their ionization and the ion recombination and the molecule dissociation, but the dissociated particles are part of chemical process, which is, together with their association in the newly produced compounds, dealt by chemism of this phenomenon. The new gaseous compounds have their own physics of their excitation in the electric field, and further on, the physics is followed by chemism of newly produced gases. Both of them, the physics and the chemism, results in kinetics of the throughout ionization formation and hence the discharging arc formation.

Keywords: discharging arc, gas throughout ionization, exciting energy, gas molecule dissociation, gas molecule ionization, gas chemism in electric field.

Kinetika nastanka razelektritvenih oblokov

Povzetek: Namen tega članka je predstavitev mehanizma vžiga razelektritvenega obloka v mehansko delujočih električnih kontaktih v zmesi plinov, kot je zrak. Uvodoma so električni kontakti razdeljeni glede na njihovo mehansko in električno delovanje s podanimi primeri in najbolj verjetnimi spremljajočimi tranzientnimi pojavi med njihovim tipičnim delovanjem. Na prvem mestu glede na obrabo in uničenjem električnih kontaktov so potegnjeni obloki, ki so obloki s kovinsko paro kontaktnih materialov. Toda večinoma so razelektritveni obloki predhodni pojav k oblokom s kovinsko paro in kot taki posredno enako učinkujejo na obrabo kontaktov kot potegnjeni obloki z jakostjo proporcionalno toku obloka. V tem članku je obravnavan pojav nastanka razelektritvenega obloka, ki je končni rezultat nastanka skožnje ionizacije in skožnje ionizacijske poti. S pomočjo avtorjevega matematičnega modela se izračunava povprečna kinetična energija elektronov v nehomogenem električnem polju zaradi primarnega in sekundarnega elektronskega toka med dvema kroglastima elektrodama. Vzbujevalna energija plinskih molekul, pridobljena s trki elektronov, povzroča ionizacijo molekul, če je energija dovolj visoka. Z nižjimi nivoji vzbujevalne energije se vrši disociacija – razdruževanje molekul, če se le-te vsaj dvoatomske. Nadalje se razdruženi delci združujejo v molekule drugih spojin in tako preidejo v druge procese ionizacije in disociacije ter nadalje rekombinacije in združevanja. V plinski mešanici, ki doseže stalno mešanico sestavnih plinov, obstaja nepretrgana kineza, dokler se pri večanju električnega polja ne vzpostavi skožnja ionizacija vsaj enega sestavnega plina plinske mešanice preko prostora med elektrodama. Fizika tega pojava obravnava kinetično energijo elektronov in energije drugih nosilcev, kot so fotoni in poljski tok, v električnem polju in njen prenos na molekule v obliki vzbujevalne energije, ki povzroča njihovo ionizacijo in rekombinacijo ionov ter razdruževanje molekul. Vendar razdruženi delci so del kemičnega procesa, ki je, skupaj z njihovim združevanjem v novo nastale spojine, obravnavan kot kemizem pojava. Nove plinaste spojine imajo svojo fiziko vzbujanja v električnem polju, in nadalje, fiziki sledi kemizem novo nastalih plinov. Oboje, fizika in kemizem sestavljata kinetiko nastanka skožnje ionizacije in tako tudi nastanka razelektritvenega obloka.

Ključne besede: razelektritveni oblok, skožnja ionizacija plinov, vzbujevalna energija, disociacija plinskih molekul, ionizacija plinskih molekul, kemizem plinov v električnem polju.

* Corresponding Author's e-mail: france.pavlovic@fe.uni-lj.si

1. Introduction

Researching arcing between electric contacts, there are some differences between the transient phenomena due to contact mechanic and electric operation. When shifting contacts are making contact, their bouncing occurs, and hence drawn arcs, which are metal vapour arcs – vapour of contact materials, which usually are metals [1]. The drawn arcs occur also in holding mode with sliding contacts, since they slips in some kinds of their design (sliders, trolleys, slip rings) while they are holding electric contact. But, the drawn arcs are accompanying phenomenon at the operation of breaking electric current, especially in heavy duty operations, nevertheless, which kind of mechanic operation is used with the electric contact. So far, these differences between the electric contacts are over-viewed in Tab. 1.

Table 1: The clasification of electric contacts due to their machanic and electric operations in connection with the possible transient phenomena associated with their operations.

| ELECTRIC CONTACTS | | | | | | |
|---|---|---|---------------------------------------|--------------------------------|--------------------------------|--|
| TRANSIENT PHENOMENA | EXAMPLES | MOVEABLE | | | | STACIONARY |
| | | SHIFTING | | SLIDING | | |
| | | perpendicular or angular direction to contact surface | parallel direction to contact surface | slipping | slipping & steady | |
| ELECTRIC OPERATIONS | MECHANIC OPERATIONS | holding | making | breaking | switching | STACIONARY |
| | | break before make before break | break before make before break | break before make before break | break before make before break | |
| none | rivet on-off switch | holding | moving | moving & steady | switching | soldered welded wrapped faston screw bus |
| >discharging arcs at all operations >drawn arcs due to bouncing at making >drawn arcs at breaking | heavy duty relay telecommunication relay | break before make before break | break before make before break | break before make before break | break before make before break | |
| none | plug-socket connector | holding | slipping | slipping & steady | switching | none |
| >discharging arcs at making and breaking >drawn arcs at holding >drawn arcs at breaking | slider trolley, slip ring sampling switch commutator | break before make before break | break before make before break | break before make before break | break before make before break | |
| >discharging arcs at all operations >drawn arcs at making >drawn arcs at breaking | rotary switch with interruption rotary switch without interruption | break before make before break | break before make before break | break before make before break | break before make before break | |

On the other hand, discharging arcs ignite by electric breakdown of throughout ionized surrounding gas medium between contact members [2], when they are in separated position, while they are closing at making operation, are opening at breaking operation or are opened still in switch-off position. The gaseous substance is surrounding gas medium, physically and chemically changed by electric field between the contact members.

The differences between the drawn arcs and the discharging arc are:

- in the time-depended electric current flow through gaseous substance between the contact members: in the drawn arcs, the current flow continues without interruption; but in the discharging arcs, it starts at zero and increases up to the arc ignition, or it is interrupted, reduced to zero and re-established through the arc ignition;
- in plasma particles, which depend on the gaseous substance between the contact members: in the drawn arcs, the ionized metal vapour of contact materials; but in the discharging arcs, the ionized gas of surrounding gas medium.

The discharging arcs would not be harmful by themselves to cause the contact wear by the involved electrons and the ions of the surrounding gas constituents, if the discharging arc did not invoke the metal vaporization and the ionization of the contact material followed by material disposition from one to another contact member. In this paper the kinetics, and thereby, the physics and the chemism of discharging arc are discussed.

2. The physics of the gas throughout ionization

The current between the separating contact members instantly falls towards zero value with the discharging arcs. A transient voltage appears due to time-derivative of the current, which extends to a breakdown voltage value of the medium – Fig. 1. The medium of the discharging arc is the existing ionized gas from the surrounding space.

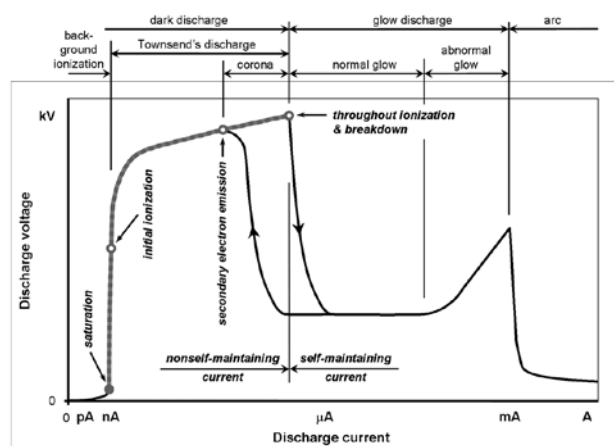


Figure 1: The principle electric discharge *UI* characteristic [3] with the range hereafter dealt in this discourse.

With the increasing transient voltage, the dielectric breakdown of the insulating gas occurs, and due to it, the electric current increases. The kind of discharge, which follows, depends on the current through the gas: the dark discharge, the glow discharge or the discharging arc, either stable or unstable, the latter one resulting in sparking. The separating contact rivets in some opening distance are substituted by a spark gap of two spherical electrodes to research the discharging arc formation. Therefore the mathematical model of the spark gap was developed to study the electric field and the ionizing process in the gap. The electric load is an air coil in this mathematical model, replaced by a conceptual circuit equivalent in very simplified way.

The spark gap consists of two spherical electrodes with the same radius r_0 , separated by the distance d_{sur} between their surfaces and the gas medium around them. An anode is positively charged and a cathode has a negative charge of the same absolute amount of charge in the first stage of the arc development, when there is no charge in the space nearby the cathode, so far without a cathode layer. The cathode is earthed so that a positive charge flows from the cathode to the earth. Due to the mutual influence of the anode and the cathode charges, the equivalent point charges of the anode and the cathode, $+Q_1$ and $-Q_1$, lie in the eccentric positions in the relevant spheres – Fig. 2. In the cathode layer shown in Figs 2 and 3, when it comes to existence, there are a positive ions layer and an electrons layer. Since the positive ions layer is closer to the cathode than the electrons layer, a distributed additional negative charge is induced just beneath the cathode surface. The integral of the distributed positive charge of the ions layer over volume, the integral of the distributed charge of the electrons layer over volume, and the integral of the distributed additional negative charge of the cathode are equal by their absolute values. Due to the signs assigned to these charges, the sum of these integrals equals to the integral of the distributed additional negative charge of the cathode when radii of the ions layer and the electrons layer are limiting to the cathode radius, and so far the integrated additional negative charge of the cathode is substituted by the equivalent point charge $-Q_2$ in the cathode centre.

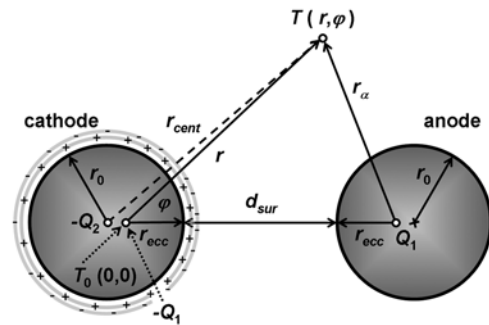


Figure 2: The geometrical drawing of the cathode with the layer of spatial distributed electric charge of integrated values of $+Q_2$ and $-Q_2$ around the cathode, the anode and the distances between them in $r-\varphi$ coordinate system.

The mathematical model in spherical coordinates (r, φ, Φ) is simplified to two dimensional space $(r, \varphi, \Phi = \pi/2) \rightarrow (r, \varphi)$ because the electric field is rotary symmetrical. Hereafter, to avoid misunderstanding, the usage of Cartesian coordinates refers strictly to the plane (r, φ) , and not to three dimensional space. The eccentric positions of the equivalent point charges are defined by eccentric radius r_{ecc} as it is shown in Fig. 2, and further on, the eccentric position of the cathode equivalent point charge $-Q_1$ is the zero point of the coordinate system. A potential U of any point $T(r, \varphi) = T(r, r_\alpha, r_{cent})$ is an algebraic sum of the partial potentials caused by the anode and the cathode charges since the potential is scalar value. It is defined by the following equation in the bi-radial coordinates r, r_α plus dependent coordinate r_{cent} as follows [4]:

$$U(r, r_\alpha, r_{cent}) = \frac{Q_1}{4 \cdot \pi \cdot \epsilon} \left(-\frac{1}{r} + \frac{1}{r_\alpha} + \frac{1}{r_{ecc}} - \frac{1}{r_{ecc} + d_{sur}} \right) + \frac{Q_2}{4 \cdot \pi \cdot \epsilon} \left(-\frac{1}{r_{cent}} + \frac{1}{r_0} \right) \quad (1)$$

where Q_1 and Q_2 are absolute values of point charges. Variables of this equation are coordinates, as already mentioned, r, r_α, r_{cent} as shown in Fig. 2.

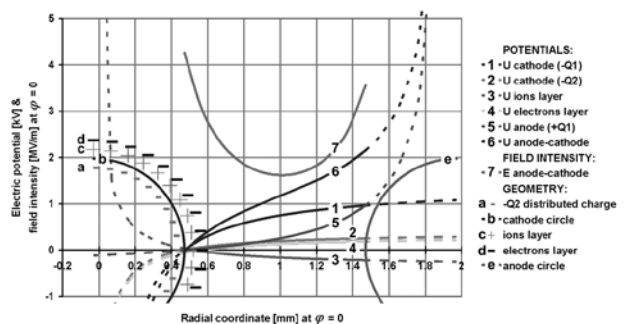


Figure 3: The analysis of the electric potentials and the electric field intensity due to the anode, the cathode and the spark gap geometry.

Since the cathode is earthed, its surface potential is defined as zero, which is also zero at the following point on its surface:

$$r = r_{ecc} \wedge r_a = r_{ecc} + d_{sur} \wedge r_{cent} = r_0 \Leftrightarrow U = 0 \quad (2),$$

hence the geometric constants in Eq. (1). The electric charge Q_1 is modelled due to the primary electric field and the primary electron emission, but Q_2 due to the spatial distributed electric charges in the cathode layer as in Fig. 2 maintaining both the primary and the secondary electron emission.

Solving the geometry of the system in Fig. 2, following geometric quantities are obtained: firstly, the surface radius of the cathode r_{surk} depending on the angle coordinate φ and used later in this discussion, and secondly, the radial coordinates r_a and r_{cent} in terms of the polar coordinates r and φ , which transform Eq. (1) in the function $U(r, \varphi)$ – the electric potential depending on the polar coordinates.

Between the anode and the cathode a certain voltage is applied, as follows:

$$r = r_{ecc} + d_{sur} \wedge \varphi = 0 \Rightarrow \quad (3)$$

$$\Rightarrow U_{ak} = \frac{2 \cdot Q_1}{4 \cdot \pi \cdot \epsilon \cdot r_{ecc} \cdot \left(1 + \frac{r_{ecc}}{d_{sur}}\right)} + \frac{Q_2}{4 \cdot \pi \cdot \epsilon \cdot r_0 \cdot \left(1 + \frac{r_0}{d_{sur}}\right)}$$

if there are both the primary and the secondary electron emissions, else Q_2 is zero.

If the electric field intensity, causing only the primary electron emission when weak, is strong enough to accelerate the electrons to ionize the gas molecules near the cathode, the secondary electron emission from the cathode arises by the gas ions hitting it. So far, a voltage drop over the narrow gap of $\lambda \cdot N_\lambda$ (an average electron free path multiplied by a natural number, explained later on) around the cathode, but not necessarily the whole around, with no secondary electron emission present is equal to the must-be value needed for gas molecule ionization. By meeting this condition, the secondary electron emission begins and the electric field intensity is being increased by the electric charge Q_2 , which causes both primary and secondary emissions increasing. With the phenomenon of the secondary electron emission, corona is associated burning near the cathode. The electric charge Q_2 increases until the electric breakdown takes place. Beyond the point of the electric breakdown the presented mathematical model is not valid any more.

The electric charges Q_1 and Q_2 depend on the increasing anode-cathode voltage U_{ak} and infinite set of kinet-

ic energy values around the cathode sphere obtained by electron while moving from the cathode surface, determined by the radii values r_{surk} up to the distance of

$$\left(r_{surk} + \frac{dr_{surk}}{dr_0} \cdot \lambda \cdot N_\lambda \right),$$

in the electric field of $\vec{E}(r, \varphi, Q_1, Q_2 = 0)$ as there is only the primary electron emission. The parameter N_λ is natural number telling at which distance from the cathode the collision phenomenon begins: up to $1 \cdot \lambda$ there is no collisions, in the interval from $1 \cdot \lambda$ inclusive and up to $2 \cdot \lambda$ there are the first collisions. So far, this parameter is taken as $N_\lambda = 2$ in this discussion. On the other hand this number also defines an interruption in the ionization process carried out by consecutive collisions process: the continuous ionization process is interrupted if only every N_λ -th collision causes the molecule (atom) ionization – every second collision in particular case of choice in presented model. On the basis of these pre-suppositions used in the model, the charges Q_1 and Q_2 are determined.

The electric field intensity is derived from the electric potential function $U(r, \varphi)$ by using the Hamilton operator:

$$\vec{E} = -\nabla \cdot U(r, \varphi) = -\text{grad}(U(r, \varphi)) = -\left(\hat{1}_r \cdot \frac{dU(r, \varphi)}{dr} + \hat{1}_\varphi \cdot \frac{dU(r, \varphi)}{r \cdot d\varphi} \right) \quad (4).$$

The eccentric radius r_{ecc} as it is defined in Fig. 2, is established by finding the closest equipotential surface to the sphere with the radius r_0 , which is its geometric radius. The equipotential surface is not exactly the sphere but is near enough not to cause any significant error. Establishing the eccentric radius r_{ecc} as it is defined in Fig. 2, the iterative procedure is used, based on similarity to the mathematic inversion of one point charge on the sphere with the radius of r_0 , known as Kelvin's transformation also, while a coefficient K_{eq} is determined to find the best approximated equivalent substituting two equal metallized and charged spheres (the anode and the cathode) with two eccentric points of opposite electric charge Q_1 inside these spheres:

$$r_{ecc} = \frac{d_{sur}}{2} \cdot \left(\sqrt{1 + 4 \cdot \frac{r_0}{d_{sur}}} - 1 \right) \cdot K_{eq} \quad (5)$$

at the charge Q_2 being zero [2]. So far, the equipotential surface of zero potential fits the cathode sphere better than 2.06 % with 95 % statistical confidence when the input data are $r_0 = 0.5$ mm and $d_{sur} = 1$ mm, but the zero cathode potential uncertainty is 1.16 % of the anode voltage by three iterations and with 95% statistical confidence.

When calculating the mean free path of electrons, quite large uncertainty is associated to this calculation. To demonstrate quite large deviations from the mean value some probability distributions are considered, and further on molecule radii discussed. The average velocity of an accelerated electron is calculated due to its exponential probability distribution and due to the final velocity value of the electron accelerated movement. The average velocity of an air gas molecule (O_2 or N_2) is established due to the Maxwell – Boltzman probability distribution. Further on, the average free path of the electron up to collision with the gas molecule due to its exponential probability distribution is derived as its expectation value and is [5]:

$$\lambda = \frac{R \cdot T}{\sqrt{1 + \frac{v_{m_avg}^2}{v_{e_avg}^2}} \cdot \pi \cdot d^2 \cdot N_A \cdot p} \quad (6)$$

where the quantity d is the sum of molecule and electron radii, defined as a collision diameter:

$$d = r_m + r_e \quad (7)$$

R is the gas constant, p and T are gas pressure and temperature, and v_{m_avg} and v_{e_avg} are average velocities of molecules and electrons respectively.

A covalent radius is the nominal radius of the atoms of an element when covalently bound to other atoms, as deduced through the separation between the atomic nuclei in molecules. In principle, the distance between two atoms that are bound to each other in a molecule (the length of that covalent bond) should equal the sum of their covalent radii. In the previous papers [2] the oxygen atom covalent radius of 68 pm was taken into account [6] and hence the molecule radius of 133.4 pm, and so far, the relevant value of the electron kinetic energy was estimated rather too low, which caused breakdown voltage values being estimated very high. Using Van der Waals radii would result in still lower values of the electron energy and higher breakdown voltage estimates. Therefore the empirical covalent radii (oxygen: 60.4 pm, nitrogen: 54.9 pm), the relevant covalent bond lengths of diatomic molecules (oxygen: 121.0 pm, nitrogen: 110.0 pm) are used afterwards [7, 8]. The molecule of diatomic gases is approximated as a rod with rounded ends and the collision area is obtained by this rod projection in the direction of the electron movement using the mean value of the collision area due to the molecule rotation. The molecule collision radii (oxygen: 81.3 pm, nitrogen: 73.9 pm) are calculated due to the mean value of the collision area. Since in the vicinity of less than $\lambda \cdot N_A$ to the cathode there is no impacts of electrons, the average kinetic en-

ergy of the electron travelling along the average free path is taken into account at the radii of

$$r > r_{surk} + \frac{dr_{surk}}{dr_0} \cdot \lambda \cdot N_A \text{ with } N_A = 2 \text{ in the presented model:}$$

$$W_{ek} = e \cdot E(r, \varphi) \cdot \lambda \quad (8)$$

whilst the electric field intensity and the average free path are collinear vectors.

When the electron collided with the gas molecule, its kinetic energy from Eq. (8) and the initial electron kinetic energy carried on from the previous collision W_{car_on} are together transferred to the molecule by impact as exciting energy of the molecule:

$$W_{exm} = W_{ek} + W_{car_on} \quad (9)$$

In this discourse the term of excitation, and hence the exciting energy, is used, according to some scientific terminology, in the unconventional way. The excitation as a general term is an elevation in energy level above an arbitrary baseline energy state of an atom or a molecule without causing any changes in its charge on the whole (ionization, electron attachment) or any chemical changes (molecule dissociation). But hereafter, the excitation, and hence exciting energy, means firstly an increase in energy level up to the levels of ionization and dissociation, if applicable, secondly their accomplishment, and thirdly causing the changes in energy of newly begotten particles – the elevation in energy level with ions or dissociated atoms, or changes in kinetic energy of free electrons, if there are any involved in the excitation process. Namely, the excitation is not obtained by the electron collisions only, but also by photon impacts and through a displacement current effect. But, the outcoming excited particles are considered to have a short lifetime, and afterwards produce the photon, which further on cause the excitation of another atom or molecule. So far, we will not deal with the changes in energy level of outcoming particles (ions, dissociated atoms), but the part of the exciting energy beyond the ionization or the dissociation energy is attributed to the involved electrons, if it is applicable, but otherwise to the photons with the same end effect, as in the case of the involved electrons, but with the mass equals to zero. In both cases this energy is carry-on energy.

Due to the function of the electric field intensity depending on the radius there are three ranges between the electrodes: a highly ionized range, a partly ionized range and a non-ionized range – Fig. 4.

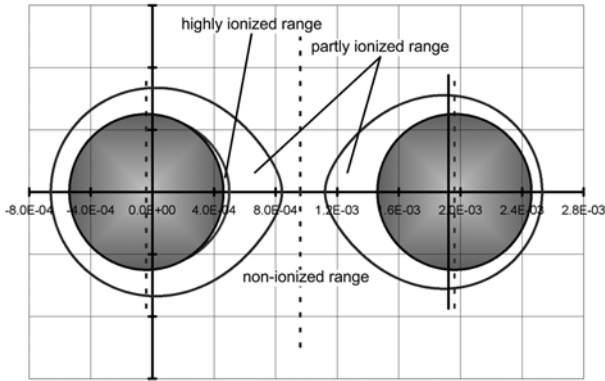


Figure 4: The ranges due to ionization degrees of nitrogen (N) in the midst of the air medium in the electric field – the ionization degrees refer to nitrogen atoms only.

The **highly ionized range** is in the vicinity of the each electrode because nearly every collision causes such exciting energy in the molecule that its ionization occurs due to very high kinetic energy of the electrons, and in the one of the next moments the ionization is followed by the recombination. From the viewpoint of kinetic energy of colliding particles before and after an inelastic collision, the kinetic energy lost by the collision is mainly consumed by some other process – in discussed case as the ionization energy, and further on as the dissociation energy, whereas the kinetic energy before the collision is the exciting energy being stored as the kinetic energy of an electron. Taking into account this loss defined by the difference ($W_{before} - W_{after}$), a fraction of the kinetic energy loss is introduced as

$$\frac{W_{before} - W_{after}}{W_{before}} = \frac{W_{icon}}{W_{exm}} = \left(\frac{m_m}{m_e + m_m} \right)$$

at a total inelastic collision, and so the exciting energy of the molecule must be at least [9]:

$$W_{exm} \geq W_{ion} \cdot \left(1 + \frac{m_e}{m_m} \right) \tag{10}$$

to cause ionization. The exciting energy of the whole amount of moving electrons with their kinetic energy, is divided between the ionization as the P_i part and the recombination as the $(1-P_i)$ part.

After the **ionization collision**, the average carry-on kinetic energy per electron, carried on by the one colliding and by the one emitted is:

$$W_{car_on} = \frac{W_{exm} - W_{icon} \cdot \left(1 + \frac{m_e}{m_m} \right)}{2} \cdot P_i \tag{11}$$

After the **recombination collision**, since the collision is totally inelastic, and it consumes the whole exciting energy received by the electron, and further on, one part of recombined molecule energy ΔW_{rec} is emitted (for instance as emitted radiation energy, where the photon is energy carrier) and further consumed by ionizing molecules in continuous process:

$$\Delta W_{rec} = W_{icon} \cdot (1 - P_i) \tag{12}$$

but the other part is transformed to thermal energy, which K -part is conveyed to surroundings by thermal conduction, convection and/or radiation, but $(1-K)$ -part of it causes the molecule temperature rise above the ambient temperature for the increment:

$$\Delta T = \frac{2 \cdot (W_{exm} - W_{icon})}{3 \cdot k} \cdot (1 - P_i) \cdot (1 - K) \tag{13}$$

So far the average temperature of the gas in the neighbourhood of the cathode and the anode rises and the temperature of the each electrode increases too when the molecules bump at it. The parameter $K=99.8\%$ in Eq. (13) defines the percentage of the energy in this equation, conveyed and conducted to the cathode, the anode, and further on, to the ambient by a natural or a forced cooling. Due to the temperature increment of Eq. (13), the average kinetic energy of the gas molecules increases, and hence the average molecule velocity.

Next to this range, the **partly ionized range** exists up to the point where no ionization occurs. In this range, besides the ionization collisions, the **dissociation collisions** are happening with the exciting energy of the molecule equal to:

$$W_{icon} \cdot \left(1 + \frac{m_e}{m_m} \right) > W_{exm} \geq W_{diss} \cdot \left(1 + \frac{m_e}{m_m} \right) \tag{14}$$

In this case, the exciting energy of the gas molecule causes the **dissociation** of the two-atom molecule into two gas atoms. This collision is partly inelastic and it consumes the dissociation energy. The remaining kinetic energy of the colliding electron is carried on by the same electron:

$$W_{car_on} = W_{exm} - W_{diss} \cdot \left(1 + \frac{m_e}{m_m} \right) \tag{15}$$

and further on, it increases because the electron passes the next average free path before the next collision – Eq. (8).

Towards the gap centre, the **non-ionized range** begins, where the dissociation collisions and also the **unaffected collisions** are present. If the exciting energy of the

molecule is lower than the dissociation energy of the gas molecule:

$$W_{diss} \cdot \left(1 + \frac{m_e}{m_m} \right) > W_{exm} \quad (16),$$

the colliding electron has no effect on the gas molecule. The kinetic energy of the electron after the collision is the same as before, which is:

$$W_{car_on} = W_{exm} \quad (17).$$

Although there is a sequence of all mentioned phenomena, we could not consider there are any pure ranges such as an ionization-recombination, a dissociation or an unaffected range.

Knowing the electric field intensity at the cathode surface at $\varphi = 0$ and its temperature, the following conductive current densities are calculated: the current density of the field emission and the current density of the thermionic emission. Both of them are the active current densities.

If an alternating electric field is applied, as in this particular case caused by a sinusoid of the anodecathode voltage with the amplitude of 20 kV and the frequency 5 kHz being interrupted by the breakdown after achieving the throughout ionization voltage, the displacement current occurs. The displacement current is defined by its density [4], and the latter is, likewise the electric field intensity, depending on time, therefore both of them can be represented by phasors in complex plane. An angle δ between the displacement current density phasor and the phasor of time-derivative of the electric field intensity is defined by the complex value of the relative permittivity. The displacement current density is vector, collinear to the time-derivative of the electric field intensity vector multiplied by absolute value of relative permittivity ϵ_r and the permittivity ϵ_0 of vacuum, and hence collinear to the electric field intensity vector. The relative permittivity is complex scalar constant defined by its absolute value and by losses angle δ , where the dielectric losses of the gas are defined as the imaginary part of the complex value of the relative permittivity, so they are associated with sinus function of the losses angle. The active displacement current causes the excitation of the molecules and the phasor of this current density is in phase with the electric field intensity phasor in the complex plane. The reactive displacement current vector is a capacitive current, so far, its phasor is perpendicular to the electric field intensity phasor, but the relevant vectors are collinear. Because the active displacement current causes the excitation of the molecule in the volume between the cathode and the anode, the ac-

tive displacement power is the integral of the product of the phasors of the active displacement current and of the electric field intensity throughout the volume relevant to one molecule that is the gas molecule itself and in the hollow volume around it, which is

$\frac{V_{mol}(p, T)}{N_A}$ (a volume of one mol divided by the Avogadro number), under the relevant thermodynamic conditions of the gas. Further on, the active displacement energy of one molecule is defined by:

$$W_{Dact} \approx \epsilon_r \cdot \epsilon_0 \cdot \frac{dE(r, \varphi, t)}{dt} \cdot E(r, \varphi, t) \cdot \frac{V_{mol}}{N_A} \cdot \frac{\lambda}{v_{e_avg}} \cdot \sin \delta \quad (18).$$

The losses angle δ is defined by the ratio of the volume of one molecule V_m and its relevant part of empty space belonging to it:

$$\tan \delta = \frac{1}{\frac{V_{mol}(p, T)}{V_m \cdot N_A} - 1} \quad (19).$$

The mathematical model of the electric discharge in gases has to take into account both, the kinetic energy of the electrons, the energy of photons and the energy of the displacement current. The electron kinetic energy is partly transferred to the gas molecule by the electron impact, and causes the ionization or the dissociation, discussed heretofore. In this case, the ionization is considered as the impact ionization although it is more probable that the ionization is done through the excitation of the gas molecule on its higher energy level [5]. The dissociation of the two-atom molecule just cannot be carried out directly by the electron impact due to the large difference of the electron mass and the dissociated atom mass. The dissociation is completed by the exciting energy of the two-atom molecule due to the impact energy when raised in such extend that the dissociation energy level is achieved. This is the dissociation due to the conductive and the convective current. The displacement current energy also affects the gas molecules, and also causes their ionization and their dissociation. Because it has no carriers, the ionization and the dissociation are caused by the excitation of the gas molecule with no impact, but only due to the displacement current. All these processes: the impact ionization, the dissociation – both due to the conductive and the convective current, the ionization and the dissociation – due to the displacement current, have the same mechanism of being completed – raising the molecule energy on its higher energy level, and afterwards the accomplishment of the process. Therefore the kinetic energy and the displacement energy

Eq. (18) are summarized in the exciting energy of the gas molecule, which is the active energy:

$$W_{exm}(r, \varphi, t, p, T, W_{ion}, W_{diss}, m_m) = e \cdot E(r, \varphi, t) \cdot \lambda(p, T) + \quad (20),$$

$$+ W_{car_on} \left(W_{ion} \cdot \left(1 + \frac{m_e \mathbf{v} \cdot \mathbf{0}}{m_m} \right), W_{diss} \cdot \left(1 + \frac{m_e \mathbf{v} \cdot \mathbf{0}}{m_m} \right) \right) +$$

$$+ \varepsilon_r \cdot \varepsilon_0 \cdot \frac{dE(r, \varphi, t)}{dt} \cdot E(r, \varphi, t) \cdot \frac{V_{mol}(p, T)}{N_A} \cdot \frac{\lambda(p, T)}{v_{e_avg}} \cdot \sin \delta$$

where the mass of the impacting particle has the value of m_e if it is an electron, or has the value of zero if it is a photon.

Due to carry-on energy the exciting energy of the gas molecule has its minimal value and its maximal value, as follows:

$$W_{exm_mn}(r, \varphi, t, p, T, m_m) =$$

$$= e \cdot E(r, \varphi, t) \cdot \lambda(p, T) + \quad (21),$$

$$+ \varepsilon_r \cdot \varepsilon_0 \cdot \frac{dE(r, \varphi, t)}{dt} \cdot E(r, \varphi, t) \cdot \frac{V_{mol}(p, T)}{N_A} \cdot \frac{\lambda(p, T)}{v_{e_avg}} \cdot \sin \delta$$

$$W_{exm_mx}(r, \varphi, t, p, T, W_{ion}, W_{diss}, m_m) = \quad (22).$$

$$= e \cdot E(r, \varphi, t) \cdot \lambda(p, T) +$$

$$+ (W_{ion} - W_{diss}) \cdot \left(1 + \frac{m_e}{m_m} \right) +$$

$$+ \varepsilon_r \cdot \varepsilon_0 \cdot \frac{dE(r, \varphi, t)}{dt} \cdot E(r, \varphi, t) \cdot \frac{V_{mol}(p, T)}{N_A} \cdot \frac{\lambda(p, T)}{v_{e_avg}} \cdot \sin \delta$$

The minimal value is very obvious, but the maximal value is numerically determined by the mathematical model. The exciting energy values, at the one and the same point (r, φ) , are lying between these two values concerning the carry-on energy probability distribution, which is the square probability distribution. The probability distributions of the other quantities in Eq. (20) would contribute their shares to the exciting energy probability on the whole, but it is reasonable that these other contributions are considered as a part of uncertainty calculation.

With this phenomenon especial curves and surfaces are defined, which are equi-exciting energy curves and surfaces. The **equi-exciting energy line (or surface)** in the electric field within the medium of the particular gas is the set of points at which the gas molecules are exposed to the same exciting energy at the same exciting energy probability:

$$C_{eqex} = \{ T_i(r, \varphi) \Leftarrow W_{exm}(r, \varphi, t, p, T, W_{ion}, W_{diss}, m_m) = \quad (23).$$

$$= constant \wedge P_{Wexm} = constant \}$$

For various constants the family of the curves (surfaces) is achieved. Among these curves (surfaces), corresponding to Eq. (23) there is one most important, and it is a border curve between the ionized range and the non-ionized range in Fig. 4, and further on also in Fig. 10, considering at least some ionization is carried out by photons:

$$C_{eqex_ion} = \{ T_i(r, \varphi) \Leftarrow \quad (24).$$

$$\Leftarrow W_{exm_mx}(r, \varphi, t, p, T, W_{ion}, W_{diss}, m_m) = W_{ion} \}$$

So far, the **ionization border line (or surface)** is a particular equi-exciting energy line (surface) within the particular gas distinguishing between the area (space) of the ionized gas on one side of this curve and the area (space) on the other side of the curve predominately occupied by its neutral molecules and atoms (also dissociated if relevant) with no ionized particles. The whole exciting energy probability distribution domain is below the value of the ionization energy of the gas molecule, and the ionization occurs just at the upper domain border, hence the probability that the exciting energy is lower than the ionization energy of the particular gas is one ($P_{Wexm} = 1$) in the non-ionized range in Fig. 4:

$$R_{non_ion} = \{ T_i(r, \varphi) \Leftarrow \quad (25).$$

$$\Leftarrow W_{exm_mx}(r, \varphi, t, p, T, W_{ion}, W_{diss}, m_m) < W_{ion} \}$$

The ionization border line is an outer contour of both the highly and the partly ionized ranges in Fig. 4.

If the anode-cathode voltage increases, the non-ionized range in Fig. 4 narrows, and the partly ionized range from the cathode side touches the partly ionized range from the anode side, and the ionized path between the electrodes arises throughout the gas gap, the dielectric breakdown occurs and the electric discharge arc takes place.

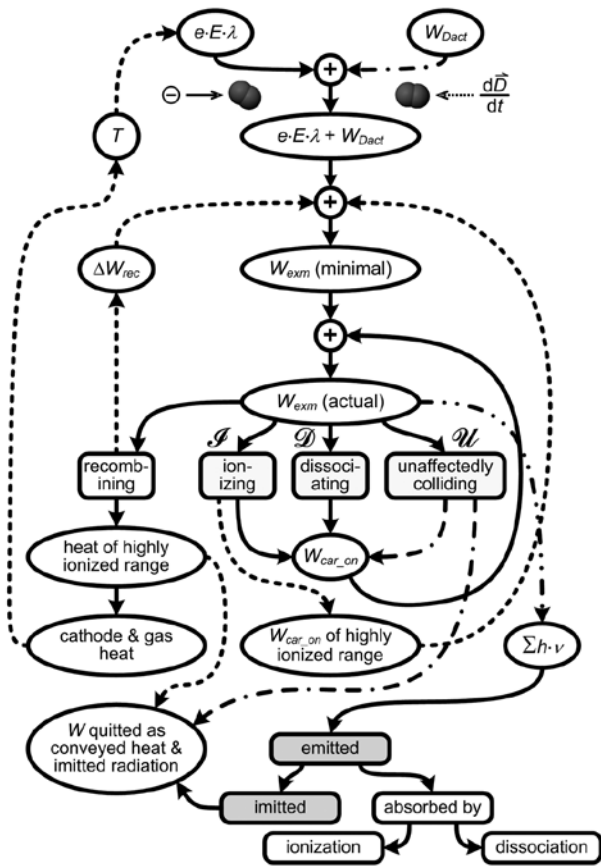


Figure 5: The physics of arising the discharging arc in the two-atom molecule gas.

Hereafter, the mathematical algorithm, describing the phenomenon of arising the discharging arc in the stage of building the ionized path through gas gap up to a throughout ionization, was computerised to get a dynamic model of this phenomenon as shown in Fig. 5.

There are three kinds of electric current density, beginning with the one already discussed:

- the displacement current density, as discussed;
- the conductive current density, which is in phase with electric field intensity, appears in consequence of the cold electron emission, due to the electric field effect, and due to the thermionic electron emission, whose relevant current density is, to the large degree, independent on time, but time-dependent part is in phase with the electric field intensity;
- the convective current is Laplacian of the electric potential $U(r, \varphi, t)$, which is direct or alternating quantity; since the Laplacian is zero in the state before the electric breakdown, the convective current is zero too.

The total cathode current is achieved by integration of the vector sum of all contributing current densities over

the cathode surface in spherical coordinates (r, φ, ϕ) taking into account the rotary symmetry of the electric field and system geometry:

$$I_k = 2 \cdot \int_{\phi=0}^{\phi=\pi} \int_{\varphi=0}^{\varphi=\pi} \left| \vec{j}_D \left(\frac{d\vec{E}}{dt} \right) + (j_E(|\vec{E}|) + j_T(T_k, |\vec{E}|)) \right| \cdot \frac{\vec{E}(r, \varphi, t)}{|\vec{E}(r, \varphi, t)|} + \vec{j}_{conv}(\vec{E}) \cdot r^2_{surk}(\varphi) \cdot d\varphi \cdot \sin \phi \cdot d\phi \quad (26)$$

having in mind the quantities depended on the electric field intensity depends indirectly on (r, φ) and time, and moreover each of them depends on the cathode temperature.

The shortest field line between the spherical electrodes of the opposite charges is the shortest surface-to-surface distance between the spheres. In this case the angle φ is zero. The vector of electric field intensity has only radial component since the angular component is zero. Hereafter the mathematical model deals with the electric field and the phenomena associated with it in this particular direction. Therefore, the radial coordinate in this direction $\varphi = 0$ is named as r_x – radius in the x -direction of the (r, φ) plane.

When discussing the electrical breaking contact, its contact members are the electrodes. The distance between them increases from zero, when the breaking contact still holds the closed position, up to the maximum value. In the model, the distance of 1 mm is used because the Paschen law minimum is being avoided.

3. The chemism the gas throughout ionization

The whole kinetics of the discharging arc formation, and hence of the throughout ionization of a gas mixture medium, continuing to the electric breakdown, and further on, followed by the discharging arc ignition in that medium, consists of its physics, discussed heretofore, and its chemism – the chemism of the discharging arc formation in any gas mixture as well as in any two-atom molecule gas even of chemical single-element. In the process of the gas medium ionization, each of the gases is ionized and afterwards ions are recombined, and multi-atoms molecules are dissociated and later their atoms associate in another molecules, all happening fluently and continuously forming the ionized ranges ending finally in the throughout ionization of the gas in the gap between electrodes if only the electric field in the gap is sufficient for it. And this part of the kinetics of the throughout ionization formation, which consequently leads to the electric breakdown and to the discharging arcs ignition, is the chemism of this phenomenon. When dealing with air as a gas me-

dium, all constituents must be taken into account: oxygen, nitrogen, argon, carbon dioxide etc. In this paper, only oxygen and nitrogen, as major constituents of air, are considered when modelling the throughout ionization of the air gap.

In the case of the O_2 - O - O_3 gas mixture, as well as in the case of the N_2 - N - NO_2 gas mixture, there are three kinds of gas and its ions in each mixture, and hence the physics of the processes are defined in the following way:

- the ionization by the set of the transfer functions $I = \{f_{ion}, g_{ion}, h_{ion}\}$ for each gas in the mixture respectively;
- the dissociation by the set of the transfer functions $D = \{f_{dis}, g_{dis}, h_{dis}\}$ for each gas in the mixture respectively;
- the unaffected collisions by the set of the transfer functions $U = \{f_{unaff}, g_{unaff}, h_{unaff}\}$ for each gas in the mixture respectively.

The sum of the f -functions is one whenever and wherever in the space, and likewise the sum of the g -functions and the sum of the h -functions for each kind of compounds: the oxygen and the nitrogen compounds separately, and these sets are also different for each of them. The chemical process of the oxygen compounds mixture is shown in Fig. 6, but the chemical process of the nitrogen compounds mixture in Fig. 8, both followed by the relevant results and discussion.

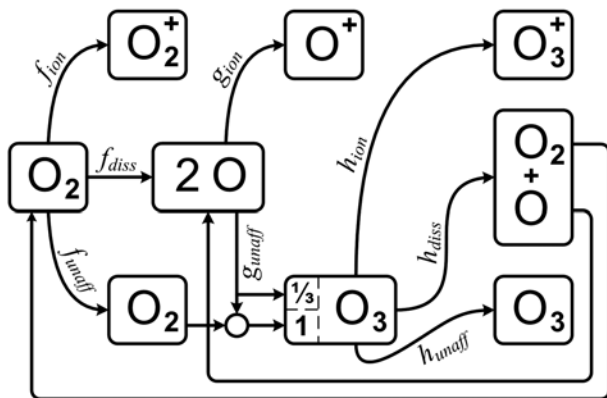


Figure 6: The chemical process of oxygen compounds in the electric field.

Yields of the outgoing gases along the shortest path between the cathode and the anode are presented graphically in Fig. 7 in the moment of the throughout ionization of O_3 molecules, which is the end of the discharging arc formation in the air followed by the electric breakdown and by the discharging arc itself.

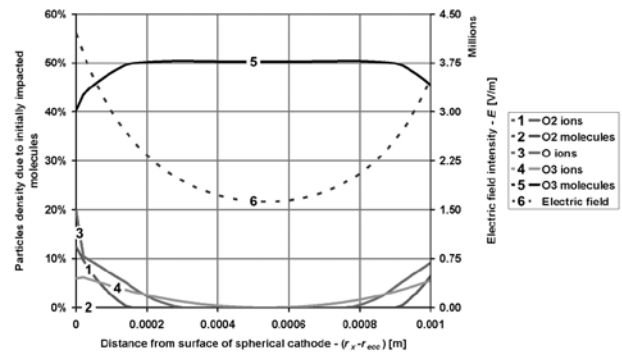


Figure 7: The yields of the chemical process of oxygen compounds of the air in the electric field along the shortest path between the electrodes.

The ratios between the oxygen compound particles densities, which are the output of the chemical process, and the initially impacted oxygen molecules density, which is the input of the chemical process, are the yields of the chemical process output, indexed as in Fig. 7, are as follows: $y_1(O_2 \rightarrow O_2^+)$, $y_2(O_2 \rightarrow O_2)$, $y_3(O_2 \rightarrow O^+)$, $y_4(O_2 \rightarrow O_3^+)$ and $y_5(O_2 \rightarrow O_3)$. The chemical process produces the mixture of the oxygen compound particles, which maintains its structure ratios despite its continuous kinesis: ionizing, recombining, dissociating and associating the molecules, the atoms and the ions respectively, whatever is appropriate for each kind of particle, within its steady state structure.

The model of the chemism of the discharging arc formation in oxygen presumes that the whole amount of the O atoms, after the O_2 molecules dissociation, is combined to ozone in one or another way. These atoms are primarily associated to the unaffected O_2 molecules, but there can be some leftover amounts either of the O atoms or the O_2 molecules. If there are the O atoms leftover, they are combined with themselves to form ozone. On the other hand, if there are the O_2 molecules leftover, they are outcome of the process by the yield of y_2 as unaffected and not combined to ozone, which is shown in Fig. 7 as the result of this (and only this) particular case, which is zero throughout the gap.

The chemical process with the O_2 - O - O_3 gas mixture is the same from the standpoint of oxygen compounds structure whether there is pure oxygen involved in it or there is some other gas in the mixture as the nitrogen in the air. But, it is not the same with nitrogen since the chemical process of the pure nitrogen in the electric field gives the N_2 -N mixture including their ions, but the chemical process of nitrogen in the air produces the N_2 -N- NO_2 mixture including their ions and dissociated particles. Hereafter the N_2 -N- NO_2 mixture is dealt with. It is presumed that there are no volatile organic compounds in the standardized (unpolluted) atmosphere, and hence

the dissociation of NO_2 is defined as $\text{NO}_2 \rightarrow \text{NO} + \text{O}$, and further oxygen atom reacts with O_2 molecule from the air $\text{O}_2 + \text{O} \rightarrow \text{O}_3$ and produced ozone, and once again oxidizes nitrogen monoxide $\text{NO} + \text{O}_3 \rightarrow \text{NO}_2 + \text{O}_2$ returning the O_2 molecule into the air, so effectually the O_2 molecules do not need to be exchanged from and into the air, but is produced and consumed inside the chemical sub-process following the dissociation of the NO_2 molecules – Fig. 8. The NO_2 molecules, which resulted from this sub-process, undergo the electric field and are ionized, dissociated or unaffected.

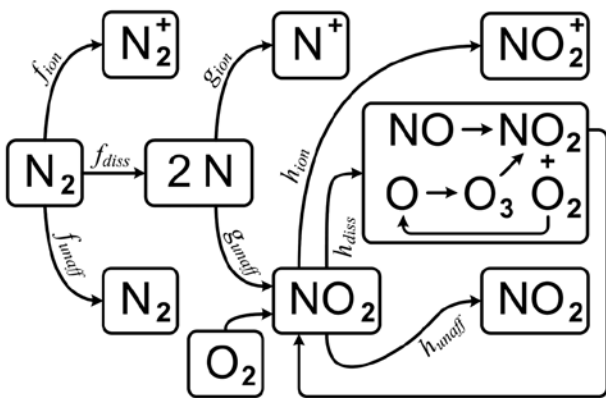


Figure 8: The chemical process of nitrogen compounds of the air in the electric field.

As in the previous case, the yields of the outgoing nitrogen gases along the shortest path between the cathode and the anode are shown in Fig. 9 in the moment of the throughout ionization of O_3 molecules formation – see Fig. 10, which is followed by the electric breakdown in the air gap.

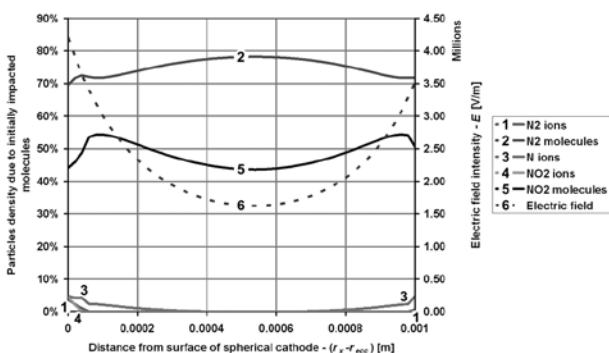


Figure 9: The yields of the chemical process of nitrogen compounds of the air in the electric field along the shortest path between the electrodes.

The ratios between the nitrogen compound particles densities, which are the output of the chemical process, and the initially impacted nitrogen molecules den-

sity, which is the input of the chemical process, are the yields of the chemical process output, indexed as in Fig. 9, are as follows: $y_1(\text{N}_2 \rightarrow \text{N}_2^+)$, $y_2(\text{N}_2 \rightarrow \text{N}_2)$, $y_3(\text{N}_2 \rightarrow \text{N}^+)$, $y_4(\text{N}_2 \rightarrow \text{NO}_2^+)$ and $y_5(\text{N}_2 \rightarrow \text{NO}_2)$.

Because the discharging arc formation depends on the throughout ionization formation, during whose process the ionized ranges of each constituent gas is being formed as a part of its kinetics, the whole mixture kinetics is influenced by each gas in the mixture, although the chemical process of the particular constituent does not depend on the other gases in the mixture. The chemical process of the O_2 - O - O_3 gas mixture in the electric field, and so far its chemism of the throughout ionization formation in this mixture, is unchanging whether it involves pure oxygen or the air. Nevertheless, the kinetics of the throughout ionization formation, and hence of the discharging arc ignition, is influenced by the particles of the other constituents of the air through its physics. Namely, the other constituents particles, as nitrogen compounds particles, are intercepting the electrons, and so reducing the electron collisions to oxygen particles, and beside that they are forming their own ionized ranges, which contribute their part to the ionized ranges growth, and so far to the throughout ionization formation. The N_2 - N - NO_2 gas mixture is also influenced by the other air constituents through its physics, hence the kinetics of the throughout ionization formation is based on an equilibrium between all air constituents in every stage of the ionized ranges growth. The kinetics, weather dealt separately as the O_2 - O - O_3 mixture and the N_2 - N - NO_2 mixture or together as the air, is qualitatively the same, but it is quantitatively different in the transfer functions, pondered by mixing ratio of oxygen (cca 20%) and nitrogen (cca 80%) in the air as modelled through physics, and hence in yield functions of chemism, and further on in concentrations and in the ionized ranges growth until the one of the constituent gases is throughout ionized – Fig. 10.

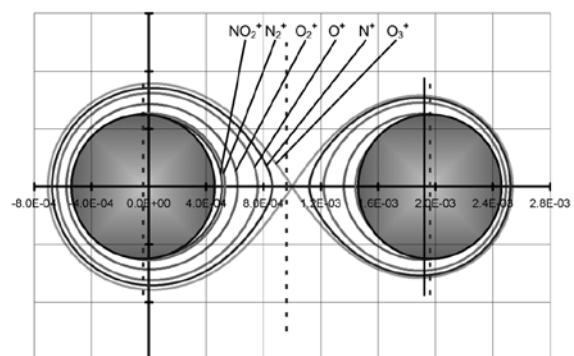


Figure 10: The ionization border lines C_{eqex_ion} as the axial cross-section of the ionization border surfaces for the main constituents of the air just when the throughout ionized path is formed by ozone ions.

In this figure, there are the ionization border lines C_{eqex_ion} representing the ionization border surfaces, as the geometric bodies of the electrodes are rotary symmetrical, for each kind of the constituent ions in the air, where the throughout ionization is achieved by ozone ions. These lines are not the Cassini ovals. The ionization border lines (surfaces) C_{eqex_ion} defined by Eq. (24), circumscribe the ionized range, which consist of the highly ionized and the partly ionized range in Fig. (4), and is complementary to the non-ionized ranges in Eq. (24):

$$R_{ion} = \bar{R}_{non_ion} = \{ T_i(r, \varphi) \leftarrow W_{exm_mx}(r, \varphi, t, p, T, W_{ion}, W_{diss}, m_m) \geq W_{ion} \}$$

for each kind of constituent ions.

If the ionized range of Eq. (27) or the union of all ionized ranges, since the air is gas mixture, includes at least one subset of points that is continuous between any point on the cathode and any point on the anode, the throughout ionization is established. Hereby, any subset of the ionized range or of their union that is continuous between any point on the cathode and any point on the anode is the throughout ionized path, and the discharging arc is formed by the electric breakdown along one of the throughout ionized paths. A voltage over the cathode-anode gap, at which the throughout ionization is established, is the throughout ionization voltage, and a relevant current is the throughout ionization current. If there is no throughout ionized path, the non-ionized gap exists with its distance between the relevant ionized ranges around the cathode and the anode, which is the infimum of the distances between any two of their respective points. The non-ionized gap can be stated due to the whole gas mixture (i.e. air) or separately due to the particular constituent gas – Tab. 2.

Table 2: The characteristic parameters at the throughout ionization of the air gap.

| | unit | Σ air | O ₂ ⁺ | O ⁺ | O ₃ ⁺ | O ₃ | N ₂ ⁺ | N ⁺ | NO ₂ ⁺ | NO ₂ |
|-------------------------------|--------------------|--------------|-----------------------------|----------------|-----------------------------|----------------|-----------------------------|----------------|------------------------------|-----------------|
| throughout ionization voltage | kV | 2.23 | ← | ← | ← | ← | ← | ← | ← | ← |
| throughout ionization current | μA | 26.6 | ← | ← | ← | ← | ← | ← | ← | ← |
| non-ionized gap | mm | 0 | 0.76 | 0.48 | 0 | - | 0.92 | 0.26 | 0.98 | - |
| ratio of impacted particles | % | - | 0.23 | 0.54 | 0.41 | 9.9 | 0.12 | 0.79 | 0.10 | 39 |
| concentration in air | ×10 ⁻¹⁸ | - | 0.40 | 0.93 | 0.71 | 17 | 0.14 | 0.93 | 0.12 | 45 |

The gas medium in the gap, if not noble gas, becomes chemically active under the sufficient electric field intensity in this gap, mostly producing new gaseous

compounds that are more vulnerable to ionization, and hence the mixture throughout ionization voltage is lowering, as well as its breakdown voltage. If the gas medium is the air, the electric field intensity can cause its pollution, since the ozone and the nitrogen dioxide are forming. Certainly, every formation of these two compounds does not mean the real pollution, and so far, in this particular case air quality indices [10] are zero and the category of the air is good.

4. Conclusions

Although the paper deals with the discharging arc ignition and especially the phenomena in early stage of the ionized path building up to the throughout ionized path establishment quite scholastically, it gives some understanding of physical and chemical processes carried on in the narrow gap of the gas mixture in the presence of the non-homogeneous electric field due to the primary and the secondary electron emission, and further on, due to the chemical changes in the gas mixture structure. So far, the arc avoiding and the arc extinguishing methods are clarified on the basis of the mathematical models of the drawn arc formation [1], and of the discharging arc formation model. On the basis of the discharging arc formation model some scientific conclusions and quantitatively evaluated results are obtained as stated in the following highlights:

- the kinetics of the processes in the gas medium between two electrodes shows that the discharging arcs in their ignition stage are not significantly determined by the contact materials and their arc forming affinity [1], except for the secondary emission, which hastens the throughout ionized path formation and hence discharging arc ignition,
- the discharging arc ignition strongly depends on physical and chemical properties and reactions of gas mixture medium, and especially chemical reactions increase the ionized path growth;
- so far, the methods to avoid discharging arcs are not based on the proper choice of contact materials with the low affinity to form arcs, but the avoiding and extinguishing is performed by specially designed arc quenching electric circuits, minimizing the transient voltages over the gap of electric contacts during their manoeuvres;
- the discharging arcs are diminished by applying parallel capacitance to inductive loads or to the electric contacts in d.c. electric circuits to minimize the displacement current and the peak value of the overvoltage;
- the discharging arcs are avoided by using inert gas medium and/or low gas pressure and even vacuum in sealed electric contacts;

- the discharging arc are extinguished by lengthening the throughout ionized path for instance by the application of magnetic field perpendicular to the electric field lines in the contact gap, and hence producing force on the flowing electrons;
- further on, in cases of some severe electric fields, as in the surroundings of EHV (extra high voltage) power lines, the discharge arc formation model, applied to appropriate geometrical and electrical parameters associated with the electrodes and the environment, gives the quantitative estimation method of ozone and nitrogen dioxide pollution in the air.

Arrived: 30. 05. 2011

Accepted: 26. 1. 2012

References

- 1 PAVLOVČIČ, France, NASTRAN, Janez. Affinity of contact materials to form the electric drawn arcs. Inf. MIDEM, sep. 2005, letn. 35, št. 3, str. 148-157.]
- 2 PAVLOVČIČ, France, NASTRAN, Janez. The arising of Electric Discharge Arcs. Inf. MIDEM, mar. 2008, letn. 38, št. 1, str. 42-52.
- 3 Gershman S.: Structure of Glow Discharge. http://science-education.pppl.gov/SummerInst/SGershman/Structure_of_Glow_Discharge.pdf, 11. 06. 2007.
- 4 Željeznov M.: Osnove teorije elektromagnetnega polja (Fundamentals of Electromagnetic Field Theory), Univerza v Ljubljani, Fakulteta za elektrotehniko, Ljubljana, 1971.
- 5 Sproull, R.L.: Modern Physics, second edition, John Wiley & Sons, Inc., New York – London, 1966.
- 6 Cambridge Structural Database of The Cambridge Crystallographic Data Centre, 12 Union Road, Cambridge, CB2 1EZ, UK, <http://www.ccdc.cam.ac.uk/products/csd/radii/>, 05.01.2010.
- 7 Slater J.C.: Atomic Radii in Crystals. Journal of Chemical Physics, Vol. 41, Issue 10, page 3199, doi:10.1063/1.1725697, (<http://dx.doi.org/10.1063%2F1.1725697>), Publisher: American Institute of Physics, Nov 15, 1964, [http://en.wikipedia.org/wiki/Atomic_radii_of_the_elements_\(data_page\)](http://en.wikipedia.org/wiki/Atomic_radii_of_the_elements_(data_page)), 06. 01. 2010.
- 8 Weast, R.C., ed., CRC Handbook of Chemistry and Physics, 62nd ed., Boca Raton, FL: CRC Press, 1981.
- 9 Yavorsky, B.; Detlaf, A.: Handbook of Physics, English translation, Mir publishers, Moscow, 1975.
- 10 Federal Register, Vol. 75, No. 26, Tuesday, February 9, 2010, Rules and regulations, Part III, Environmental Protection Agency, 40 CFR Parts 50 and 58, Primary National Ambient Air Quality Standards for Nitrogen Dioxide, Final Rule.

300 GHz microbolometer double-dipole antenna for focal-plane-array imaging

Leon Pavlovič, Janez Trontelj in Drago Kostevc*

University of Ljubljana, Faculty of Electrical Engineering, Ljubljana, Slovenia

Abstract: A room-temperature planar microbolometer double-dipole antenna for the focal-plane-array imaging at 300 GHz is presented. The fabricated antenna with a Titan bolometer consists of the full-wavelength parallel-dipole array on a thin nitride membrane, double impedance-transformation sections and low-pass-filter readout taps on a silicon substrate. The simulated antenna directivity at 300 GHz is about 11.7 dBi and agrees well with the measured radiation pattern. The radiation efficiency is about 85 % and the estimated bandwidth more than 200 GHz. A responsivity of 40 V/W and a noise-equivalent power of $4 \times 10^{-11} \text{ W}/\sqrt{\text{Hz}}$ have been measured, respectively.

Key words: millimeter, terahertz, microbolometer antennas, sensors, focal-plane arrays

300 GHz mikrobolometriška antena z dvojnimi dipolom za slikanje s poljem v goriščni ravnini

Izveček: Predstavljena je mikrobolometriška antena z dvojnimi dipolom za slikanje s poljem (senzorjev) v goriščni ravnini pri 300 GHz. Antena ima bolometer iz titana in sestoji iz celovalovnega dvojnega dipola, ki leži na tanki opni iz nitrida. Vsebuje še dvojno impedančno pretvorbo ter nizkopasovno sito z odcepnimi linijami na silicijevem substratu. Simulacijski rezultati, s smernostjo okoli 11,7 dBi, se dobro ujemajo z izmerjenimi smernimi diagrami. Sevalni izkoristek antene znaša okoli 85 %, ocenjena pasovna širina pa je približno 200 GHz. Izmerjena odzivnost je 40 V/W, ekvivalentna šumna moč (ang. »NEP«) pa $4 \times 10^{-11} \text{ W}/\sqrt{\text{Hz}}$.

Ključne besede: milimetrsko področje, teraherci, mikrobolometriška antena, senzori, polja v goriščni ravnini

* Corresponding Author's e-mail: leon.pavlovic@fe.uni-lj.si

1. Introduction

The research at millimeter-wave (mm-wave) and terahertz (THz) frequencies has been a continuous challenge for many decades and various applications, like radio astronomy, instrumentation, security, medicine, telecommunication, radar, etc. /1, 2/. For the mm-wave and THz sources (using either electrical, photonics or photo-conductive devices) and receivers the choice of an efficient antenna has been very applicative or device limited. Many antenna types, like the dipole, slot, spiral, bow-tie, log-periodic and horn, were successfully implemented at these frequencies /3, 4, 5, 6/. Due to its relatively simple manufacturing process and implementation, a planar antenna is a popular type. One of the most important limitations of a planar-antenna design is the choice of a suitable substrate, since it affects the antenna properties significantly. High-resistivity silicon (HR-Si) or indium phosphide (InP) substrates are typically the best choices, however (doped) silicon sub-

strate is also applicable or even desirable in some cases (suppression of unwanted resonances). The substrate thickness must be carefully chosen, otherwise surface waves in the substrate (for example, TM_0 mode has a zero cut-off frequency) might have a major impact on the antenna performance (mostly reduced efficiency) when the substrate is thicker than approx. $\lambda/50$ /7, 8, 9/. Often when a thick high-permittivity substrate is used, a large (typically HR-Si) lens is added underneath the substrate to couple the radiation through the substrate and lens /10/. For the focal-plane-array (FPA) imaging either a single lens or a lens array, i.e. fly's eye, can be used for the focusing of the received wave /8/. Another possibility is that the planar antenna is placed on a thin membrane with a ground plane distanced at $\lambda/4$ from the antenna-structure metallization.

2. Antenna design

The antenna as an element of the receiving FPA imaging system must fulfill certain requirements: small crosstalk between adjacent antennas, low side lobes, small footprint, high efficiency, optimal impedance and radiation pattern, easy integration with the receiver electronics, etc. In our case the antenna directivity of about 12 dBi for each element was targeted to meet the required spatial resolution of the complete FPA using a large dielectric lens for the focusing.

A planar antenna on a thin membrane and a back-side metallization was chosen with the dipole as an antenna element. Simulation results proved that a 620 μm long and a 40 μm wide (full-wavelength) dipole in a free space (or on a thin membrane) is resonant at 300 GHz. A full-wavelength dipole was chosen over the half-wave dipole because of a higher directivity and higher impedance (approx. 500 Ω at resonance), respectively. Since the directivity of a single dipole is too small, a second dipole was added in parallel to form a dipole array. A double full-wavelength dipole antenna can have a symmetric radiation pattern, high directivity, high impedance (discussed later) and relatively simple manufacturing. The two dipoles are 612 μm apart and are connected by a parallel transmission line (width/gap/width = 5/20/5 μm). The whole antenna structure with the detail of the realized load (Titan thermistor) is shown in Fig. 1 and one half of the antenna metallization in Fig. 2.

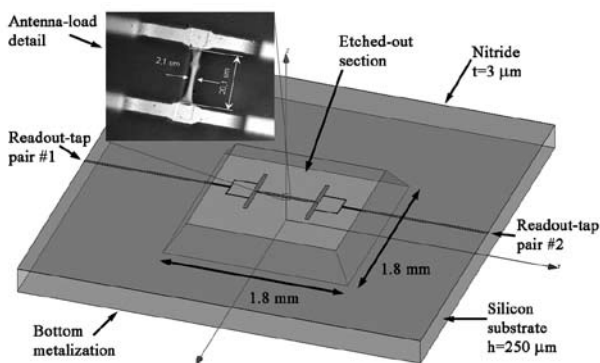


Figure 1: 300 GHz antenna structure with the realized antenna-load (thermistor) detail.

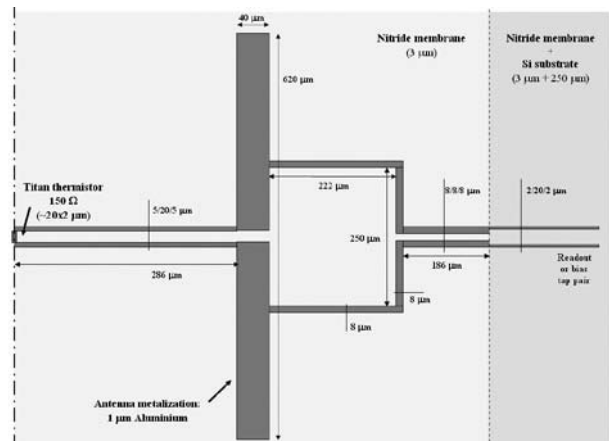


Figure 2: One half of the antenna metallization.

The double-dipole antenna lies on a thin (3 μm thick) nitride membrane attached to a 250 μm thick (doped) silicon substrate. A thin silicon dioxide membrane was also tested, but was found to be too fragile during the manufacturing process. During the manufacturing, the antenna metallization (1 μm thick aluminum) on top of a thin nitride layer first lie on a bulk silicon substrate, which is later etched-out underneath the area of the antenna metallization. In this way an air pyramidal section (with the cross section of about $1.8 \times 1.8 \text{ mm}^2$) is created below the two dipoles. Finally, the substrate with the membrane in the center is glued to a golden metallic plate (holder). The antenna cross section is shown in Fig. 3.

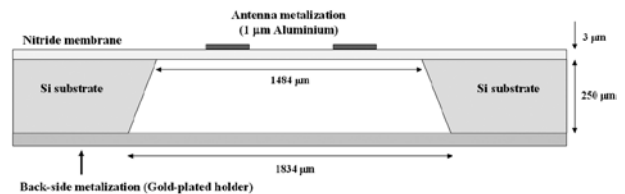


Figure 3: The antenna cross section.

The readout-tap pairs combine an impedance-transformation and low-pass sections, respectively, and are identical on both sides of the antenna. They are connected to the dipoles at a point of a maximal current (lowest impedance) at resonance. That is 125 μm from the dipole's gap. In this way the readout and bolometer bias traces do not interfere with the antenna performance. The impedance transformation is done two times: firstly on the membrane and secondly on the membrane-to-substrate interface by an impedance change of the readout transmission lines. The low-pass section is implemented as a transmission line on a (lossy) silicon substrate. One readout-tap pair is used for the bolometer (thermistor) current bias and the other for the voltage readout, therefore the DC resistance of the antenna metallization does not

influence the low-frequency nor the DC measurements.

3. Measurements and results

The experimental setup included a 300 GHz transmitter and a receiver, comprising the double-dipole antenna as a detector and a lock-in amplifier for the readout and processing. The antenna load (thermistor as a bolometer) had a low-noise DC-current bias connected through one of the readout-tap pairs. The 300 GHz transmitter used was an experimental amplifier-multiplier-chain system (x24 frequency multiplication) delivering the output power of about 3-4 mW at 300 GHz out of the horn antenna. The multiplier chain has an operating frequency range of about 290 to 330 GHz and features an on-off modulation capability. The transmitter antenna is a rectangular horn with 26 dBi of gain. The lock-in amplifier and the transmitter's modulation input were driven synchronously at a frequency of 530 Hz. The antenna was fixed to a rotatable table and positioner stages for a precise position and orientation alignment. A close agreement is found between the simulated and the measured radiation patterns, which are shown in Fig. 4 and 5, respectively. For the numerical simulations the FEM (Ansoft HFSS) and the FDTD (CST MWS) solvers were used.

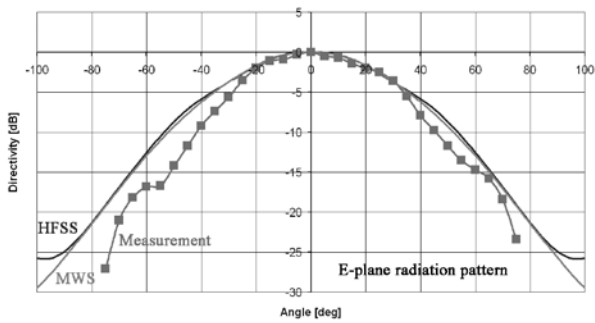


Figure 4: Measured and simulated E-plane radiation pattern at 320 GHz.

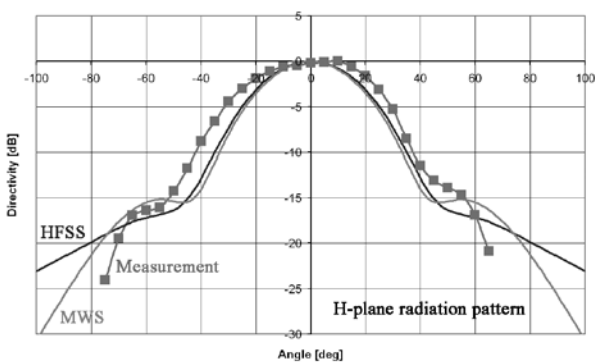


Figure 5: Measured and simulated H-plane radiation pattern at 320 GHz.

The numerically-computed directivity of the antenna is about 11.7 dBi at 85 % radiation efficiency. The simulated impedance of the antenna is $100 + j40 \Omega$ at 300 GHz with the (full-wave) resonance at 280 GHz. The DC resistance of the realized Titan thermistor (20 μm long and about 2 μm thick) is 150Ω and provides a relatively good match to the antenna impedance. A mismatch loss of about 1 dB was estimated. The responsivity of the microbolometer antenna was measured at 0.75 mA DC-current bias through the thermistor (bolometer). The distance between the transmitter and the receiver antenna was 110 mm. For the measured voltage of 48.4 μV (by the lock-in amplifier) at 530 Hz modulation frequency a responsivity of 40 V/W was calculated.

The noise-equivalent power (NEP) was also estimated. The noise spectral density for the Titan 150Ω thermistor used is about $1.8 \times 10^{-9} \text{ V}/\sqrt{\text{Hz}}$. Taking into consideration the responsivity of 40 V/W at 0.75 mA bias the NEP of $4 \times 10^{-11} \text{ W}/\sqrt{\text{Hz}}$ is obtained. As a reference the NEP of $5 \times 10^{-11} \text{ W}/\sqrt{\text{Hz}}$ was reported for the Golyay-cell detector [11]. The manufactured antenna was mounted onto a gold-plated multi-pin metal holder for an easy bonding and practical handling. A photograph of the antenna is shown in Fig. 6, where the antenna metallization on the membrane is clearly visible.

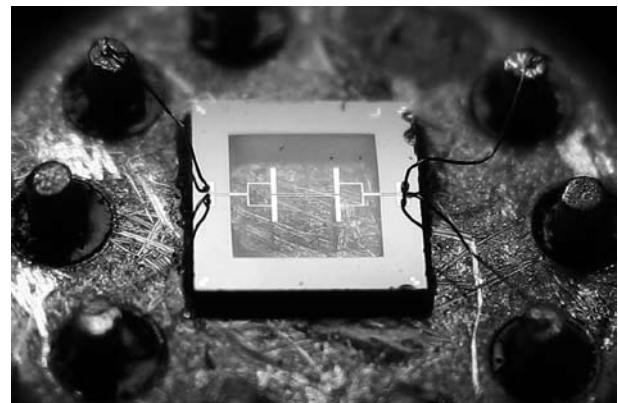


Figure 6: Photograph of the 300 GHz double-dipole antenna prototype mounted on a metal holder.

4. Conclusion

A 300 GHz room-temperature microbolometer double-dipole antenna for the FPA imaging has been fabricated. The antenna with a Titan bolometer consists of a full-wavelength dipole array on a 3 μm thick nitride membrane, backed by a ground plane at a 250 μm distance. Double impedance-transformation and low-pass-filter tap pairs on a silicon substrate are provided for the bias and readout, respectively. The measured radiation

patterns correspond well to the simulated patterns with the directivity of 11.7 dBi at the 85 % radiation efficiency at 300 GHz. The simulated antenna impedance at the feed point is about 100 Ω . Double filter-integrated tap pairs from the microbolometer antenna ensure optimal bolometer readout, since one tap pair provides the bolometer bias, while the other voltage readout. The antenna occupies an area of approx. 1.8x1.8 mm². A responsivity of 40 V/W and a NEP of 4 x 10⁻¹¹ W/ \sqrt Hz have been measured. Further improvements of the antenna will include a thin-film Bismuth bolometer, a vacuum encapsulation of the antenna structure and finally an active sensor/detector for a heterodyne receiver. Until now, a commercial lock-in amplifier has been used for the readout. Readout electronics is currently in development and will be later integrated with the antenna.

Acknowledgement

Authors would like to thank Slovenian Ministry of Defence for the research funding. In addition we thank dr. Marijan Macek and other team members of Laboratory for microelectronics, Faculty of Electrical Engineering, University of Ljubljana, for manufacturing and testing of the antenna devices and also for many fruitful discussions.

References

- 1 GOLDSMITH, P. F., HSIEH, C.-T., HUGUENIN, G. R., KAPITZKY, J., and MOORE, E. L.: 'Focal plane imaging systems for millimeter wavelengths', IEEE transactions on microwave theory and techniques, Vol. 41, No. 10, October 1993, pp. 1664-1675.
- 2 SIEGEL, P. H.: 'Terahertz technology', IEEE transactions on microwave theory and techniques, Vol. 50, No. 3, March 2002, pp. 910-928.
- 3 SIEGEL, P. H., DE MAAGT, P., and ZAGHLOUL, A. I.: 'Antennas for terahertz applications', IEEE antennas and propagation society international symposium, July 2006, pp. 2383-2386.
- 4 REBEIZ, G. M.: 'Millimeter-wave and terahertz integrated circuit antennas', Proceedings of the IEEE, Vol. 80, No. 11, November 2002, pp. 1748-1770.
- 5 FILIPOVIC, D. F., GEARHART, S. S., and REBEIZ, G. M.: 'Double-slot antennas on extended hemispherical and elliptical silicon dielectric lenses', IEEE transactions on microwave theory and techniques, Vol. 41, No. 10, October 1993, pp. 1738-1749.
- 6 FILIPOVIC, D. F., ALI-AHMAD, W. Y., and REBEIZ, G. M.: 'Millimeter-wave double-dipole antennas for high-gain integrated reflector illumination',

- IEEE transactions on microwave theory and techniques, Vol. 40, No. 5, May 1992, pp. 962-967.
- 7 ALEXOPOULOS, N. G., KATEHI, P. B., and RUTLEDGE, D. B.: 'Substrate optimization for integrated circuit antennas', IEEE transactions on microwave theory and techniques, Vol. MTT-31, No. 7, July 1983, pp. 550-557.
- 8 ROGERS, R. L., and NEIKIRK, D. P.: 'Use of broadside twin element antennas to increase efficiency on electrically thick dielectric substrates', International journal of Infrared and millimeter waves, Vol. 9, No. 11, 1988, pp. 949-969.
- 9 POZAR, D. M.: 'Considerations for millimeter wave printed antennas', IEEE transactions on antennas and propagation, Vol. AP-31, No. 5, September 1983, pp. 740-747.
- 10 YNGVESSON, S., GERECHT, E., NICHOLSON, J., RODRIGUEZ-MORALES, F., GU, D., ZHAO, X., WALDMAN, J., GOYETTE, T., and KOLLBERG, E.: 'Development of focal plane arrays with hot electron bolometer heterodyne detectors for 3 to 10 THz', IEEE Aerospace conference proceedings, 2004, pp. 724-734.
- 11 NAFTALY, M., DEAN, P., MILES, R. E., FLETCHER, J. R., and MALCOCI, A.: 'A simple interferometer for the analysis of terahertz sources and detectors', IEEE journal of selected topics in quantum electronics, Vol. 14, No. 2, March/April 2008, pp. 443-448.

Arrived: 24. 03. 2011

Accepted: 26. 1. 2012

Measurement system for testing of bipolar plates for PEM electrolyzers

Marko Petkovšek^{1*}, Peter Kosmatin¹, Ciril Zevnik², Danijel Vončina¹, Peter Zajec¹

¹ University of Ljubljana, Faculty of Electrical Engineering, Ljubljana, Slovenia

² Leonardo, d.o.o., Kranj

Extended abstract: The paper gives an insight into part of our research work in the field of hydrogen production by means of water electrolysis. With such approach, extremely pure hydrogen can be produced (purity above 99.99% is quite common). Furthermore, electrolyzers can produce hydrogen at high pressure (20 MPa or even more) without the use of additional compressors /1-3/. Since the electrolysis requires a source of high quality energy – i.e. electrical energy, the costs of the produced hydrogen from electrolyzers are relatively high. To minimize them, one can use electrical energy from conventional power plants during their off-peak hours. Alternatively, one can use electrical energy from renewable sources, like for instance from photovoltaic power plants /4/. We designed a measurement system for testing laboratory electrolyzers with key components being a polymer membrane for exchanging protons (PEM membrane) and a bipolar plate. The main focus in our research was to study the effect of types and forms of the distribution field and design methods for manufacturing of bipolar plates on the overall performance of the electrolysis. Firstly, we tested bipolar plates that were assembled together using the Metal-Core technology. For the anode and cathode, we used a metal foil of titanium and stainless steel, while the linkage between the final electrode and the inner copper layers was successfully solved by the use of a conductive adhesive (Ablebond). Despite relatively encouraging initial results, further testing of this type of bipolar plates was abandoned, due to a problematic titanium foil milling, flooding of internal cooling channels and leakages in parts where the conductive adhesive was applied. Further testing was then performed on bipolar plates that have been produced using high temperature pressing (prepreg) of pre-treated metal plates. We used a mesh of expanded titanium (anode) and a mesh of expanded stainless steel (cathode) as outer layers of the bipolar plate, which resulted in a pin-type of the distribution field. Furthermore, we modified the original rectangular shape of the distribution field into a more effective shape of a prolonged deltoid. By doing so, we minimized the lag of water and gases in the area of cell corners which resulted in a better efficiency of the electrolysis cell (during testing a current density of 0.8 A/cm² was measured). The latter can be furthermore improved if we use a PEM membrane with catalyst coating on both sides. In this way, the current density of 1 A/cm² can be achieved, which is directly reflected on the amount of the produced hydrogen.

Key words: electrolysis, PEM membrane, bipolar plate, hydrogen, distribution field

Merilni sistem za testiranje bipolarnih plošč PEM elektrolizne celice

Izvleček: V prispevku podajamo vpogled v del naših raziskov na področju generiranja vodika s postopkom elektrolize vode. V ta namen smo izdelali merilni sistem za testiranje laboratorijskih elektroliznih celic, katerih ključna sestavna dela sta polimerna membrana za izmenjavo protonov (PEM membrana) in bipolarna plošča. Prav slednja je bila predmet naših študij, saj smo analizirali vpliv vrste in oblike distribucijskega polja ter načina izdelave bipolarne plošče na učinkovitost delovanja elektrolizne celice. Ob uporabi bipolarnih plošč, izdelanih po postopku lepljenja predhodno obdelanih kovinskih plošč, in z modificirano obliko distribucijskega polja ter uporabo PEM membrane brez katalizatorja smo tako dosegli gostoto toka do 0,8 A/cm². Glede na obetavne rezultate začetnih testiranj s katalizirano membrano pa pričakujemo, da bomo z modificiranim distribucijskim poljem dosegli še višjo gostoto toka in s tem večjo učinkovitost elektrolizne celice.

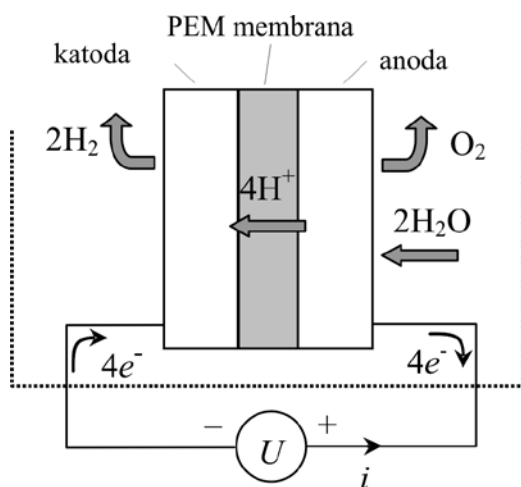
Ključne besede: elektroliza, PEM membrana, bipolarna plošča, vodik, distribucijsko polje

* Corresponding Author's e-mail: marko.petkovsek@fe.uni-lj.si

1. Uvod

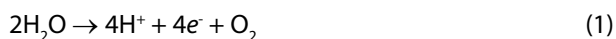
Pridobivanje vodika s pomočjo elektrolize vode je dandanes precej uveljavljen postopek, še posebno v primerih, ko je zahtevana visoka stopnja čistosti. Poleg alkalne elektrolize tu prednjačijo predvsem elektrolizne celice s PEM polimerno membrano (PEM; Proton Exchange Membrane), kjer kot nečistoča pri postopku pridobivanja vodika nastopa takorekoč samo voda oziroma vodna para. S sodobnimi elektroliznimi celicami je tako možno proizvesti zahtevano količino vodika s čistostjo tudi nad 99,99%. Dodatna odlika PEM elektroliznega postopka v primerjavi z ostalimi postopki pa je možnost neposrednega visokotlačnega (večinoma do 20 MPa, lahko tudi več) shranjevanja nastalega plina brez dodatnih kompresijskih enot /1-3/. Ker pa je postopek elektroliznega pridobivanja vodika vezan na uporabo visokokvalitetne električne energije, je cena tako proizvedenega vodika relativno visoka. Proizvodne stroške je npr. možno znižati z delovanjem v času nizke tarife, druga možnost pa je uporaba električne energije iz obnovljivih virov – predvsem iz fotonapetostnih modulov /4/.

Princip delovanja elektrolizne celice je vezan na razpad molekul vode na vodik in kisik pod vplivom dovajane električne energije, ki se teoretično zgodi pri napetosti 1,23 V med anodno in katodno stranjo elektrolizne celice /5/. Na anodni strani (slika 1) dovajamo v elektrolizno celico vodo, ki se razcepi na vodikove protone (prodirajo skozi protonsko izmenljivo (PEM) membrano na katodno stran), kisik (O_2) in elektrone (omogočijo sklenitev električnega tokokroga, ki ga napaja vir napetosti U).



Slika 1: Princip delovanja PEM elektrolizne celice.

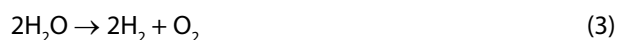
Reakcija na anodni strani je torej:



Na katodni strani pa se vodikovi protoni rekombinirajo z elektroni in tvorijo vodik (H_2):

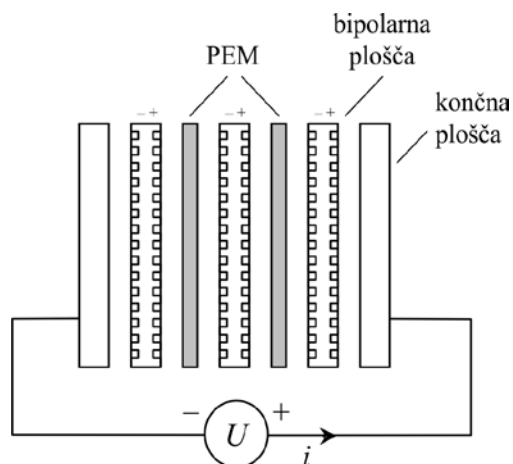


Celotno reakcijo lahko zapišemo kot:



Iz poteka kemijskih reakcij (npr. 2) je razvidno, da sta pri nastanku molekule plina vodika sodelovala dva elektrona. Slednje lahko upoštevamo pri oceni učinkovitosti elektrolizne celice, saj je količina proizvedenega vodika dejansko premosorazmerna pretečenemu naboju. Ker je velikost toka med elektroliznim postopkom odvisna od aktivne površine celice, na kateri poteka elektrolizna reakcija (površina PEM membrane), pogosto kot merilo učinkovitosti elektrolizne celice uporabljamo kar gostoto toka v A/cm^2 .

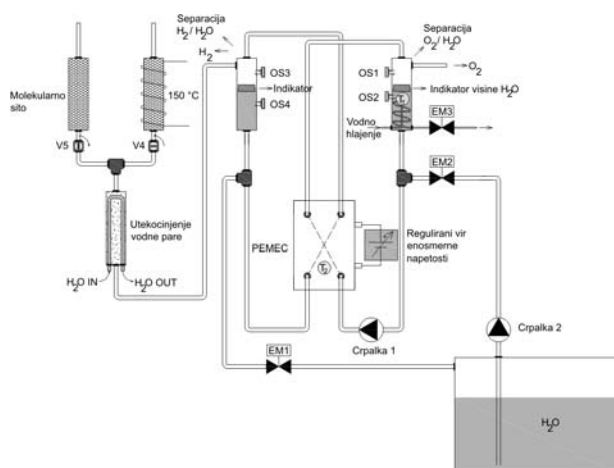
V praksi po navadi uporabljamo več v niz povezanih celic, s čimer povečamo zmogljivost elektrolizne enote. Pri tem je anodna stran prve celice povezana s katodno stranjo naslednje. V konstrukcijskem pogledu je nastali spoj dveh nasprotno nabitih elektrod sosednjih celic smiselno obravnavati skupaj, a ločeno od membranskega dela posamezne osnovne celice. Tako dobljeni sklop je zaradi različnih nabojev na obeh straneh poimenovan tudi bipolarna plošča in je poleg PEM membrane ključen elektromehanski element elektrolizne celice. Bipolarna plošča v elektrolizni celici tako omogoča dovod vode, distribucijo plinov (vodik, kisik) in povezovanje več osnovnih celic z namenom povečevanja moči elektrolizne enote in s tem količine proizvedenega vodika. Na sliki 2 je prikazana shema sestavljene elektrolizne celice z dvema PEM membranama in tremi bipolarnimi ploščami. Celica je na obeh straneh zaključena s končnima ploščama, na katerih sta nameščena tudi elektrodna priključka za napajalni vir.



Slika 2: Shema sestavljene elektrolizne celice.

2. Kontrolno-merilni sistem za testiranje PEM elektrolizne celice

Za kritično ovrednotenje uporabljenih komponent PEM elektrolizne celice (PEMEC) je pri testiranju delovanja treba imeti na razpolago ustrezno merilno okolje. S slednjim moramo zajeti več ključnih področij – od nadzora električnih parametrov elektroliznega postopka, zanesljive ločitve nastalih plinov od vode, nadzora temperature in tlaka izstopnih plinov med elektroliznim postopkom, pa vse do ustreznega krmiljenja vodnega pretoka na anodni strani in nadzora nivoja vode na katodni strani. Pri prehodu vodikovega protona skozi PEM membrano moramo namreč upoštevati, da skozi membrano dejansko prestopa vodikov proton skupaj s hidratno ovojnico – torej v obliki iona H_3O^+ . To pa pomeni, da sta z vsako nastalo molekulo plina H_2 na katodno stran prešli tudi dve molekuli vode z anodne strani. Posledica tega je seveda večji primanjkljaj vode na anodni strani in presežek vode na katodni. Za samostojno in dolgotrajno delovanje elektrolizna celica zato potrebuje krmilno-merilni sistem, ki zagotavlja konstantno enosmerno napetost med anodnim in katodnim priključkom celice, stalno prisotnost deionizirane vode tako v sami celici kot tudi v obeh separatorjih sistema in njeno hlajenje. Na sliki 3 je podana shema krmilno-merilnega sistema, ki smo ga uporabili pri testiranju bipolarnih plošč.



Slika 3: Kontrolno-merilni sistem PEM elektrolizne celice.

Zadostno količino deionizirane vode v testirani elektrolizni celici nadziramo posredno preko merjenja nivoja vode v obeh separatorjih. Na njih sta zato dodana dva optična senzorja (IR oddajna in sprejemna dioda), ki s pomočjo črpalke 2, elektromagnetnega ventila 2 in elektromagnetnega ventila 1 vzdržujeta količino razpoložljive vode znotraj nastavljenih meja. Če pade nivo vode v kisikovem separatorju v območje spodnjega

optičnega senzorja (OS2), vklopimo črpalko 2, hkrati pa odpremo tudi ventil EM2 in nivo vode začne naraščati. Ob doseženem nivoju, ki ga detektira zgornji senzor OS2, izklopimo črpalko 2 in ventil EM2. V vodikovem separatorju se med obratovanjem zaradi prehoda H_3O^+ ionov skozi membrano celice ustvarja presežek vode, zato moramo nivo vode regulirati s krmiljenjem elektromagnetnega ventila EM1, s katerim presežek vode spustimo v skupni rezervoar sistema.

Delovanje elektrolizne celice je zelo odvisno tudi od temperature, zato je pri analizi učinkovitosti uporabljene bipolarnih plošč pomembno nadzorovati tudi temperaturo celice. Sistem hlajenja celice je v našem primeru izveden s pomočjo toplotnega izmenjevalnika v kisikovem separatorju. Toplotni izmenjevalnik je preko elektromagnetnega ventila EM3 priključen na vodovodno omrežje, krmiljenje ventila pa je pogojeno z informacijo o temperaturi iz dveh temperaturnih senzorjev (T1 in T2, tip TC74), ki sta nameščena na zunanjo steno separatorja (T1) in elektrolizne celice (2). Na ta način lahko dosežemo vzdrževanje konstantne temperature celice med delovanjem v relativno ozkem temperaturnem območju ($\Delta T = \pm 3 \text{ }^\circ\text{C}$).

Nadzor nad delovanjem vseh podsistemov izvaja mikro-krmilnik PIC 18F458, ki ga krmilimo s pomočjo osebnega računalnika z LabView programsko aplikacijo. Na ta način je poskrbljeno tudi za vizualni prikaz delovanja in stanja celice, shranjevanje izmerjenih veličin in krmiljenje napetostnega vira.

3. Bipolarna plošča za PEM elektrolizno celico

3.1. Materiali

Pri izbiri in konstrukcijski zasnovi sestavnih delov PEM elektrolizne celice je seveda poglobitnega pomena ustrezna izbira polimerne membrane. Tu bi v grobem lahko izbirali glede na predvideno temperaturno območje delovanja in prisotnost katalizatorja na eni ali obeh straneh membrane. Kljub obširnimi raziskavam materialov za membranski sestav MEA (*membrane electrode assembly*), je to področje praktično vezano le na nekaj ključnih globalnih dobaviteljev (3M, Dupont, Fumatech,...). Povsem drugače je pri konstrukciji bipolarnih plošč – pa naj si gre za plošče za elektrolizno celico ali pa gorivno celico – razvoj in analiza materialov za bipolarne plošče je v zadnjem času predmet številnih raziskav [6-10]. Ključni problem pri tem predstavlja pasivacija anodne površine bipolarne plošče, ki posledično poveča prehodno upornost in končno onemogoči normalno delovanje PEM elektrolizne celi-

ce. Materiali za bipolarne plošče morajo zato izkazovati visoko korozijsko odpornost, biti morajo kar se da dobro mehansko in termično stabilni, v stiku z elektrolitom pa ne sme priti do pasivacije anodne elektrodne površine. Največkrat na anodni strani uporabljamo ploščevino iz titana, ki je po navadi oplemenitena s platino, iridijevem dioksidom ali kakšnim drugim materialom iz platinske skupine kovin /11/. Poseben poudarek pri izbiri materialov je treba nameniti tudi katodni strani, kjer prevladujeta nerjavno jeklo in grafit. Slednji je npr. ključen za nemoteno tvorbo vodika v skladu z reakcijo (2) in ga na katodno stran vgrajujemo v obliki grafitnega papirja z mikro dopiranimi ogljikovimi zrcni. Tako na katodni strani ustvarimo tanko porozno plast (MPL, *micro porous layer*), skozi katero lahko prehaja vodik v plinastem stanju.

3.2. Vrsta in oblika distribucijskega polja

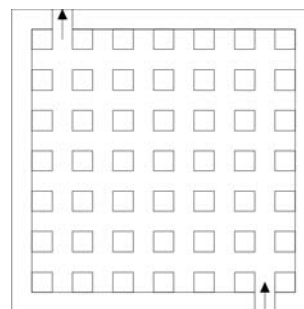
Poleg materialov membranskega elektrodnega sestava in materialov za bipolarne plošče pa je seveda za delovanje elektrolizne celice nadvse pomembna tudi konstrukcija same bipolarne plošče. Pri tem je treba imeti v mislih, da je pri zaporedni vezavi več samostojnih celic (slika 2) treba konstrukcijsko rešiti več medsebojno odvisnih sistemov. Namreč, poskrbeti je treba za dovajanje zadostne količine sveže vode (črpalka 1 na sliki 3), poskrbeti za dovod električne energije in odvod nastalih plinov na posamezni celici ter poskrbeti, da ob delovanju sestavljene elektrolizne celice ne prihaja do lokalnega pregrevanja (nazivna delovna temperatura na trgu dostopnih PEM elektroliznih celic je $\approx 70\text{ }^{\circ}\text{C}$). V tem pogledu je najbolj kritičen element pravzaprav PEM membrana (tako pri elektrolizni kot gorivni celici) – predmet intenzivnih raziskav je zato možnost dviga delovne temperature na okoli $120\text{ }^{\circ}\text{C}$ in doseganje dolgotrajne stabilnosti /12/.

Pri konstrukciji bipolarnih plošč je tako možno izbirati med različnimi vrstami distribucijskega polja /13/, s čimer pa je seveda posledično določena tudi izbira materialov in tehnoloških postopkov za izdelavo bipolarnih plošč. V naših testiranjih smo se omejili na dve najpogostejše uporabljani vrsti distribucijskega polja (slika 4):

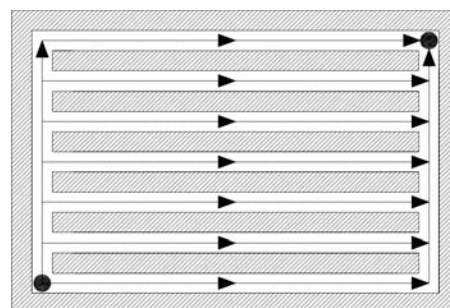
- prosto distribucijsko polje (*pin type*) in
- usmerjeno distribucijsko polje (serpentina).

Prvo vrsto distribucijskega polja lahko tehnološko izvedemo npr. z uporabo ekspandirane mreže iz titana, ki jo lahko nadalje na anodni strani oplemenitimo s prevleko IrO_2 ali kakšno drugo prevleko. Pri drugi vrsti distribucijskega polja je v nosilno strukturo (plošča iz plemenite kovine – npr. Nb, Ti) treba zarezati en ali več vzporednih kanalov, kar je npr. možno storiti s postopkom rezkanja z vodnim curkom.

Četudi je pri obravnavanju vrste distribucijskega polja predpostavljena pravokotna oblika polja, le-ta ne zagotavlja dobre hidrodinamike in je vzrok za zastajanje plina in s tem slabše delovanje elektrolizne celice. Študij oblike distribucijskega polja je posledično predmet številnih raziskav interdisciplinarno obarvanih raziskovalnih skupin /14-16/.



a)



a)

Slika 4: Vrsta distribucijskega polja pri bipolarni plošči za PEM elektrolizo: a) prosto polje b) usmerjeno polje.

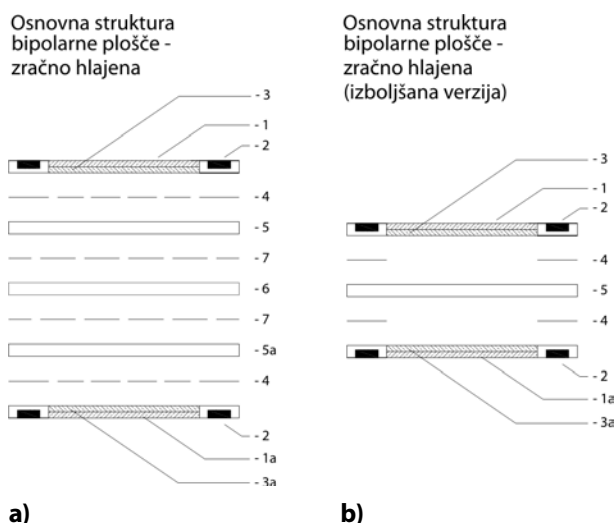
4. Eksperimentalni rezultati

Pri izdelavi bipolarne plošče za PEM elektrolizo smo pri prvih testiranjih uporabljali Metal-Core tehnologijo. Za anodno in katodno površino smo uporabili kovinski foliji iz titana in nerjavnega jekla, povezavo med končno elektrodo in notranjimi bakrenimi plastmi pa smo uspešno rešili z uporabo prevodnega lepila Ablebond (na sliki 5 je prikazana na ta način izdelana bipolarna plošča z usmerjenim distribucijskim poljem in aktivno površino 92 cm^2 ; dimenzije $7,6\text{ cm} \times 12,1\text{ cm}$). Kljub relativno vzpodbudnim začetnim rezultatom smo omenjeni tehnološki postopek opustili zaradi težavnega rezkanja folije iz titana, zalivanja notranjih hladilnih kanalov celice in slabega tesnjenja na delih, kjer je bila uporabljena prevodna pasta Ablebond.



Slika 5: Bipolarna plošča za PEM elektrolizo-izdelana z Metal-Core tehnologijo.

Nadaljnja testiranja smo izvedli z bipolarnimi ploščami, ki so bile izdelane s postopkom lepljenja predhodno obdelanih kovinskih plošč. Tu smo sprva uporabljali relativno kompleksno zgradbo z bakreno sredico in lepljenjem s prevodnim lepilom (slika 6a). Tudi v tem primeru je uporaba prevodnega lepila negativno vplivala na tesnjenje celice, zato smo tak pristop popolnoma opustili in prešli na bolj preprosto zgradbo, ki jo kaže slika 6b. Bakreno plast smo zamenjali s tanko pločevino iz titana (0,3 mm), lepljenje plošč pa smo izvedli s stiskanjem s prepregom pri 170 °C. Kasnejše preskušanje obeh sistemov je pokazalo, da vlogo bakrenega jedra prevzame kovinska struktura iz titana in nerjavnega jekla, s postopkom prepreg stiskanja pa smo odpravili slabo ali nezadostno tesnjenje, do katerega je prihajalo ob uporabi Ablebond prevodnega lepila.

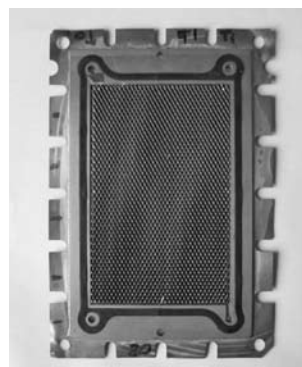


Legenda:

- 1 Ti mreža, tipG oplemenitena površina-anoda
- 1a SS pločevina, 0,15mm; 0,8 mm/0,8 mm
- 2 EPDM vloženo tesnilo
- 3 Ti mreža, tipG –anoda
- 3a SS mreža- katoda
- 4 prepreg
- 5 Ti pločevina 0,5mm
- 6 Cu pločevina 0,5mm
- 7 prevodna pasta Ablebond
- 5a SS pločevina 0,3 mm

Slika 6: Shematičen presek bipolarne plošče a) s Cu jedrom; b) izboljšana in poenostavljena izvedba.

Na sliki 7 je fotografija izdelane bipolarne plošče z bakrenim jedrom z aktivno membransko površino 92 cm² in tesnilom iz EPDM vulkanizirane gume. Na anodni strani bipolarne plošče je vgrajena ekspandirana mreža iz Ti pločevine (tip G) s prevleko IrO₂, katodna stran pa je izdelana iz mrežastega nerjavnega jekla tip 316. Glede na porozno strukturo na anodni in katodni strani lahko v tem primeru govorimo o distribucijskem polju s prostim pretokom.

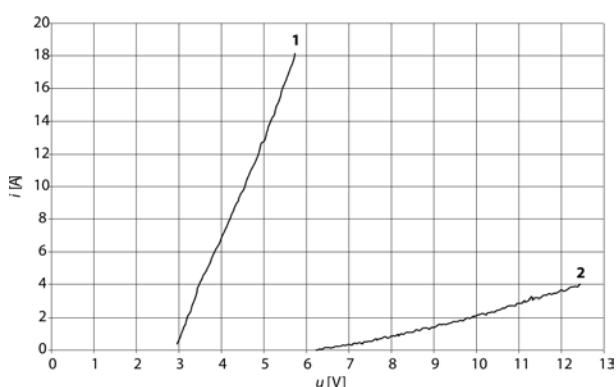


Slika 7: Bipolarna plošča z bakrenim jedrom; pogled na anodno stran.

V nadaljevanju so podrobneje analizirani rezultati testiranja elektrolizne celice s tremi bipolarnimi ploščami in dvema membranama MEA s skupno aktivno površino $2 \times 92 \text{ cm}^2$. Bipolarne plošče so bile izdelane po izboljšanem in preprostejšem postopku, notranji presek take bipolarne plošče kaže slika 6b. Na sliki 8 sta podani polarizacijski krivulji za dve celici z različnima membranama, in sicer:

- PEM membrana brez katalizatorja (F9100), katalizator IrO_2 je nanešen na Ti anodi in
- PEM membrana z obojestransko nanešenim katalizatorjem (N115).

Razvidno je, da je membrana z obojestransko nanešenim katalizatorjem (N115) v pogledu učinkovitosti delovanja elektrolizne celice in s tem večje količine proizvedenega vodika (večji tok elektrolize) bistveno boljše kot membrana brez katalizatorja (F9100). V tem primeru je katalizator sicer prisoten, a le kot prevleka na anodni strani bipolarne plošče. Pri uporabi katalizirane membrane (N115; krivulja 1) se kemijska reakcija razpada vode na vodik in kisik prične že pri napetosti $\approx 3 \text{ V}$ (torej $1,5 \text{ V}$ na celico), medtem ko je pri membrani F9100 (krivulja 2) ta napetost precej višja. V obeh primerih je bila delovna temperatura celice med testom $T = 25 \text{ }^\circ\text{C}$, kar je relativno nizka vrednost. Kot bo razvidno iz rezultatov v nadaljevanju, je učinkovitost delovanja elektrolizne celice mogoče zvišati z zvišanjem delovne temperature. Vsekakor pa lahko na podlagi analize rezultatov testiranja zaključimo, da je pri konstrukciji elektrolizne celice za čim večjo proizvodnjo vodika smiselno uporabiti membrano z obojestranskim nanosom katalizatorja.



Legenda:

- 3x bipolarna plošča, 2x membrana (duPont - tip N115), pravokotno distribucijsko polje, $T = 25 \text{ }^\circ\text{C}$
- 3x bipolarna plošča, 2x membrana (Fumatech - tip F9100), pravokotno distribucijsko polje, $T = 25 \text{ }^\circ\text{C}$

Slika 8: Vpliv membrane na polarizacijsko krivuljo.

Na začetku raziskav smo za obliko distribucijskega polja privzeli pravokotno obliko (slika 9a). Testiranje PEM

elektrolizne celice s to izvedbo so pokazala vrsto težav, predvsem problematično pa je bilo zaostajanje pretoka vode in kisika v kotnih predelih distribucijskega polja. Na osnovi dolgotrajnih preskusov smo zato oblikovali novo distribucijsko polje, kot je prikazano na sliki 9b.



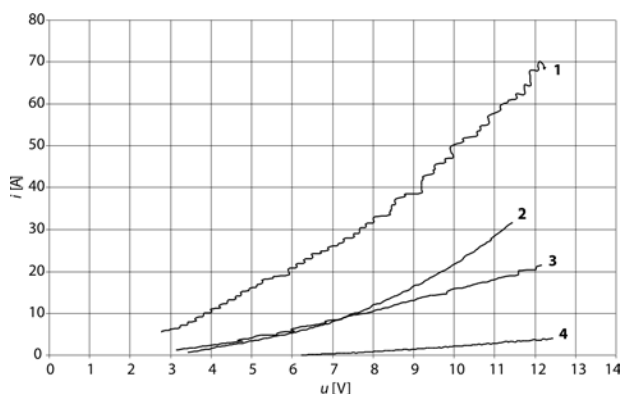
a) **b)**

Slika 9: Bipolarna plošča z a) pravokotno izvedbo distribucijskega polja in b) z izboljšano obliko distribucijskega polja.

Distribucijsko polje smo izdelali v obliki razpotegnjenega deltoida, kjer je vstop vode porazdeljen na 2 vstopna kanala. Voda se nato v poroznem sloju razporedi po celotnem preseku, kar onemogoči zaostajanje kot v primeru pravokotnega distribucijskega polja. Izstop vode in nastalega plina je mogoč skozi 4 izstopne kanale z različnim presekom.

Pri testiranju izboljšane oblike distribucijskega polja bipolarnih plošč smo uporabili nekatalizirano membrano (duPont N424), ki je v pogledu elektrokemijskih lastnosti enakovredna predhodno uporabljeni membrani F9100. Na podlagi primerjave polarizacijskih krivulj na sliki 10 lahko ugotovimo, da pri bipolarni plošči z izboljšanim distribucijskim poljem (krivulji 1 in 3) dosežemo bistveno boljše rezultate kot pri plošči s pravokotnim poljem (krivulja 2). Sestavljena elektrolizna celica z izboljšanim poljem ima tako npr. pri temperaturi $T = 25 \text{ }^\circ\text{C}$ (krivulja 3) skoraj identičen potek toka kot celica s pravokotnim distribucijskim poljem pri temperaturi $T = 60 \text{ }^\circ\text{C}$ (krivulja 2). Primerjava krivulj 2 in 4 (pravokotno polje) razkriva tudi veliko temperaturno odvisnost celice z nekatalizirano membrano – vsaj v pogledu minimalne napetosti za pričetek reakcije. Pri delovni temperaturi $T = 25 \text{ }^\circ\text{C}$ je namreč napajalna napetost, potrebna za pričetek reakcije, $u \approx 6 \text{ V}$ (oziroma 3 V na posamezno celico), že pri delovni temperaturi $T = 60 \text{ }^\circ\text{C}$ pa se te vrednosti praktično razpolovijo in s tem približajo teoretičnim vrednostim napetosti za razkroj vode.

Pri testiranju celice pri povišani delovni temperaturi ($T = 50\text{ }^{\circ}\text{C}$) in izboljšanem polju (krivulja 1) je pri napajalni napetosti 12 V bila dosežena gostota toka $j \approx 0,8\text{ A/cm}^2$, s čimer se že približujemo standardnim vrednostim na trgu dostopnih elektroliznih enot z gostoto toka okoli 1 A/cm^2 .

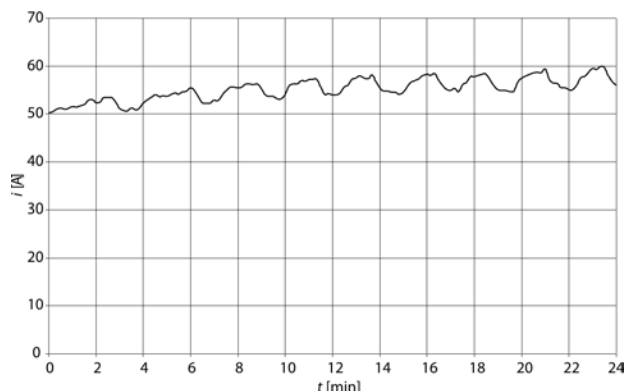


Legenda:

- 1 3x bipolarna plošča, 2x membrana (duPont - tip N424), deltoid distribucijsko polje, $T = 50\text{ }^{\circ}\text{C}$
- 2 3x bipolarna plošča, 2x membrana (F9100), pravokotno distribucijsko polje, $T = 60\text{ }^{\circ}\text{C}$
- 3 3x bipolarna plošča, 2x membrana (duPont - tip N424), deltoid distribucijsko polje, $T = 25\text{ }^{\circ}\text{C}$
- 4 3x bipolarna plošča, 2x membrana (F9100), pravokotno distribucijsko polje, $T = 25\text{ }^{\circ}\text{C}$

Slika 10: Vpliv oblike distribucijskega polja na delovanje elektrolizne celice.

Predhodno podane polarizacijske krivulje smo dobili s postopnim spreminjanjem napetosti na sponkah napajalnega vira (korak spremembe napetosti $\Delta u = 100\text{ mV/s}$). Po meritvi polarizacijskih krivulj celice z izboljšanim distribucijskim poljem na njej oz. njenih podsklopih nismo zaznali kakršnihkoli poškodb in posledic, ki bi negativno vplivale na nadaljnje delovanje, zato smo izvedli tudi daljši test delovanja pri konstantni napajalni napetosti. Na sliki 11 je podan časovni potek toka elektrolizne celice s tremi bipolarnimi ploščami in z dvema membranama (tip N424), pri čemer smo celico priključili na napajalno napetost 11 V in pri tem vzdrževali delovno temperaturo celice $T = 50\text{ }^{\circ}\text{C}$. Pri preizkusu smo dosegli enako povprečno vrednost toka, kot smo jo pri enaki napetosti dobili pri merjenju polarizacijske krivulje 1 na sliki 10. Zaključimo lahko, da je tako narejena elektrolizna celica primerna za dolgotrajnejše obratovanje, saj v času izvajanja testa in pri ponovljenih testiranjih ni prišlo do zmanjšanja učinkovitosti delovanja celice. Iz časovnega poteka je sicer razvidno nihanje toka, ki pa ga pripisujemo hladilnemu sistemu, s katerim lahko delovno temperaturo celice nastavljammo z natančnostjo $\pm 3\text{ }^{\circ}\text{C}$.



Legenda:

3x bipolarna plošča, 2x membrana (duPont - tip N424), deltoid distribucijsko polje, napajalna napetost $U = 11\text{ V}$, delovna temperatura celice $T = 50\text{ }^{\circ}\text{C}$

Slika 11: Časovni potek toka elektrolizne celice pri konstantni napajalni napetosti.

5. Sklep

V prispevku smo se osredotočili na prikaz naših raziskovalnih aktivnosti na področju generiranja vodika s pomočjo elektrolize vode v PEM elektrolizni celici. Učinkovitost elektrolizne celice je odvisna predvsem od dveh ključnih komponent, in sicer od PEM membrane in bipolarnih plošč. Naše raziskovalno delo je bilo usmerjeno predvsem na zasnovo in možne tehnološke prijeme pri izdelavi bipolarnih plošč, ki je, gledano s konstrukcijskega stališča, zelo kompleksen sistem. V ta namen smo zgradili tudi kontrolno-merilni sistem, s katerim je bilo možno voditi in nadzorovati elektrolizni postopek v skladu s predhodno zastavljenimi hipotezami.

V začetnih testiranjih smo uporabljali bipolarnih plošč, ki smo jih izdelali po postopku Metal-Core. Poleg nekaterih težav pri sami izdelavi (npr. zahtevno rezkanje ploščevine iz titana in nerjavnega jekla) smo tak postopek izdelave opustili tudi zaradi nezadostnega tesnjenja na mestih, kjer je bilo uporabljeno električno prevodno lepilo.

Nadaljnja testiranja smo izvedli z bipolarnimi ploščami, ki smo jih izdelali s tehnologijo visokotemperaturnega lepljenja in stiskanja (prepreg) kovinskih plošč iz titana in nerjavnega jekla. Pri tem smo se odločili za prosto distribucijsko polje na aktivni površini, kar smo dosegli z uporabo mreže iz ekspandirane titanove (anodna stran) in nerjavne ploščevine (katodna stran). Poleg tega smo klasično pravokotno obliko distribucijskega polja zamenjali za bolj učinkovito (podaljšan deltoid), s katero smo omogočili boljše odvajanje nastalih plinov z aktiv-

ne površine. Z izdelanimi bipolarnimi ploščami z izboljšano obliko distribucijskega polja in s PEM membrano brez katalizatorja smo pri sestavljeni elektrolizni celici (2, 3 oz. 4 membrane) ob povišani delovni temperaturi (do $T = 70\text{ }^{\circ}\text{C}$) uspeli doseči gostoto toka do $0,8\text{ A/cm}^2$. Glede na vzpodbudne začetne rezultate pričakujemo, da bo gostota toka v primeru uporabe katalizirane membrane preseгла vrednost 1 A/cm^2 , kar je primerljivo s sodobnimi elektroliznimi enotami na trgu.

Naše prihodnje raziskave bodo potekale v smeri optimizacije bipolarnih plošč z namenom zmanjšanja debeline in s tem mase plošč ob njihovi nezmanjšani učinkovitosti, kar bi se seveda neposredno odražalo na ceni izdelane elektrolizne celice. Poseben poudarek bo namenjen tudi nadaljnji analizi oblike distribucijskega polja in povezovalnih kanalov med posameznimi bipolarnimi ploščami.

Zahvala

V prispevku je bil del eksperimentalnih rezultatov pridobljen v okviru raziskovalnih projektov »H2PEM: Bipolarna plošča za reverzibilno pretvarjanje električne energije v kemično energijo vodika« in »HyMIV: Sistem gorivnih celic kot pomožni vir energije za zagotavljanje avtonomnosti vojaških vozil; podprojekt: Generiranje vodika z obnovljivimi viri energije za napajanje gorivnih celic«.

Literatura

- 1 S. A. Grigoriev, V. I. Porebsky, V. N. Fateev, "Pure Hydrogen Production by PEM Electrolysis for Hydrogen Energy," *Int. Journal of Hydrogen Energy*, 31, 171-176, 2006.
- 2 P. Millet, D. Dragoe, S. Grigoriev, V. Fateev, C. Etievant, "GenHyPEM: A research program on PEM water electrolysis supported by the European Commission," *International Journal of Hydrogen Energy*, 34, 4974-4982, 2009.
- 3 F. Marangio, M. Santarelli, M. Cali, "Theoretical model and experimental analysis of a high pressure PEM water electrolyser for hydrogen production," *International Journal of Hydrogen Energy*, 34, 1143-1158, 2009.
- 4 F. Barbir, "PEM electrolysis for production of hydrogen from renewable energy sources," *Solar Energy*, 78, 661-669, 2005.
- 5 M. Petkovšek, C. Zevnik, P. Kosmatin, P. Zajec, D. Vončina, "PEM elektrolizna celica - fizikalno ozadje delovanja," *Zbornik 17. mednarodne Elektrotehniške in računalniške konference ERK 2008*, 29.9. - 1.10. 2008, zv. A, str. 327-329, Portorož, Slovenija, 2008.
- 6 Y. Hung, K. M. El-Khatib, H. Tawfik, "Corrosion-resistant lightweight metallic bipolar plates for PEM fuel cells," *Journal of Applied Electrochemistry*, 35, 445-447, 2005.
- 7 E. A. Cho, U. S. Jeon, H. Y. Ha, S. A. Hong, I. H. Oh, "Characteristics of composite bipolar plates for polymer electrolyte membrane fuel cells," *Journal of Power Sources*, 125, 178-182, 2004.
- 8 H. Tawfika, Y. Hunga, D. Mahajan, "Metal bipolar plates for PEM fuel cell – A review," *Journal of Power Sources*, 163, 755-767, 2007.
- 9 J. Pettersson, B. Ramsey, D. Harrison, "A review of the latest developments in electrodes for unitized regenerative polymer electrolyte fuel cells," *Journal of Power Sources*, 157, 28-34, 2006.
- 10 V. Mehta, J. S. Cooper, "Review and analysis of PEM fuel cell design and manufacturing," *Journal of Power Sources*, 114, 32-53, 2003.
- 11 S. S. Dhrab, K. Sopian, M. A. Alghoul, M. Y. Sulaiman, "Review of the membrane and bipolar plates materials for conventional and unitized regenerative fuel cells," *Renewable and Sustainable Energy Reviews*, 13, 1663-1668, 2009.
- 12 B. Genorio, D. Strmcnik, R. Subbaraman, D. Tripkovic, G. Karapetrov, V. R. Stamenkovic, S. Pejovnik, N. M. Marković, "Selective catalysts for the hydrogen oxidation and oxygen reduction reactions by patterning of platinum with calix[4]arene molecules," *Nature Materials*, 9, 998-1003, 2010.
- 13 X. Li, I. Sabir, "Review of bipolar plates in PEM fuel cells: Flow-field designs," *International Journal of Hydrogen Energy*, 30, 359-371, 2005.
- 14 J. Nie, Y. Chen, S. Cohen, B. D. Carter, R. F. Boehm, "Numerical and experimental study of three-dimensional fluid flow in the bipolar plate of a PEM electrolysis cell," *International Journal of Thermal Sciences*, 48, 1914-1922, 2009.
- 15 S. Grigoriev, P. Millet, S. A. Voloubuev, V. Fateev, "Optimization of porous current collectors for PEM water electrolyzers," *International Journal of Hydrogen Energy*, vol. 34, 11, 4968-4973, 2009.
- 16 P. Hu, L. Peng, W. Zhang, X. Lai, "Optimization design of slotted-interdigitated channel for stamped thin metal bipolar plate in proton exchange membrane fuel cell," *Journal of Power Sources*, 187, 407-414, 2009.

Arrived: 21. 03. 2011

Accepted: 26. 1. 2012

Design and modeling high performance electromechanical Σ - Δ modulator

Drago Strle*

University of Ljubljana, EE Department, Tržaška 25, Ljubljana, Slovenia

Abstract: In this article we present part of the design methodology, modeling and efficient simulation of high performance micro-electromechanical $\Sigma\Delta$ modulator. The method is based on converting continuous-time model of the MEMS sensor and eventual analog loop filter into discrete time equivalent using impulse invariant transformation. The methodology is valid for any "MEMS based cantilever" sensor operating in a closed loop, where mechanical transfer function does not provide adequate noise shaping to reach high accuracy and resolution. Using proposed methodology makes possible to efficiently design, predict the behavior and stability of the loop and perform efficient system level simulations.

Key words: electro mechanical $\Sigma\Delta$ modulator, modeling, CT to DT circuit equivalence

Načrtovanje in Modeliranje elektro-mehanskega Σ - Δ modulatorja z visoko ločljivostjo

Izveček: V članku obravnavamo metodologijo načrtovanja, modeliranje in učinkovito simulacijo visoko zmogljivega Mikro-Elektro-Mehanskega $\Sigma\Delta$ modulatorja. Metoda bazira na ekvivalenci odziva zveznega sistema, ki ga sestavlja zvezni model MEMS senzora ter eventualnega zveznega filtra v zanki ob času vzorčenja in diskretnega sistema ob enakih časih z uporabo impulzno invariantne transformacije. Metoda je veljavna za kakršenkoli MEMS sensor, ki bazira na odmiku oziroma oscilaciji MEMS senzorskega elementa in deluje v zaprti zanki, kjer prevajalna funkcija mehanskega dela ne zagotavlja zadostnega slabljenja kvantizacijskega šuma, da bi dosegli veliko ločljivost in točnost. Predstavljena metodologija omogoča učinkovito načrtovanje ter predvidevanje stabilnosti ter drugih lastnosti realiziranega mikro elektro-mehanskega sistema z uporabo hitrih simulacij na visokem hierarhičnem nivoju.

Ključne besede: elektromehanski $\Sigma\Delta$ modulator, modeliranje, ekvivalenca vezji v zveznem in diskretnem časovnem prostoru

* Corresponding Author's e-mail: drago.strle@fe.uni-lj.si

1. Introduction

High performance micro-machined sensors based on cantilevers are usually operating in closed loop to increase dynamic range, linearity, bandwidth and other parameters. To prevent pull-in and to improve noise performances a low order force-feedback 1 bit Σ - Δ modulator can be used. Further improvements are possible if high order modulator and/or multi bit force feedback are used instead. In that case, the mechanical element transfer function together with electronic transfer function form a loop filter and in this way the influence of quantization noise is reduced and higher resolution is possible. The price paid is increased instability of the control loop and difficult design procedure. This article presents possible architecture, modeling and simulation of high performance electromechanical $\Sigma\Delta$ modulator operating in closed loop.

In section 2, theoretical background is given using well-known model of mechanical mass-spring system. Section 3 gives design steps needed for the efficient design of mechanical $\Sigma\Delta$ modulator, while simulation results for designed modulators are presented in section 4. Section 5 concludes the article.

2. Theory

Block diagram of generic electromechanical $\Sigma\Delta$ modulator is presented on Figure 1 ([1], [2], and [3]).

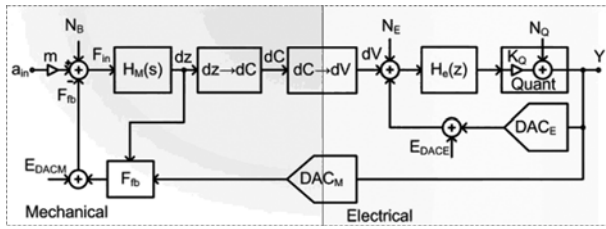


Figure 1: Generic electromechanical $\Sigma\Delta$ modulator

Mechanical part consists of a proof mass suspended by springs [6] (Figure 2) and can be described by (1).

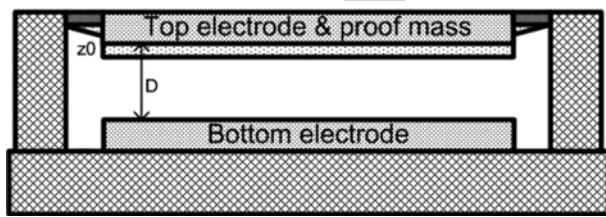


Figure 2: MEMS sensor

Mass of the sensor is m , $\omega_0 = \sqrt{k/m}$ is a resonance frequency of the mechanical part dependent on m and spring constant k , while δ is a damping factor (defined by friction of the media where the proof mass is moving).

$$H_M(s) = \frac{dz(s)}{F_{in}(s)} = \frac{1/m}{s^2 + s \cdot 2\delta\omega_0 + \omega_0^2} \quad (1)$$

Input signal is acceleration a_{in} that produce a force to the mass m . Feedback force F_{fb} tries to keep the sensor at equilibrium position, so the real input to the mechanical system is $F_{in} = m \cdot a - F_{fb}$. The sensor is prestressed by force F_0 so, that position of the mass at equilibrium is z_0 , which is away from the position D . The displacement dz describes the movement around z_0 . N_B models spectral density of the Brownian noise, which enters the loop unattenuated and is dependent on sensors characteristics and pressure around it; we will neglect it in this article because it is assumed that the sensor is operating in vacuum. The displacement dz can be measured through the change of capacitance represented by block $dz \rightarrow dC$ and described by (2) (ϵ_0 is permittivity of free space, A is the area of the electrode, D is the distance of the electrodes with zero force, z_0 is the displacement at force F_0 and dz represent small displacement around z_0). To sense the change of the capacitance, a HF sensing signal is applied to the sense capacitors of the sensor.

$$dC = \epsilon_0 A \left(\frac{1}{D + z_0 + dz} - \frac{1}{D + z_0} \right) \quad (2)$$

Charge amplifier converts charges to voltage at HF and amplify it. Synchronous demodulation converts signals back to the base-band, while LP filtering removes HF mixing components; in this way the influence of $1/f$ noise and offset voltage is reduced. All this elements are hidden in block $dC \rightarrow dV$ of Figure 1. Part of this block is positioned in electronic part, while another part is located in the mechanical part of the model. Signal dV enters the electronic part of $\Sigma\Delta$ modulator with loop filter transfer function described by $H_E(z)$. Electronic noise with spectral density N_E is added at the input and consist of all electronic noise sources calculated back to that input except the quantization noise. The quantizer is in fact a nonlinear element which can be modelled by simple "signum" function in nonlinear model or by gain factor K_Q and addition of quantization noise with density for linear model. The quantizer can be one bit for linearity and simplicity but can be also be multi bit if more demanding characteristics are needed. Errors caused by nonlinearity of the DAC inside the modulator are modelled by E_{DAC_E} ; they appear at the output unattenuated. The bit-stream signal described by $Y(s)$ for linear model is fed back and converted to voltage through block element DACM. The feedback force $dF_{fb} = F - F_0$ is dependent on V^2 and dz according to (3) where V_0 is selected in such a way that force F_0 is half of maximum force and causes prestressed position at $D + z_0$. Around that position the sensor moves by dz . For 1 bit quantizer the equation (3)

$$dF_{fb} = - \frac{\epsilon_0 A}{2} \left[\frac{V^2}{(D + z_0 + dz)^2} - \frac{V_0^2}{(D + z_0)^2} \right] \quad (3)$$

simplifies to (4), where BS stands for the bit-stream $BS = \{\pm 1\}$. We can see that the force in this case is not any longer in quadratic relation with the applied voltage.

$$dF_{fb} = - \frac{\epsilon_0 A}{2} \frac{V_0^2}{2} \left[\frac{(1 + BS)}{(D + z_0 + dz)^2} - \frac{1}{(D + z_0)^2} \right] \quad (4)$$

For average $a_{in} = 0$ the average of $(1 + BS) = 1$ and small nonlinearity still remains due to dependency of (4) on dz . For low resolution devices this nonlinearity is of no problem but for high resolution devices the nonlinearity reduces the SNDR as shown in section 4. It can be compensated adding appropriate nonlinear electronic feedback; the solution is in development.

To prepare the background for synthesis of the loop transfer function we need to linearise nonlinear components of the sensor. Assuming that dz is small compared to z_0 , only linear term of the Taylor expansion is preserved, thus, dF_{fb} and dC are simplified to (6) and (7) respectively. The linear term in (5) is much smaller than ω_0^2 , so the right summand could be neglected, which gives (6). Because linear model (6) does not contain any term in dz we can drop the line connecting that signal with block F_{fb} (Figure 1).

$$dF_{fb} \cong - \frac{\epsilon_0 A V_0^2}{2} \left[\frac{BS}{(D+z_0)^2} - \frac{2 \cdot dz \cdot (1+BS)}{(D+z_0)^2} \right] \quad (5)$$

$$dF_{fb} \cong - \frac{\epsilon_0 A V_0^2}{2} \left[\frac{BS}{(D+z_0)^2} \right] \quad (6)$$

$$dC \cong - \frac{dz \cdot \epsilon_0 \cdot A}{(D+z_0^2)} \quad (7)$$

Keeping the linear term of Taylor expansion for dC gives (7).

3. Design procedure

The design procedure for an electronic $\Sigma\Delta$ modulator starts with synthesis of noise transfer function from required SnR and oversampling ratio, followed by selection of appropriate electronic topology to assure all requirements [7]. Because of simplicity, speed of simulation and available design tools the synthesis is usually done in z domain even for the CT- $\Sigma\Delta$ modulators. $NTF(z)$ is synthesized followed by the synthesis of the loop filter $H(z)$ for DT modulator or $H(s)$ for CT implementation. In later case the response of DT prototype modulator and CT must be equal at $t = nT_s$ (equations (8), (9) and (10)), where $\hat{r}_{DAC}(t)$ is the impulse response of D/A converter; this is so called impulse invariant transformation [5].

$$x(nT_s) = \hat{x}_a(t) |_{t=nT_s}; \quad (8)$$

$$h_M(nT_s) = h_M(t) |_{t=nT_s}$$

$$h(nT_s) = Z^{-1} \{H(z)\} = L^{-1} \{ \hat{R}_{DAC}(s) \cdot \hat{H}(s) \} |_{t=nT_s} \quad (9)$$

$$h(nT_s) = [\hat{r}_{DAC}(t) * \hat{h}(t)] |_{t=nT_s} = \left[\int_{-\infty}^{+\infty} \hat{r}_{DAC}(\tau) \cdot \hat{h}(t-\tau) d\tau \right] |_{t=nT_s} \quad (10)$$

In the case of mechanical $\Sigma\Delta$ modulator the mechanical part of the transfer function is already present, thus part of the loop transfer function is already defined. Unfortunately, internal nodes are not available for optimization and stabilization and in addition, there is no freedom for changing parameters of that part because it is defined by required mechanical characteristics. The minimum order of the total loop transfer function is two if electronic loop filter does not exist. Unfortunately, the amount of noise shaping provided by only $H_M(s)$ is not big enough for high-resolution mechanical $\Sigma\Delta$ modulator; therefore, the electronic filtering is needed [4]. Because of sampling inside the loop, the system is

a mixture of CT and DT system. To be able to correctly design such a system the equivalence between continuous time (CT) and discrete time (DT) system must be preserved using so-called impulse invariant transformation. We can distinguish three cases regarding loop transfer function and sampling: $H_M(s)$ and sampling in front of a quantizer, $H_M(s)$ and $H_E(z)$ with sampling in front of $H_E(z)$ and $H_M(s)$ followed by $H_E(s)$ while sampling occurs in front of a quantizer. The simplest possibility is presented on Figure 3. In this case, the only filtering element is mechanical transfer function $H_M(s)$. To be able to analytically analyze and model such modulator we have to calculate the response of the mechanical element at the sampling instances. The mechanical transfer function in z domain is than $H_M(z)$, which we obtain by impulse invariant transformation of $H_M(s)$, taking into consideration also transfer function of the D/A. Upper part of Figure 4 shows both arrangements: CT on the left and DT on the right.

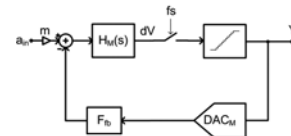


Figure 3: Simplest mechanical $\Sigma\Delta$ modulator

They will behave equally if impulse responses are the same at nT_s . The CT system has three problems. The delay between sampling instant and reaction of the DAC may compromise the stability of the loop; we can solve it by taking into considerations the shape of the DAC pulse. The second problem is that the rise and the fall times of the DAC pulses are usually not equal; they are signal dependent, which degrades the SnR and causes inter-symbol interference. We can minimize it by appropriate shaping of the DAC pulse (for example RZ instead of NRZ). The third problem is that mechanical DAC generates nonlinear feedback force (3), which can be solved by appropriate electronic linearization.

For the DT implementation, the DAC is of no problem because by correct design we can assure a complete charge transfer in one sampling period.

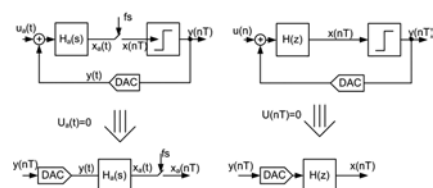


Figure 4: CT-DT equivalence

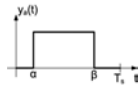


Figure 5: Shape of the DAC pulse

For CT systems, we have to implement and model the DAC correctly. Possible DAC pulse for one-bit quantizer is presented on Figure 5 and described by (11), where $0 \leq a < 1, 0 \leq \beta < 1, a < \beta$ and $u(t)$ is a unit step function.

$$\hat{r}_{DACM}(t) = u(t - aT_s) - u(t - \beta T_s) \quad (11)$$

The Laplace transformation of (11) gives (12):

$$L\{\hat{r}_{DACM}(t)\} = \frac{e^{-saT_s} - e^{-s\beta T_s}}{s} \quad (12)$$

The shape of the DAC pulse changes the loop transfer function. In this paper, we will treat only the case $a = 0, \beta = 1$, while general case is under development. Mechanical properties define poles, zeroes and coefficients that can be calculated by fractional expansion of (1) using (13) and (14) for $\delta \neq 1$. Equivalent DT transfer function $\hat{H}_M(z)$ can be expressed as a sum of first order poles (15).

$$\hat{p}_{1,2} = -\delta \cdot \omega_0 \pm \sqrt{\delta^2 - 1} \quad (13)$$

$$\hat{a}_1 = -\hat{a}_2 = \frac{1}{m \cdot 2 \cdot \omega_0 \cdot \sqrt{\delta^2 - 1}}$$

$$\hat{H}_M(s) = \sum_{k=1}^2 \frac{\hat{a}_k}{s - p_k} \quad (14)$$

$$H_M(z) = \sum_{k=1}^2 \frac{z a_k}{z - z_k} \quad (15)$$

Parameters a_k and poles z_k are calculated by explicit evaluation of (10) equating corresponding coefficients. The results are given in (16) to (19):

$$\hat{h}(nT_s) = \sum_{k=1}^2 \frac{\hat{a}_k}{\hat{p}_k} (e^{\hat{p}_k T_s (1-\beta)} - e^{\hat{p}_k T_s (1-a)}) \quad (16)$$

$$Z^{-1}\{H(z)\} = a_1 z_1^{nT_s} u(nT_s) + a_2 z_2^{nT_s} u(nT_s) \quad (17)$$

$$a_k = \frac{\hat{a}_k}{\hat{p}_k} (z_k^{(1-\beta)} - z_k^{(1-a)}); \quad k = 1, 2 \quad (18)$$

$$z_1 = e^{\hat{p}_1 T_s}; z_2 = e^{\hat{p}_2 T_s} \quad (19)$$

For $\delta = 1$ the calculation of poles and zeroes is different according to (20)

$$p_x \rightarrow 0; z_x \rightarrow 1; \quad (20)$$

$$a_x \rightarrow -a_x \frac{\beta - \alpha}{(1 - \beta)(1 - \alpha)}$$

Using transformations given in (18) and (19) the mechanical $\Sigma\Delta$ modulator transfer function can be translated to DT domain where simulations are faster compared to CT domain; in addition, we can easily test and predict closed loop stability characteristics and perform also other necessary simulations.

4. Simulation results

To prove the efficiency of the methodology, different MEMS electromechanical modulators have been designed using the sensor model defined in (1). Brownian noise has been neglected because it is assumed that the sensor is in a vacuum. Three different designs differ in the electronic loop filter order: zero one and two. The stability of the loop is of no concern for the first two designs, while for higher order electronic loop filter the poles and the zeroes must be optimized for stability. In our examples, the electronic loop filters are CT followed by one-bit quantizer, with sampling frequency 1MHz. Input acceleration is equal for all three cases. Simulation results using Matlab for three topologies are presented on Figure 6. The SnR in 1kHz bandwidth and HD are calculated for each design. As expected, increasing electronic loop-filter order increases the SnR, while HD remains the same. In addition, 2nd order electronic loop filter provides much bigger bandwidth compared to the first order structure because of more aggressive noise shaping, which is beneficial characteristics.

5. Conclusions

A design methodology and Matlab modeling of precision MEMS electromechanical $\Sigma\Delta$ modulators is presented in the article. We show methodology, mathematical modeling and Matlab simulation results for three different electronic loop filters. Methodology is adapted from the design procedure for the CT modulators and is applicable to general closed loop mechanical $\Sigma\Delta$ modulator. In the future, the design procedure will be generalized to the synthesis of arbitrary-order electronic loop filter implemented with CT or S-C circuits with mechanical part consisting of complex poles and higher order modes to be able to control and predict the stability of the closed loop system already during the design procedure. The linearization of the feedback force is currently under development.

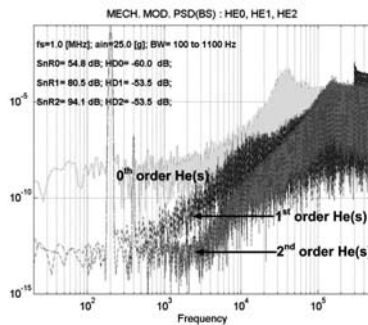


Figure 6: Spectrums of three MEMS $\Sigma\Delta$ modulators with different orders of electronic noise shaping filters.

References

- 1 T.Smith, O. Nys, M. Chevroulet, Y. DeCoulon, M. Degraue, "A 15b Electromech. S-D Converter for Acceleration Measurements," ISSCC 94.
- 2 H.Kulah, J. Chae, N. Yazdi, K. Najafi, "Noise Analysis and Characterization of a Sigma-Delta Capacitive Micro accelerometer," IEEE JSSC, vol. 41, No. 2, Feb. 2006.
- 3 C.P.Lewis, M. Kraft, T.G.Hesket, „Mathematical model for micromachining accelerometer," Trans. Inst. Of Meas. and Control, Vol 18, No.2, pp 92-98, 1996.
- 4 Y.Dong, M. Kraft, C. Gollasch, W.R. White, „A high performance accelerometer with a fifth-order sigma-delta modulator," Journal of Micromechanics and Micro engineering, vol. 15, pp. 1-8, March 2005.
- 5 J.A.Cherry, W.M.Snelgrove, "Excess Loop Delay in Continuous-Time Delta-Sigma Modulators," IEEE trans. on CAS-II, Analog and digital signal processing, vol. 46, No. 4. April, 1999.
- 6 M. Brandl M, V. Kempe "High performance accelerometer based on CMOS technologies with low cost add-ons," 14th International Conference on MEMS, Interlaken, January 2001.
- 7 S.R.Norsworthy, R.Schreier, G.C.Themes, " Delta-Sigma Data Converters, Theory, Design and Simulation," IEEE Press 1997.

Arrived: 22. 02. 2011

Accepted: 26. 1. 2012

A 4.1-bit, 20 GS/s Comparator for High Speed Flash ADC in 45 nm CMOS Technology

M.J. Taghizadeh, Marvast, H.Sanus, M. A. Mohd. Ali*

Universiti Kebangsaan Malaysia, Bangi, Malaysia

Abstract: A 4.1-bit, high speed comparator for high-speed flash analog-to-digital converter and K-band applications that can work at a sampling rate of 20GS/s is presented in this paper. This fully differential comparator consists of three stages using a new structure to improve its performance. The offset voltage of the designed comparator has been reduced by means of an active positive feedback. The CMOS positive feedback and a new structure as output circuit are used to improve sampling rate and performance of comparator. The analyses and simulation results were obtained by using CMOS parameters. The comparator can operate with a 1 V peak to peak input range consuming 0.561 mW. The predicted performance is verified by analyses and simulations using HSPICE tool.

Keywords: Analog –to- Digital converter, Comparator, Preamplifier.

4.1-bitni 20 GS/s komparator za hitrobliskovni ADC v 45 nm CMOS tehnologiji

Izveček: V članku je predstavljen 4.1-bitni hiter komparator za hitrobliskoven analogno-digitalen pretvornik in K-pasovne aplikacije, ki lahko delujejo pri vzorčni frekvenci 20 GS/s. Polno diferencialen komparator uporablja za izboljšanje učinkovitosti novo tristopenjsko strukturo. Ničelna napetost načrtovanega komparatorja je bila zmanjšana v smislu pozitivne povratne vezave. Pozitivna CMOS povratna vezava in nova struktura izhodnega vezja je bila uporabljena za izboljšanje vzorčenja in učinkovitosti komparatorja. Analize in rezultati simulacij so bile opravljene na osnovi CMOS parametrov. Komparator deluje pri napetosti 1 V (peak to peak) in porabi 0.564 mW. Predpostavljena učinkovitost je bila preverjena s simulacijskim orodjem HSPICE.

Ključne besede: anogno digitalni pretvornik, komparator, predojačevalac

* Corresponding Author's e-mail: taghiza@eng.ukm.my

1. Introduction

Flash analog-to-digital converters (ADC) with X-band and K-band frequency sampling rates are critical components for applications such as radar, signal capture, satellite, digital oscilloscopes and waveform recorders [1]. Today researchers and the industry have extended the requirement for higher frequency and higher sample rate. Flash can generally achieve the higher sampling rates, with the comparator limiting the maximum achievable sampling speed. In addition, this comparator can be used for UWB, X-band and K-band technology that offer a lot of capability for the design of communications devices requiring very high performance and low power consumption. The comparators published in years [2][3][4] still have relatively high power consumption and operate with sampling rate lower than the expected future requirement. In this paper a new CMOS positive feedback is proposed to increase

the speed of track and hold (T/H) of the comparator. A new structure is also proposed to achieve the overall high speed for the comparator. The comparator design incorporates various techniques to lower its power consumption and improve its overall performance. The comparator architecture is described in Sect. 2. The preamplifier design, T/H and output domino logic are presented in Sect. 3. Section 4 shows the simulation results, and finally Sect. 5 is the conclusion.

2. Architecture

Fig. 1 illustrates the comparator architecture that consists of preamplifier, track&hold (T/H) and output circuits. The comparator structure is fully differential and consists of three stages. The first stage is a low gain differential amplifier with resistive loads (RD), which is high range band with.

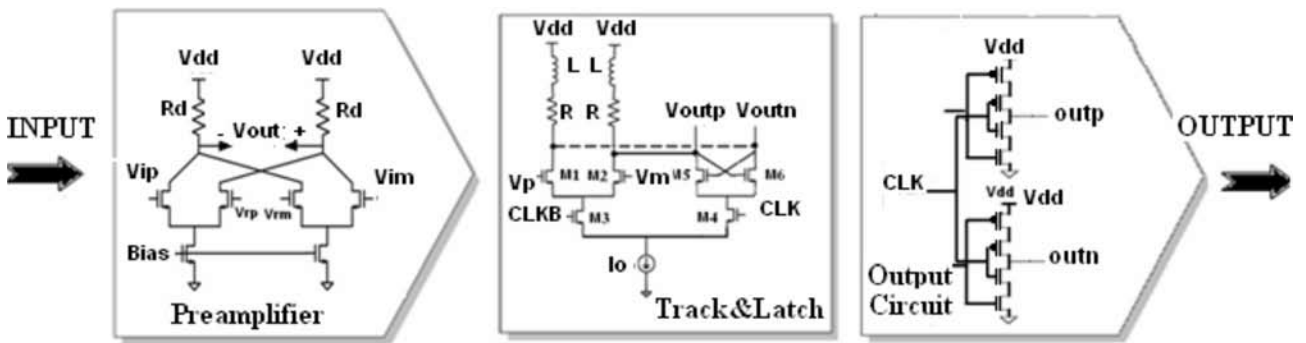


Figure 1: Schematic of comparator.

The comparator with resistive loads shows better linearity offset and gain response in comparison with comparators with active or diode loads. The first stage of comparator is used to reduce the input offset of comparator. The second stage is a CMOS track and hold with positive feedback and used of inductor and current source to reduce regenerative time. The domino output circuit that is new our suggestion circuit as shown in right block of Fig. 1 is used instead of SR Latch to support the comparator in high sampling rate.

er, making the design a multi-dimensional optimization problem. Illustrated in Fig. 2 such trade-off present many challenges in the design of high quality comparator for flash ADC, requiring intuition and experience to arrive at an acceptable compromise.

3. Comparator Design

3.1. Preamplifier

The low noise amplifier (LNA) is shown in Fig. 3. The main role of LNA is to reduce the input referred offset of the comparator. The preamplifier acts as an isolator between voltage reference and T/H to improve bandwidth and decrease input offset. The preamplifier has two inputs for differential analog signal and two inputs for voltage reference.

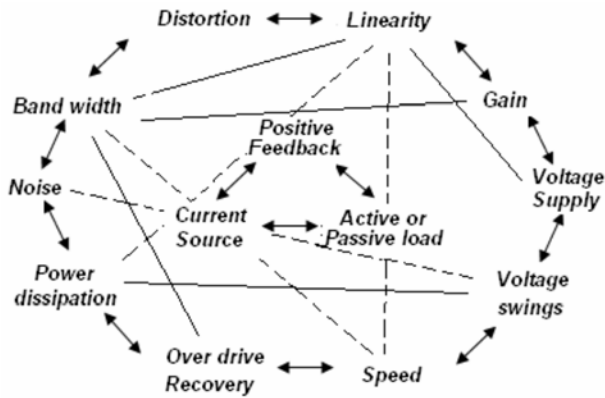


Figure 2: Relationship between comparator design parameters

In practical implementation, any random or systematic imbalance of the circuit creates an offset in the comparator. Offsets are classified as static or dynamic according to their origins. The fully differential comparator has many advantages to prevent supply and kickback noise and therefore, achieves a big dynamic range. The differential amplifier has better linearity.

It has to be clear, which aspect of comparators performance is important? In addition to power dissipation there are several items which may be important, such as supply voltage, gain, swing voltage, band width, distortion input offset, linearity and over drive recovery. In practice, most of these parameter trade with each other,

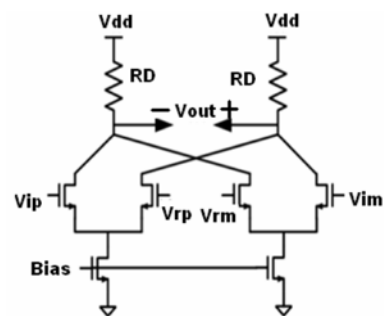


Figure 3: Preamplifier.

There is a relation between offset and W/L of the preamplifier that is equal to:

$$V_{\text{offset}} = \Delta Vt + \frac{1}{gm} \left(\frac{\Delta w_1}{w_1} + \frac{\Delta L_1}{L_1} + \frac{\Delta w_2}{w_2} + \frac{\Delta L_2}{L_2} + \dots + \frac{\Delta w_n}{w_n} + \frac{\Delta L_n}{L_n} \right) \quad (1)$$

where Vt is threshold voltage and gm is transconductance w and L are width and length respectively [5] [6].

Equation (1) indicates that with increase of transistor size (W) offset will be reduced, but this increase depends on the design. In addition, swing, bandwidth, output capacitance and linearity are important factors to choose the load of preamplifier. The linearity and frequency response of the preamplifier with passive load is better than preamplifier with active load. It is important to note that, with increasing LNA gain, the bandwidth is also decreased.

3.2. Comparator core (T/H) and Output circuit

The comparator core is shown in Fig. 4. The load is formed by the series combination of a resistor and an inductor. V_p and V_m are the differential analog inputs signal from the preamplifier. It has input differential pairs (M1 and M2) that turn on when the clock is low and track the input from the previous stage. When the clock is high, the comparator goes into hold mode. In this paper CMOS positive feedback is applied to improve speed of comparator and decrease the regenerative time in latching mode. The passive inductor peaking technique is also employed in the T/H circuit to enhance the bandwidth [7] [8] [9]. The comparator core is designed using new structure. This type of design is the most efficient in terms of speed and very low swing signal operation. Therefore, it's reduced output swing and hence low-power dissipation. In other words, the domino output circuit as shown in Fig. 1 is used instead of SR Latch to support the comparator in high sampling rate operation. The combination of T/H and output circuit creates a fast structure for the comparator. Domino logic as output circuit operates in two phases, the precharge phase and the evaluation phase. In the precharge phase, output is precharged from low to high, while in the evaluation phase, output will either be discharged from high to low or remain high.

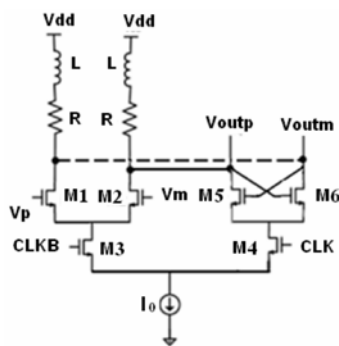


Figure 4: Comparator core (Track/Hold).

4. Simulation Results

The proposed comparator structure is designed using 45 nm CMOS technology. Simulation result was obtained by using HSPICE tool Table 1 shows the summary of comparator performance, in comparison with the designs in [2] and [3].

The new comparator dissipates only 0.561 mW at 20 GS/s. Fig. 6 shows the output wave of comparator with 1 GHz analog input signal and clock frequency of 20 Gs/s. The FFT of the signal at input frequency of 6.5 GHz and sampling rate of 20 Gsample/s is shown in Fig. 5.

5. Conclusion

In this paper, a 45 nm CMOS K-band comparator for high speed low power flash ADC is proposed. CMOS positive feedback and a new structure as output circuit are used to improve sampling rate and performance of comparator. We have used new core structure and domino logic circuit to speed up, reduce crosstalk and save power consumption of comparator. The measured ENOB is 4.1 bits at 20 GS/s with a 6.5 GHz sine input signal.

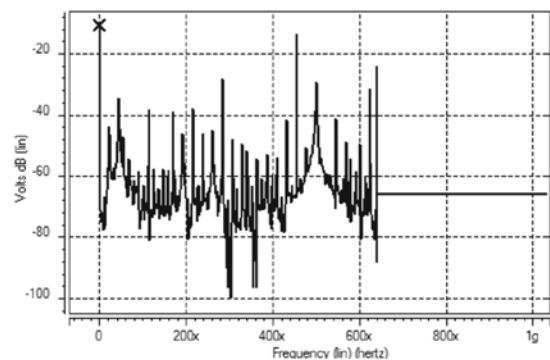


Figure 5: FFT at input frequency of 6.5 GHz and sampling rate of 20 Gsample/s.

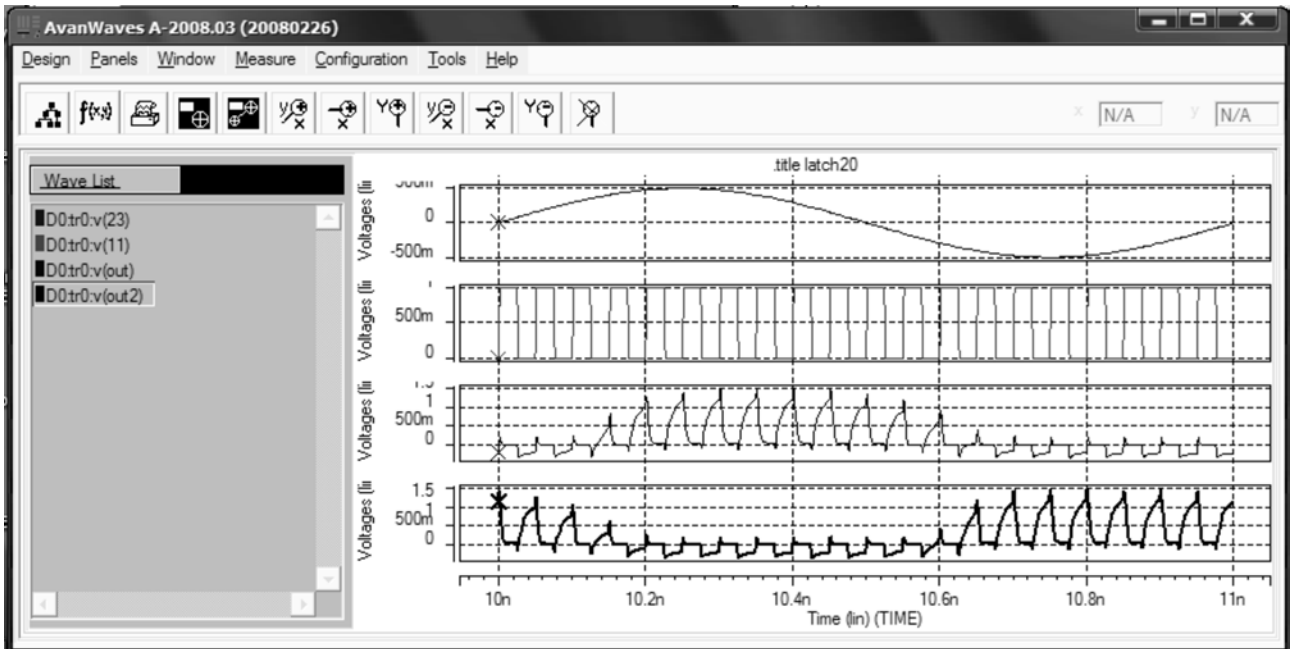


Figure 6: shows output wave of comparator at $F_{in}=1\text{GHz}$, $F_{clk}=20\text{Gs/s}$.

Table 1: Performance comparison

| Aurhor | Supply voltage | Sampling frequency (fs) | ENOB Effective number of bits (ENOB) | Process | Power dissipation | Years |
|-----------|----------------|-------------------------|--------------------------------------|-------------|-------------------|-------|
| [3] | 1 v | 4 (GS/s) | 4 | 90 nm CMOS | 3.6 mW | 2007 |
| [4] | 1.2 v | 0.5 (GS/s) | 3.5 | 130 nm CMOS | 148 μW | 2007 |
| [2] | 2.2 v | 11 (GS/s) | 3 | 120 nm CMOS | - | 2008 |
| This work | 1.8 v | 20 (GS/s) | 4.1 | 45 nm CMOS | 0.561 mW | 2010 |

References

- 1 Federal Communications Commission. (2002). First Report and Order Revision of Part 15 of the commission's rules regarding ultra-wideband systems. ET Docket No. 98-153.
- 2 Yuan Yao, Foster Dai, J. David Irwin and Richard C. Jaeger. (2008). A 3-Bit 2.2V 3.08pJ/Conversion-Step 11GS/s Flash ADC in 0.12um SiGe BiCMOS Technology. IEEE Bipolar /BiCMOS Circuit and Technology Meeting (BCTM), Monterey, California.
- 3 International A. Mohan, A. Zayegh, A. Stojcevski, R. Veljanovski. (2007). High Speed Ultra Wide Band Comparator in Deep Sub-Micron CMOS. IEEE International Symposium on Integrated Circuits. ISIC07, Singapore.
- 4 J. P. Oliveira, J. Goes, N. Paulino, J. Fernandes, (2007) low power low voltage CMOS comparator for 4-bit FLASH ADCS for UWB applications. 14th International Conference, MIXDES 07.
- 5 B. Razavi, Principles of Data Conversion System Design, IEEE Press, 1995.
- 6 A. Mohan, A. Zayegh, and A. Stojcevski.(2007) A High Speed Analog to Digital Converter for Ultra Wide Band Applications. IFIP International Federation for Information Processing, pp. 169-180.
- 7 S. Park and M. P. Flynn,.(2006) A regenerative comparator structure with integrated inductors. IEEE Trans. Circuits Syst. I, vol. 53, pp. 1704–1711.
- 8 B. Razavi, Principles of Data Conversion System Design. (1994). Hoboken, NJ: Wiley-IEEE Press, p. 183.
- 9 S. S. Mohan, M. D. M. Hershenson, S. P. Boyd and T. H. Lee. (2000). Bandwidth extension in CMOS with optimized on-chip Inductors. IEEE J. Solid-State Circuits, vol. 35, no. 3, pp. 346–355.

Arrived: 07. 04. 2011
Accepted: 26. 1. 2012

Instructions for authors | *Navodila avtorjem*

Informacije MIDEM - Journal of Microelectronics, Electronic Components and Materials is a scientific-professional-societal publication of Professional Society for Microelectronics, Electronic Components and Materials – MIDEM Society. In the Journal, scientific and professional contributions are published covering the fields of microelectronics, electronic components and materials, including but not limited to Electronics, Technologies & Materials, Sensors and Actuators, Power Engineering and Telecommunications.

Authors should suggest to the Editorial board the classification of their contribution such as: original scientific paper, review scientific paper, professional paper...

Scientific and professional papers are subject to peer review.

Each scientific contribution should include the following:

1. Title of the manuscript, authors' names, name of the institution/company.
2. Key Words (5-10 words) and Abstract (200-250 words), stating how the work advances state of the art in the field.
3. Introduction, main text, conclusion, acknowledgements, appendix and references following the IMRAD scheme (Introduction, Methods, Results and Discussion).
4. At the end add full authors' names, titles and complete company/institution address, including Tel./Fax/Email.
5. Manuscripts should be prepared in MS Word format (.doc or .docx) or any OpenDocument format (.odt or .fodt) in single column format and font size 12pt. Recommended length of manuscript (figures not included) is 12-15 pages.
6. Slovene authors writing in English language must submit title, key words and abstract also in Slovene language.
7. Authors writing in Slovene language must submit title, key words and extended abstract (500-700 words) also in English language.

Other types of contributions such as popular science papers, application papers, scientific news, news from companies, institutes and universities, reports on actions of MIDEM Society and its members as well as other relevant contributions, of appropriate length, are also welcome.

General informations

1. Authors should use SI units and provide alternative units in parentheses wherever necessary.
2. Figures should be included in the text and provided separately in TIFF, PCX, JPG or GEM format.
3. Contributions may be written and will be published in Slovene or English language.
4. Authors are fully responsible for the content of the paper.

Contributions are to be sent electronically to:

editor@midem-drustvo.si

Informacije MIDEM - Journal of Microelectronics, Electronic Components and Materials je znanstveno-strokovno-društvena publikacija Strokovnega društva za mikroelektroniko, elektronske sestavne dele in materiale - MIDEM. Revija objavlja prispevke s področja mikroelektronike, elektronskih sestavnih delov in materialov. Ob oddaji člankov morajo avtorji predlagati uredništvu razvrstitev dela v skladu s tipologijo za vodenje bibliografije v okviru sistema COBISS.

Znanstveni in strokovni prispevki bodo recenzirani.

Znanstveno-strokovni prispevki morajo biti pripravljani na naslednji način:

1. Naslov prispevka, imena in priimki avtorjev brez titula, imena institucij in podjetij.
2. Ključne besede in povzetek (največ 250 besed).
3. Naslov dela v angleščini.
4. Ključne besede v angleščini (Key words) in podaljšani povzetek (Extended Abstract) v angleščini, če je članek napisan v slovenščini.
5. Uvod, glavni del, zaključek, zahvale, dodatki in literatura v skladu z IMRAD shemo (Introduction, Methods, Results And Discussion).
6. Na koncu dodajte polna imena in priimki avtorjev s titulami, naslovi institucij in firm, v katerih so zaposleni ter tel./Fax/Email podatki.
7. Prispevki naj bodo napisani v MS Word (.doc ali .docx) ali OpenDocument (.odt ali .fodt) formatu v enem stolpcu z velikostjo črk 12pt. Priporočena dolžina članka je 12-15 strani brez slik.

Ostali prispevki, kot so poljudni članki, aplikacijski članki, novice iz stroke, vesti iz delovnih organizacij, inštitutov in fakultet, obvestila o akcijah društva MIDEM in njegovih članov ter drugi prispevki so dobrodošli.

Ostala splošna navodila

1. V prispevkih je potrebno uporabljati SI sistem enot oz. v oklepaju navesti alternativne enote.
2. Risbe in slike naj bodo vključene v tekst in priložene ločeno v formatu TIFF, PCX, GEM ali JPG.
3. Prispevek je lahko napisan in bo objavljen v slovenščini ali v angleščini.
4. Avtorji so v celoti odgovorni za vsebino objavljenega sestavka.

Prispevke pošljite po elektronski pošti na:

editor@midem-drustvo.si



Strokovno društvo za mikroelektroniko,
elektronske sestavne dele in materiale

MIDEM pri MIKROIKS | Stegne 7 | SI - 1000 Ljubljana | Slovenia
t. +386 (0)1 513 37 78, +386 (0)1 513 37 68 | f. +386 (0)1 513 37 71
e. info@midem-drustvo.si | www.midem-drustvo.si

Midem Society registration form

FIRST NAME: _____ LAST NAME: _____ TITLE: _____

ADDRESS: _____

CITY: _____ POSTAL CODE: _____

COUNTRY: _____

DATE OF BIRTH: _____

EDUCATION (please, circle whichever appropriate)

| | | | | |
|-----|-----|-----|-------------|---------|
| PhD | MSc | BSc | High School | Student |
|-----|-----|-----|-------------|---------|

PROFESSION (please, circle whichever appropriate)

| | | | | |
|-------------|---------|-----------|------------|-------------------|
| Electronics | Physics | Chemistry | Metallurgy | Material Sciences |
|-------------|---------|-----------|------------|-------------------|

COMPANY: _____

ADDRESS: _____

CITY: _____ POSTAL CODE: _____

COUNTRY: _____

TELEPHONE: _____ FAX: _____

E-MAIL: _____

YOUR PRIMARY JOB FUNCTION (please, circle whichever appropriate):

| | | | |
|-------------|-------------|------------|-------|
| Fabrication | Engineering | Facilities | QA/QC |
| Management | Purchasing | Consulting | Other |

Please, send mail to (please, circle): a) company address b) home address

I will regularly pay the annual MIDEM membership fee (25,00 EUR/year in 2012).

MIDEM members receive printed version of Journal »Informacije MIDEM - Journal of Microelectronics, Electronic Components and Materials« (ISSN 0352-9045) for free!!!

SIGNATURE: _____ DATE: _____



MIDEM at MIKROIKS

Stegne 11
SI-1521 Ljubljana
Slovenia

Boards of MIDEM Society | Organi društva MIDEM

MIDEM Executive Board | Izvršilni odbor MIDEM

President of the MIDEM Society | Predsednik društva MIDEM

Prof. Dr. Marko Topič, University of Ljubljana, Faculty of Electrical Engineering, Slovenia

Vice-presidents | Podpredsednika

Prof. Dr. Barbara Malič, Jožef Stefan Institute, Ljubljana, Slovenia

Dr. Iztok Šorli, MIKROIKS, d. o. o., Ljubljana, Slovenija

Secretary | Tajnik

Olga Zakrajšek, UL, Faculty of Electrical Engineering, Ljubljana, Slovenija

MIDEM Executive Board Members | Člani izvršilnega odbora MIDEM

Prof. Dr. Slavko Amon, UL, Faculty of Electrical Engineering, Ljubljana, Slovenia

Darko Belavič, In.Medica, d.o.o., Šentjernej, Slovenia

Prof. Dr. Bruno Cvikl, UM, Faculty of Civil Engineering, Maribor, Slovenia

Prof. Dr. Leszek J. Golonka, Technical University Wroclaw, Poland

Leopold Knez, Iskra TELA d.d., Ljubljana, Slovenia

Dr. Miloš Komac, UL, Faculty of Chemistry and Chemical Technology, Ljubljana, Slovenia

Prof. Dr. Marija Kosec, Jožef Stefan Institute, Ljubljana, Slovenia

Prof. Dr. Miran Mozetič, Jožef Stefan Institute, Ljubljana, Slovenia

Jožef Perne, Zavod TC SEMTO, Ljubljana, Slovenia

Prof. Dr. Giorgio Pignatelli, University of Perugia, Italia

Prof. Dr. Janez Trontelj, UL, Faculty of Electrical Engineering, Ljubljana, Slovenia

Supervisory Board | Nadzorni odbor

Prof. Dr. Franc Smole, UL, Faculty of Electrical Engineering, Ljubljana, Slovenia

Mag. Andrej Pirih, Iskra-Zaščite, d. o. o., Ljubljana, Slovenia

Dr. Slavko Bernik, Jožef Stefan Institute, Ljubljana, Slovenia

Court of honour | Častno razsodišče

Emer. Prof. Dr. Jože Furlan, UL, Faculty of Electrical Engineering, Slovenia

Prof. Dr. Radko Osredkar, UL, Faculty of Computer and Information Science, Slovenia

Franc Jan, Kranj, Slovenia

Informacije MIDE
Journal of Microelectronics, Electronic Components and Materials
ISSN 0352-9045

Publisher / Založnik:
MIDEM Society / Društvo MIDE
Society for Microelectronics, Electronic Components and Materials, Ljubljana, Slovenia
Strokovno društvo za mikroelektroniko, elektronske sestavne dele in materiale, Ljubljana, Slovenija

www.midem-drustvo.si